Multi-Flyby Mission to a Potentially Hazardous Asteroid: Improving the Earth Impact Probability Knowledge

Alessandro Gianolio
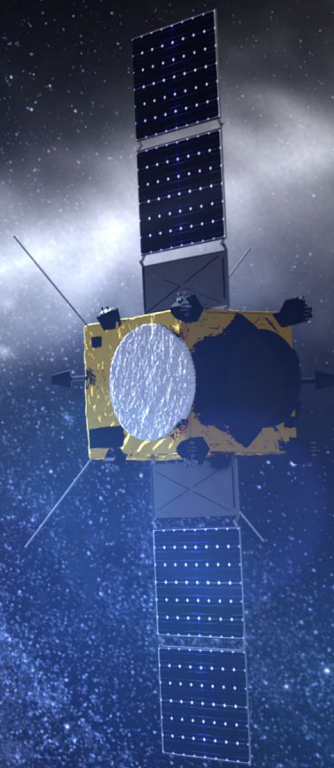
TUDelft Delft University of Technology

esa

Aerospace Engineering

Multi-Flyby Mission to a Potentially Hazardous Asteroid: Improving the Earth Impact Probability Knowledge

by

Alessandro Gianolio

to obtain the degree of

Master of Science
in Aerospace Engineering

at the Delft University of Technology

This thesis has been realised in collaboration with
the Mission Analysis Section of ESA/ESOC

Supervisors

Dr. Angelo Cervone	Dr. Dominic Dirkx	Dr. Waldemar Martens
Space Systems Engineering	Astrodynamics and Space Missions	Mission Analysis
TU Delft	TU Delft	ESA/ESOC

Preface

This master's thesis concludes my incredible journey as a university student. The bumpy ride until this very moment started in 2011 and finally reaches an amazing end after being able to score the thesis of my dreams. I often hear from fellow students that they tend to become annoyed or frustrated at their thesis sooner or later, while I, on the other hand, have enjoyed every single second of the last nine months working on this project. Especially the first six months of this thesis at ESA/ESOC have been a truly inspiring and incredible experience overall. In the three months that followed I continuously kept changing my working environment and found myself working on the thesis at very diverse places, ranging from the beach of Menorca to the university of Turin, which made this phase very enjoyable as well.

During these nine months I have had the luck to be surrounded by incredibly supportive and patient people helping me make this work what it turned out to be today. What makes this thesis project quite unique, is the fact that I did not have one or two supervisors, but I had a total of three supervisors contributing to this work. I am extremely thankful to Waldemar Martens, my ESA supervisor, as his involvement in this thesis has been absolutely incredible: his expertise on astrodynamics and orbit determination, his availability to spend from minutes to sometimes hours helping me out on a daily basis and friendliness have truly inspired me. This thesis would have never become what it is now without his help. Obviously, I am very grateful towards my university supervisors, Angelo Cervone and Dominic Dirkx, for making this thesis possible in the first place. Both have been very supportive since the very beginning, despite the early troubles to secure this thesis at ESA, and have been very flexible in letting me steer the thesis in a direction that interested me most.

I wish to thank all staff, contractors and students of ESA's mission analysis section for the wonderful experience. Especially Johannes Schoenmaekers for offering me this thesis position, Michael Khan for having me in his section, Lorenzo Bucci for his daily help with any questions that came to mind, Gábor Varga for always helping me fix the MATLAB interface when it broke, Amedeo Rocchi for helping me with the verification of the orbit determination tool and Ruaraidh Mackenzie for his help interpreting results from my simulations.

Words cannot express how grateful I am towards my family and close friends for their unconditional support and endless love, but I will try nonetheless. I am thankful to my parents, Alberto and Susi, for always encouraging me to pursue my dreams and then making it possible for those dreams to become reality, and to my sister, Alice, for always being there for me no matter what. I feel blessed for being surrounded by many close friends that accept me for the complicated individual that I am and care for me no matter where in the world I am.

This work is dedicated to the loving memory of Gyp, who always believed that I would accomplish great things in life. He would have been extremely proud of his grandson for this achievement.

"Chi più sa, più può."
— A.D. Calvi, Edinburgh (2018)

Abstract

The feasibility of improving the Earth collision uncertainty knowledge of a potentially Earth impacting asteroid by means of a multi-flyby mission has been researched in this thesis. The feasibility is assessed both from an astrodynamics point of view and from a systems engineering point of view. The astrodynamics part provides knowledge evolution results from a covariance analysis, which combines radiometric measurements of the spacecraft from Earth and optical measurements of the asteroid from the spacecraft. The systems engineering aspect on the other hand identifies all mission and subsystem requirements and provides possible subsystem design options.

From the 1906 potentially hazardous asteroids known at the time of writing, Apophis has been selected as the main research target due to its extremely close expected Earth encounter on April 13th, 2029: the expected miss distance is just 38440 km. Asteroids 2012 UE34 and 2001 WN5 have been selected as secondary targets. High-fidelity resonant trajectories have been generated using a multiple shooting method implemented in NASA's General Mission Analysis Tool. As a robust initial guess for these simulations, results from porkchop plots have been used, which combine the solution of Lambert's problem and resonance data. Only 1:1 resonance has been researched for this thesis. All trajectories target the asteroid B-plane at 600 km distance.

Data from JPL's HORIZONS has been used, alongside the generated high-fidelity trajectories, as input for a covariance analysis to produce the asteroid position knowledge evolution and the knowledge evolution of the asteroid in Earth's B-plane at the expected close-approach date. It has been found that, for Apophis, two flybys are sufficient to ensure mission success. After the second set of optical measurements, the orbital period of the asteroid is accurately known, which improves the asteroid position knowledge by roughly two orders of magnitude while improving the diameter of the covariance error ellipse at the expected close-approach date by roughly three orders of magnitude. The 1-σ error ellipse diameter shrinks from roughly 65000 km to roughly 15 km after two flybys. The analysis shows that for the used spacecraft trajectory the asteroid knowledge evolution is independent from the targeted flyby B-plane parameters. In the case multiple optical measurements are taken during a flyby, the knowledge evolution is found to be close-to independent from the distance to the asteroid when an optical measurement is taken. Asteroid WN5, which does not have a near-circular orbit around 1 AU such as Apophis and UE34, has a different knowledge evolution that does not improve the orbital knowledge after two flybys, meaning that the proposed mission would not be justified for this target.

The major conclusions that result from the systems engineering analysis are the following: a feasible launch strategy would be to use a light launcher, such as Vega, to launch the spacecraft to LEO, in combination with an upper stage, such as STAR 48, to escape Earth's gravity and put the spacecraft in the desired interplanetary trajectory. Feasible options for the propulsion system are an ion thruster, a cold gas system and a hydrazine system. All three require a low velocity increment, in the order of magnitude of a few m/s, which translates into a propellant mass of maximum 0.2 kg. The attitude control system needs to provide a slew rate of at least 0.835 degrees per second during the flyby phase for accurate asteroid pointing in order to make optical measurements. The estimated necessary average power equals 215.16 W and the peak power 485.76 W. The average power will be provided by GaAs solar panels with an estimated area of 0.6709 m^2, while Li-ion batteries with a storage capacity of 3301.11 Wh will be used to provide the necessary power during peak power scenarios. The high-level spacecraft design has an estimated dry mass of 149.77 kg, excluding the mass of the upper stage.

The combination of the astrodynamics aspects and the systems engineering aspects indicate that a flyby mission to a potentially Earth impacting asteroid is a promising option to improve the Earth collision uncertainty knowledge of that asteroid.

Contents

List of Tables

List of Figures

List of Abbreviations

The notations used for this thesis, in addition to the acronyms listed below, are the following:

- Vectors are denoted by a vector arrow, such as $\vec{V}$
- Scalars and variables are denoted by italics without a vector arrow, such as V
- Matrices are denoted by a bold letter, such as $\mathbf{\Phi}$
- Unit vectors are denoted by a hat symbol, such as $\hat{e}$
- Programs and tools are denoted by small caps, such as MATLAB
- Powers of 10 are often denoted with an e, such as 5e-1 instead of $5 \cdot 10^{-1}$

AIDA	Asteroid Impact and Deflection Assessment	JPL	Jet Propulsion Laboratory
AIM	Asteroid Impact Mission	JUICE	Jupiter Icy Moons Explorer
ART	Automated Regression Test	KBO	Kuiper Belt Object
AU	Astronomical Unit	LD	Lunar Distance
CA	Close Approach	LEOP	Launch and Early Orbit Phase
CCD	Charge Coupled Device	LGA	Low Gain Antenna
CDMU	Command and Data Management Unit	LOF	Local Orbital Frame
CFRP	Carbon Fibre Reinforced Polymer	LOS	Line of Sight
CIS	CMOS Image Sensor	LSK	Leapseconds Kernel
CNEOS	Center for NEO Studies	MASW	Mission Analysis Software
CoM	Centre of Mass	MEMS	Micro Electro-Mechanical System
CPS	Cumulative Palermo Scale	MGA	Medium Gain Antenna
CReMA	Consolidated Report on Mission Analysis	MICE	MATLAB SPICE
DART	Double Asteroid Redirection Test	MLI	Multi Layer Insulation
DHS	Data Handling System	MOID	Minimum Orbit Intersection Distance
DOT	Design Option Tree	MPC	Minor Planet Center
DST	Deep Space Transponder	NAC	Narrow Angle Camera
ECA	Earth Close Approach	NAIF	Navigation and Ancillary Information Facility
ECSS	European Cooperation for Space Standardisation	NASA	National Aeronautics and Space Administration
EIRP	Equivalent Isotropic Radiated Power	NEA	Near-Earth Asteroid
EOL	End of Life	NEC	Near-Earth Comet
EPC	Electric Power Conditioner	NEO	Near-Earth Object
ESA	European Space Agency	NEOCC	NEO Coordination Centre
ESOC	European Space Operations Centre	NEODyS	NEO Dynamical Site
ESTRACK	European Space Tracking	NGA	Non-Gravitational Acceleration
ET	Ephemeris Time	opnav	Optical Navigation
GNC	Guidance, Navigation and Control	PCDU	Power Conditioning and Distribution Unit
GS	Ground Station	PCK	Physical Constants Kernel
HGA	High Gain Antenna	PHA	Potentially Hazardous Asteroid
IAU	International Astronomical Union	PHC	Potentially Hazardous Comet
IEP	Implicitly Estimated Parameter	POS	Plane of Sky
IMCCE	Institute for Celestial Mechanics and Computation of Ephemerides	RCS	Reaction Control System
IMU	Inertial Measurement Unit	RFDN	Radio Frequency Distribution Network
IP	Image Processing	RTU	Remote Terminal Unit
JGM	Joint Gravity Model	SBDB	Small-Body Database

SEP	Solar Electric Propulsion
SPAD	Solar Pressure and Aerodynamic Drag
SPK	SPICE Ephemeris Kernel
SQP	Sequential Quadratic Programming
SRIA	Square Root Information Array
SRIF	Square Root Information Filter
SRP	Solar Radiation Pressure
STM	State Transition Matrix
TAI	International Atomic Time
TCM	Trajectory Correction Manoeuvre
TCS	Thermal Control System
TT&C	Telemetry, Tracking and Command
TWTA	Travelling Wave Tube Amplifier
UTC	Coordinated Universal Time

1

Introduction

Asteroids and comets, the building blocks of life, can potentially be of great hazard to Earth. The best example is the mass extinction of three quarters of the plant and animal species during the Cretaceous-Paleogene event 66 million years ago [1]. An asteroid estimated to be 10 km in diameter is believed to have impacted with Earth, catastrophically affecting the global environment and causing many species to become extinct [2] [3]. Differently than the dinosaurs during that period, we humans now have access to space and can potentially defend ourselves against a similar future threat.

Several space agencies, universities and research institutes have invested many resources in research regarding asteroids in the past few decades. For example, many asteroid impact mitigation missions and concepts have been developed in the last decade. Besides studying mitigation measures, many resources are spent in scouting for existing asteroids that have not yet been discovered. The ultimate goal is to map the trajectories of all existing asteroids in order to assess whether any of them can potentially collide with Earth[1]. In many cases Earth observations do not suffice in predicting whether a collision will take place or not.

One possible solution for this problem is to send a satellite to the potential impacting asteroid to perform measurements which will help improve the asteroid's orbit knowledge. The best way to do this would be to have a satellite rendezvous with the asteroid and map the asteroid completely, such as Rosetta did with comet 67P/Churyumov-Gerasimenko starting August 6th, 2014 [4]. Rosetta orbited the comet for approximately 1.5 years and performed an elaborated sequence of manoeuvres in order to perform all kinds of science measurements ranging from mapping the comet to understanding its composition. With these measurements, it has been possible to create an accurate 3D model of the exact shape of the comet [5]. This shape model in combination with the accurate state (position and velocity) data collected during this time made it possible to fully understand the effect of gravitational and non-gravitational effects on the comet, dramatically improving its ephemeris: by November 2014 the magnitude of the orbit prediction error, defined as the predicted orbit minus the reconstructed orbit, had already improved from an initial position error of about 1 km and a velocity error of about 1 cm/s to almost 0 for both [6] [7] [8].

Rosetta was a large and important mission consisting of an orbiter and a lander, which took much effort and many resources from both ESA and NASA [9]. It would be impossible to send such a mission to every asteroid that needs an ephemeris improvement, as it would require too many resources. A much more appealing alternative for these cases would be a small satellite with only one or few instruments that performs one or multiple flybys to the body for which an improvement in the orbit accuracy knowledge is required. The velocity increment (ΔV, or dV hereafter) needed to perform a flyby is much lower than that required for a rendezvous mission and even objects with a high inclination can be visited with little dV when they are close to crossing the Earth equatorial plane [10]. The orbit improvement would obviously be less than the case of a rendezvous mission, but a flyby mission could potentially be sufficient to determine whether an Earth impact by the target body will take place. The in-situ measurements during a flyby could certainly improve the knowledge of the target's orbit compared to an ephemeris solely based on measurements from Earth [11]. Additional flybys to the target could then improve the knowledge even further, which could efficiently be achieved with a resonant orbit.

This thesis will focus on this proposed resonant multi-flyby mission as it seems a viable solution for improving the uncertainty knowledge of an asteroid orbit with the use of limited resources. The main research question to be analysed is the following: *what is the feasibility of a multi-flyby mission to a potentially Earth impacting asteroid in order to improve the knowledge of the Earth collision uncertainty of that asteroid?* In order to answer this research question, the work has been split up in two independent parts: one focusing on the astrodynamics aspects of the mission and the other focusing on the systems

---

[1]https://cneos.jpl.nasa.gov/sentry/intro.html, accessed 22-05-2018

engineering aspects of the spacecraft. The main research question for the astrodynamics part is: *how can the knowledge of the uncertainty on the trajectory of an asteroid be improved by means of a multi-flyby mission to that asteroid?* The main research question for the systems engineering part is: *what are critical requirements and design considerations for an asteroid multi-flyby mission?*

This thesis is structured as follows: first, Potentially Hazardous Asteroids (PHAs), a subset of Near-Earth Objects (NEOs), will be introduced in the remainder of this chapter. The relevance of these small bodies, along with the available data and tools, will be discussed. Then, in Chapter 2, asteroid targets are chosen, the methodology to generate high-fidelity trajectories to these chosen targets are discussed and the trajectory results are presented. In Chapter 3, the mathematical model of the MATLAB tool created to perform a covariance analysis for a flyby mission to the selected targets will be explained in detail. The verification and validation, alongside the results, of this orbit determination model will be discussed as well. Using the trajectory and orbit determination results, it will be possible to perform an analysis of the entire spacecraft using systems engineering techniques. This is done in Chapter 4. Finally, conclusions and future work will be discussed in Chapter 5.

1.1. NEOs

Primitive bodies are the building blocks of life. These objects include main belt asteroids, Trojan asteroids, small satellites, comets, Centaurs and Kuiper Belt Objects (KBOs) [12]. Of particular interest for this study are NEOs, since these orbit closest to Earth, as the name suggests, and thus are the ones that are most likely to impact with Earth due to their close approaches. NEOs can be divided further into Near-Earth Asteroids (NEAs) and Near-Earth Comets (NECs). NECs are furthermore restricted to include only short-period comets, thus those that have an orbital period less than 200 years. The definition of NEOs are asteroids and comets with a perihelion distance less than 1.3 Astronomical Units (AU).

The vast majority of NEOs are NEAs, and since there are very little NECs, as will be clear later from Table 1.2, from here on when NEOs or asteroids in general are mentioned, NEAs will be implied. NEAs can be divided further into groups based on either physical or orbital properties. The most used group for dividing NEAs is the Tholen taxonomy, which is based on asteroid composition: C-type asteroids are dark carbonaceous objects, S-type asteroids are siliceous (stony) objects and X-type are asteroids which are mainly metallic [13]. However, for this study it is much more interesting to group the objects by orbital properties: perihelion distance (q), aphelion distance (Q) and semi-major axis (a). The four NEA groups; Atiras, Atens, Apollos and Amors and their properties can be found in Table 1.1, while their visualisations with respect to the Earth and the Sun can be seen in Figure 1.1.

Table 1.1: NEA Groups[2]

Group	Definition [AU]	Description
Atiras	$a < 1.0$ $Q < 0.983$	NEAs with orbits contained entirely within the orbit of the Earth
Atens	$a < 1.0$ $Q > 0.983$	Earth-crossing NEAs with semi-major axes smaller than Earth's
Apollos	$a > 1.0$ $q < 1.017$	Earth-crossing NEAs with semi-major axes larger than Earth's
Amors	$a > 1.0$ $1.017 < q < 1.3$	Earth-approaching NEAs with orbits exterior to Earth's but interior to Mars's

(a) Atiras   (b) Atens   (c) Apollos   (d) Amors
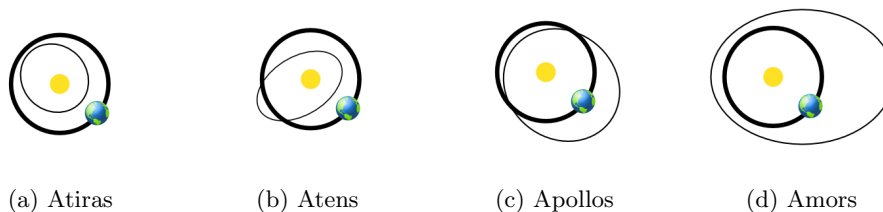
Figure 1.1: Visualisation of NEA Groups[2]

[2]https://cneos.jpl.nasa.gov/about/neo_groups.html, accessed 02-03-2018

Furthermore, another group of NEAs are the Potentially Hazardous Asteroids (PHAs). These are defined as NEAs with a Minimum Orbit Intersection Distance ($MOID$) with Earth of 0.05 AU or less and with an absolute magnitude of 22.0 or brighter[2]. An asteroid's absolute magnitude is the visual magnitude an observer would record if the asteroid would be 1 AU from him, 1 AU from the Sun and at a zero phase angle[3]. It is used to get a conservative estimate for the size of the NEA from Earth. The smaller the absolute magnitude, the higher the luminosity and thus the bigger the estimated size. This relation will be further discussed in Section 2.1.

1.2. NEO Data and Tools

It is essential to discover all existing NEOs to be able to assess whether any object will impact with Earth, this is therefore a high priority for space agencies. For example, NASA spends about M$4 annually to search for NEOs, with the goal to find those that may collide with Earth [14]. NEOs are being discovered on a daily basis and when a new NEO has been found it is stored in a database. A wide variety of NEO and asteroid databases are available, the four major ones are listed below [15].

- International Astronomical Union's (IAU) Minor Planet Center (MPC) Orbit Database[4]
- University of Pisa's NEO Dynamical Site (NEODyS)[5]
- Lowell Observatory's AstOrb[6]
- JPL's Small-Body Database (SBDB)[7]

Some of the data changes slightly per database. For example some newly discovered bodies are missing in some databases, which is often caused due to one the database not being updated yet. Some numbers for SBDB and NEODyS are given in Table 1.2.

Table 1.2: Number of Bodies Present in NEO Databases

Type	SBDB	NEODyS
Asteroids[8]	779911	656586
Comets	3520	3520
NEOs	18377	N/A
NEAs	18201	18184
NECs	176	~100
PHAs	1906	1896
Atiras	18	18
Atens	1344	1347
Apollos	9965	9974
Amors	6874	6820

There are several websites which integrate the databases and expand its capabilities in terms of search options and visualisation. Two examples are ESA's NEO Coordination Centre[9] (NEOCC), which uses the NEODyS database, and NASA's Center for NEO Studies[10] (CNEOS), which uses SBDB. Of particular interest on these pages are NEOCC's Risk Page[11] and CNEOS's Sentry[12]. These pages sort the NEOs based on risk potential. Of particular interest is JPL's HORIZONS[13] system. Detailed ephemeris data for asteroids can be generated using this system. HORIZONS reads the data from JPL's SBDB and propagates the orbit solutions to generate high-precision ephemerides as a function of time from this data.

---

[3]https://cneos.jpl.nasa.gov/glossary/h.html, accessed 02-03-2018
[4]http://www.minorplanetcenter.net/, accessed 02-03-2018
[5]http://newton.dm.unipi.it/neodys/, accessed 02-03-2018
[6]ftp://ftp.lowell.edu/pub/elgb/astorb.html, accessed 02-03-2018
[7]https://ssd.jpl.nasa.gov/sbdb.cgi, accessed 02-03-2018
[8]The big discrepancy here is due to NEODyS only having asteroids with good available orbital information
[9]http://neo.ssa.esa.int/, accessed 02-03-2018
[10]https://cneos.jpl.nasa.gov/, accessed 02-03-2018
[11]http://neo.ssa.esa.int/risk-page, accessed 02-03-2018
[12]https://cneos.jpl.nasa.gov/sentry/, accessed 02-03-2018
[13]https://ssd.jpl.nasa.gov/?horizons, accessed 05-03-2018

1.3. NEO Mitigation Strategies

While the actual asteroid mitigation is out of the scope of this study, as this study merely focuses on a possible flyby mission to the asteroid prior to sending a possible mitigation mission, it is worthwhile briefly researching current mitigation strategies to understand the relevance of such a flyby mission.

A "slow-push" or "slow-pull" strategy is a method where the orbit of the target object is slowly changed in order to avoid Earth collision. This can be done in a number of ways, but the most effective way to change the orbit with the lowest amount of energy is to change the velocity of the object in either the same way it is moving or in the opposite way [14]. A change of velocity in any other direction, such as sideways, would be much less efficient and require much more energy. This strategy is however only applicable for small NEOs with a diameter of no more than 100 meters.

A similar strategy is a gravity tractor concept. The idea of this method is to have a satellite close to the NEO in such a way that the gravitational attraction between them changes the orbit of the NEO[14]. This method is particularly interesting for NEOs of which the composition is not well known, as this is not needed [16]. However, just as the previous method, it is only applicable for small NEOs, as otherwise the gravitational attraction will be small or even negligible for changing the NEO orbit.

Another option is to have a kinetic impactor mission, which requires a satellite to impact with the NEO at a velocity of 10 km/s or higher in order to significantly deviate its trajectory. Several studies on kinetic impactors have been performed such as the Don Quijote concept [17], the joined ESA/NASA Asteroid Impact and Deflection Assessment (AIDA) which consists of two spacecraft: ESA's Asteroid Impact Mission (AIM) satellite would orbit the asteroid while NASA's Double Asteroid Redirection Test (DART) would impact with the asteroid. Even though AIM has been cancelled, NASA continued its studies for DART. Another example is NASA's Deep Impact mission, which proved the feasibility of a kinetic impactor mission: on July 4th, 2005, it successfully collided with Comet 9P/Tempel [18]. Within Airbus Defence & Space's NEOShield-2 project the NEOTωIST concept is being developed, which stands for "Near Earth Object Transfer of angular momentum Spin Test". It is a low-cost design concept which will demonstrate the kinetic impactor concept feasibility[15].

A final option would be to have an explosive detonate close to the NEO or on the NEO, often referred to as a blast deflection mitigation strategy[16]. This explosive can be either nuclear or non-nuclear [14] [16]. The blast could cause the NEO to completely or partially disintegrate and its orbit would be completely changed. When using this strategy, it has to be made sure that the fragments of the NEO after the explosion will also not impact with Earth, or at least be small enough to not cause harm.

---

[14]http://www.neoshield.eu/mitigation-measures-kinetic-impactor-gravity/gravity-tractor-spacecraft-asteroid/, accessed 02-03-2018

[15]http://www.neoshield.eu/science-technology-asteroid-impact/neo-angular-momentum-spin/, accessed 02-03-2018

[16]http://www.neoshield.eu/mitigation-measures-kinetic-impactor-gravity/blast-deflection-neo-path/, accessed 02-03-2018

2

Spacecraft Trajectory Design

This chapter will give a detailed discussion on the design methodology and results of the spacecraft trajectory. First of all, the chosen asteroid targets will be discussed in Section 2.1, followed by a brief discussion on an essential toolkit used throughout this whole thesis in Section 2.2. The trajectory design methodology will then be explained in two steps: first the initial guess generation using porkchop plots in Section 2.3, followed by the the high-fidelity ephemerides generation in Section 2.4, which also contains a brief introduction to the tool GMAT. Finally, the trajectory results will be presented in Section 2.5.

2.1. Target Selection

Before generating the trajectories, a decision about the possible targets has to be made. Naturally, only asteroids that will have a close encounter in the (near) future with Earth are relevant for this study. As mentioned in Section 1.1, PHAs have an Earth $MOID$ of 0.05 AU or less, which makes this group of asteroids the most interesting for this research. The actual close approach distance and its uncertainty are leading parameters for selecting feasible targets. The other factors that are important for selecting a target are estimated diameter, relative velocity, close approach date and absolute magnitude. The estimated diameter is important, since this will determine the consequences of an Earth impact. This parameter can be approximated using the following equation [19] [20]:

$$D = \frac{1329 \cdot 10^{-0.2H}}{\sqrt{A_g}} \tag{2.1}$$

where D is the estimated diameter in km, A_g is the geometric albedo, which is unitless, and H the absolute magnitude, which is also dimensionless but nonetheless often colloquially given a unit called mag. The approximation is based on the assumption that for small changes in absolute magnitude the quantity $(1 - A)D^2$ can be considered invariant, where A and D are the object's albedo and diameter, respectively. Most asteroids have a geometric albedo in the range of 0.05 to 0.25[1]. Estimates for both the absolute magnitude and the geometric albedo are given for most asteroids in JPL's HORIZONS. The relative velocity is furthermore also important to determine the Earth impact risk, as a higher velocity will result in a higher impact energy. The close approach date is relevant for determining how far in the future the impact is predicted. Obviously, close approaches which will happen in the near future are the most interesting to study. The absolute magnitude is important for two reason: the first is the relation with the estimated diameter, the second has to do with the optical navigation towards the target. A more visible asteroid is preferred, since the manoeuvre(s) needed to target the spacecraft accurately towards the asteroid using optical navigation will be possible much sooner if an asteroid has a higher visibility. A list of potential targets has been generated for this research, using CNEOS[2]. Only asteroids with an Earth Close Approach (ECA) up to and including the year 2050 have been taken into account, where the Close Approach (CA) distance is 1 Lunar Distance (LD) or lower. One Lunar Distance corresponds to 384400 km[3]. The targets including their respective important parameters discussed above are summarised in Table 2.1, sorted by the ECA epoch.

From this list it can be quickly concluded that the only targets worth researching for this thesis are 2001 WN5, 2004 MN4, 2012 UE34 and 2015 XJ351. The other targets have magnitudes above 24 mag, which means the asteroid will be very small and will thus not be as much of a threat in case of impact. Asteroids 2012 UE34 and 2015 XJ351 furthermore have an absolute magnitude between 22

---

[1]https://minorplanetcenter.net/iau/Sizes.html, accessed 20-08-2018
[2]https://cneos.jpl.nasa.gov/ca/, accessed 20-08-2018
[3]https://cneos.jpl.nasa.gov/glossary/LD.html, accessed 20-08-2018

Table 2.1: Potential Asteroid Targets

Asteroid	ECA Epoch	ECA Distance [km]	H [mag]	Diameter [m or km]	V_{rel} [km/s]
2001 WN5	2028-Jun-26 05:23	249860	18.2	610 m - 1.4 km	10.24
2004 MN4	2029-Apr-13 21:46	38440	19.7	310 m - 680 m	7.43
2001 AV43	2029-Nov-11 15:25	311364	24.6	32 m - 71 m	4.00
2014 HB177	2034-May-06 09:06	88412	28.1	6.4 m - 14 m	6.80
2017 FU102	2036-Apr-03 05:01	315208	28.7	4.8 m - 11 m	7.37
2012 UE34	2041-Apr-08 02:50	107632	23.3	58 m - 130 m	6.12
2018 GE2	2042-Oct-30 03:50	130696	27	11 m - 24 m	6.61
2012 HG2	2047-Feb-13 00:54	103788	27	11 m - 24 m	4.36
2015 XJ351	2047-Jun-06 09:07	303676	22.4	88 m - 200 m	15.84
2016 RD34	2047-Sep-05 11:11	103788	27.6	8.0 m - 18 m	3.01
2007 UD6	2048-Oct-18 01:47	57660	28.3	5.8 m - 13 m	7.03
2006 GU2	2050-Oct-09 08:32	176824	27.8	7.3 m - 16 m	7.62

and 24 mag, which means they are not considered PHAs, and their ECA will happen in more than 20 years. The only two targets that remain and thus have been selected as the chosen targets are asteroids 2001 WN5, from now on referred to as WN5, and 2004 MN4, also known as 99942 Apophis or simply Apophis. Coincidentally, these are the two asteroids with the closest ECA epochs. Since 2012 UE34's orbit is similar to Apophis's, this asteroid is selected as well despite its small size to compare results. A summary of all the important parameters, including the orbital elements, for these three asteroids is given in Table 2.2.

Table 2.2: Relevant Parameters of Apophis, WN5 and UE34

Parameter	Apophis		WN5		UE34	
Reference Epoch	24 Sep 2008		27 Apr 2019		27 Apr 2019	
Orbital Elements						
	Value	Uncertainty [1σ]	Value	Uncertainty [1σ]	Value	Uncertainty [1σ]
a [AU]	0.9224	4.1547e-10	1.7117	8.1758e-9	1.1053	1.3797e-6
e [-]	0.1911	5.3461e-9	0.4670	1.9944e-8	0.0992	7.8207e-7
i [deg]	3.3313	3.5025e-7	1.9198	3.3556e-6	9.6585	8.3467e-5
Ω [deg]	204.4460	2.1065e-5	277.5059	1.6588e-4	198.4812	5.3784e-5
ω [deg]	126.4018	2.0643e-5	44.5582	1.6573e-4	18.3849	5.1363e-4
M [deg]	180.4293	5.4642e-6	134.2477	9.7028e-6	51.8414	2.5245e-3
Other Orbital Parameters						
	Value	Uncertainty [1σ]	Value	Uncertainty [1σ]	Value	Uncertainty [1σ]
T [days]	323.5969	2.1863e-7	818.0372	5.8606e-6	424.4511	7.9471e-4
n [deg/days]	1.1124	7.5161e-10	0.4400	3.1528e-9	0.8481	1.5880e-6
Physical Parameters						
H [mag]	19.7		18.2		23.3	
D [km]	0.325		0.932		N/A	
A_g [-]	0.23		0.097		N/A	
Misc						
Earth $MOID$ [AU]	3.1568e-4		1.6325e-3		1.0015e-3	
OCC [-]	0		0		3	
Type [-]	Aten		Apollo		Apollo	

All the data of table 2.2 comes from the HORIZONS pages of the two asteroids, where T is the orbital period in days, n is the mean motion in degrees per days, D is the diameter in km, A_g is the geometric albedo. The OCC is the Orbit Condition Code which is a number ranging from zero to nine that defines the uncertainty of the orbit. A zero being well defined, and nine being highly uncertain. The OCC is also called the uncertainty parameter U by MPC, and is calculated using the following equation [21]:

$$U = min\left(9, max\left(0, \left[9 \cdot \frac{\ln r}{\ln 648000}\right] + 1\right)\right) \qquad (2.2)$$

Here, 648000 is the number of arc seconds in a half circle, and r is the in-orbit longitude runoff in seconds of arc per decade, which is calculated as follows:

$$r = \left(dT \cdot e + 10 \cdot \frac{dP}{P}\right) \cdot 3600 \cdot 3 \cdot \frac{k_0}{P} \qquad (2.3)$$

Here dT is the uncertainty in the perihelion time in days, e is the eccentricity, P is the orbital period in years, dP is the uncertainty in the orbital period in days and k_0 is the Gaussian constant in degrees, which is $180/\pi \cdot 0.01720209895$ rad ≈ 0.9856 deg.

The majority of this research will be based on Apophis, since it is a much more feasible target for this purpose than WN5: Apophis's orbital period of about 323 days will mean a much shorter mission duration compared to WN5's period of about 818 days. Furthermore, Apophis has an orbit with parameters much like Earth's orbit: it is near circular with a low eccentricity and a semi-major axis of almost 1 AU. On the other hand, WN5 has a highly elliptical orbit. Since the goal is to be in a resonant orbit, at least two or three flybys will be performed, meaning a total mission time of roughly seven years will be needed for WN5 in case of a 1:1 resonant orbit, compared to the roughly three years mission duration for Apophis. A short mission duration is preferred, especially considering the ECA for WN5 is already in 2028. The short mission duration will also directly relate to a much shorter computation time of the covariance analysis, which has also been a driving factor for this choice, since the calculation matrices will be much smaller as will become clear in Chapter 3. Even though most work will be done for Apophis, the trajectory and covariance analysis results for asteroids UE34 and WN5 have been included in this thesis as well: UE34 to compare with Apophis's results while WN5 as a bonus study case.

2.2. SPICE

Before discussing the actual trajectory design for the chosen targets, it is worth briefly discussing a tool that has been essential for this research: SPICE. SPICE is an information system built by NASA's Navigation and Ancillary Information Facility (NAIF), acting under the directions of NASA's Planetary Science Division, to assist scientists in planning and interpreting scientific observations from space-borne instruments, and to assist NASA engineers involved in modelling, planning and executing activities needed to conduct planetary exploration missions.

The SPICE data sets are called kernels or kernel files. The SPICE toolkit makes it possible to read, interpret and manipulate several kernel files. On MATLAB, these files can be used with the MATLAB SPICE (MICE)[4] toolkit. On JPL's public FTP server[5] many useful files such as pre-generated ephemerides can be downloaded, which can be used in combination with the SPICE toolkit for orbital calculations. Similarly, on NASA's public NAIF database[6] similar files can be found for a wide variety of solar system bodies and satellites.

Of primary interest are the planet, satellite, comet and asteroid ephemerides: the SPICE Ephemeris Kernels (SPK). Physical Constants Kernels (PCKs) contain a variety of body constants, such as radii and gravitational constants. Finally, Leapseconds Kernels (LSKs) are frequently needed when using several internal SPICE routines, such as the conversion of Coordinated Universal Time (UTC) to Ephemeris Time (ET). The generic JPL kernels used throughout this whole thesis, unless stated differently were applicable, are summarised in Table 2.3.

Table 2.3: Used Generic Kernels

Type	Name	Description
SPK	DE_432	Planetary and lunar ephemerides
PCK	GM_431	Mass data
	PCK00010	Size, shape and orientation data
LSK	NAIF0012	All leapseconds up to including 31/12/2016

---

[4]https://naif.jpl.nasa.gov/naif/toolkit.html, accessed 05-03-2018
[5]ftp://ssd.jpl.nasa.gov/pub/, accessed 05-03-2018
[6]https://naif.jpl.nasa.gov/pub/naif/, accessed 05-03-2018

2.3. Trajectory Initial Guess Generation

This section will discuss how initial guesses are generated for the high-fidelity ephemerides that will be generated later. First, the Lambert theorem will be briefly analysed to understand its basics and how it can be applied to generate porkchop plots. Then RESOTRAJ will be discussed, which is a tool written for this thesis to combine the data generated using the Lambert theorem with resonance data to find solutions for resonant orbits.

2.3.1. Lambert's Problem

Porkchop plots are very common to generate a first guess for a flyby or rendezvous interplanetary trajectory as they contain a lot of information about possible combinations of energy, launch date and time of flight in a single figure. Generating porkchop plots relies on solving the Lambert problem for a wide range of possible combinations. Since the Lambert problem is a very well known problem in the mission analysis field and the complex derivation is freely available in a wide range of papers [22] [23], it will not be discussed any further in this thesis. A brief discussion regarding how to generate results using the Lambert's problem will however follow.

Tools that solve the Lambert's problem are often referred to as Lambert solvers. Lambert solvers require the following inputs: the initial (departure) position vector, the final (arrival) position vector, the time of flight, the transfer angle (between initial and final position), the number of complete revolutions, the Lambert parameter and the gravitational constant of the central body. The number of complete revolutions means the amount of orbits around the central body before arriving at the final position, where a value of zero gives the fastest direct transfer. For a nonzero value of the number of complete revolutions, there are two possible solutions for every input which depend on the Lambert parameter: one with a smaller transfer time and one with a larger transfer time, see Figure 2.1.
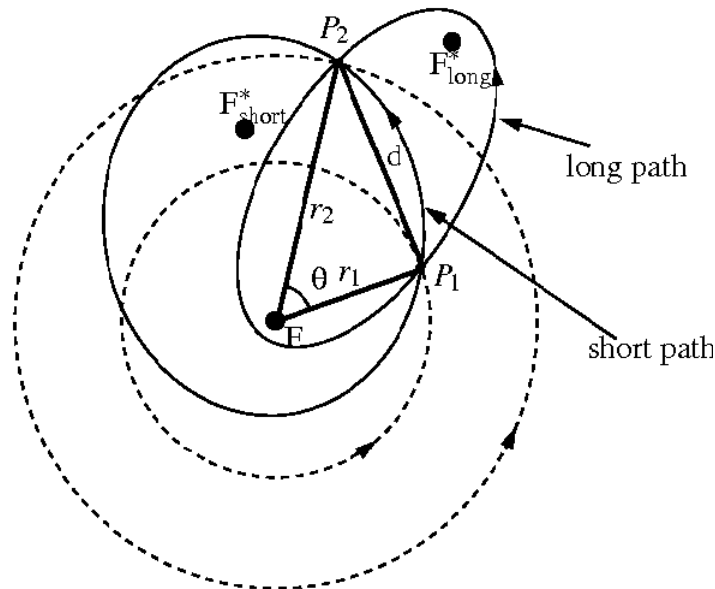
Figure 2.1: Short and Long Solution of the Lambert Problem [24]

For a full set of inputs, the result of a Lambert solver will be the initial and final velocity a spacecraft needs to achieve for that particular trajectory. In order to exploit a Lambert solver, it is looped over all possible inputs within a certain range, in order to see which generate feasible results in terms of dV. The initial position being the position of the departing body (in most cases Earth) at a certain initial epoch, and the final position being the position of the body to be visited at the epoch that sums the initial epoch and the time of flight. Using both the inputs and the outputs of every solution, a wide variety of data can be calculated for that specific solution, the excess velocity at departure and arrival being the most important, since these relate directly to the needed dV. These can be calculated in an inertial frame using:

$$\vec{V}_{\infty,d} = \vec{V}_{d,sc} - \vec{V}_{d,bo} \tag{2.4}$$

$$\vec{V}_{\infty,a} = \vec{V}_{a,sc} - \vec{V}_{a,bo} \tag{2.5}$$

Where the subscripts d and a stand for departure and arrival, respectively, while sc and bo stand for spacecraft and (departure or arrival) body, respectively. For interplanetary space missions, such as the one researched in this thesis, usually a heliocentric inertial frame is used for these equations. The spacecraft velocities are in fact the output of the Lambert solver, while the body velocities are assumed to be known since the state of the body is the input of the Lambert solver. These can be retrieved from SPICE kernels, discussed in Section 2.2. Aside from the excess velocity, the energy required, known as C_3, is also useful as this is a measure often used for launches to determine spacecraft dV needs, as the launcher performance is often expressed in C_3. It is calculated with:

$$C_{3,d} = \left(|\vec{V}_{d,sc}| - |\vec{V}_{d,bo}| \right)^2 = |\vec{V}_{\infty,d}|^2 \tag{2.6}$$

A porkchop plot is a contour plot containing the Lambert problem solutions, and different combinations are possible for what is plotted. A common possibility is to plot the contour levels of the C_3 for the combinations of departure date and time of flight.

2.3.2. Porkchop Plots and Resonant Orbits

A tool has been set up in MATLAB to create porkchop plots using the theory described in the previous section, named RESOTRAJ. Porkchop plots generated using an initial version, which uses the theory described in the previous section exclusively, is compared to porkchop plots available on JPL HORIZONS for verification purposes before expanding the tool. Important to note is that in this plot the solutions for 0, 1, 2 and 3 number of complete revolutions are combined into one figure and only combinations that give a C_3 value of 100 km^2/s^2 or less are kept, to be consistent with the porkchop plots available on JPL. See Figure 2.2. Since Figures 2.2a and 2.2b are close to being identical, this part of RESOTRAJ can be considered verified. The blue dots in Figure 2.2b depict solutions that have interactive features on the JPL website, and can be ignored in this work.

Important to note is that the trajectory analysed for this research is a flyby trajectory. This means that the $\vec{V}_{\infty,a}$ is not relevant for computing the total dV needs of the spacecraft, since no rendezvous manoeuvres will be necessary. The total dV will thus only depend on the launch, and the Trajectory Correction Manoeuvres (TCMs), which will be discussed in Section 2.4. Also important to note is that for this research a resonant orbit is required, which means only a small portion of the porkchop plot that satisfies the resonant orbit constraint will be relevant for this case. In order find the solutions of the porkchop plot that satisfy the resonant orbit constraint, additional computations are needed.

First of all, the semi-major axis is calculated from the initial state vector (or final state vector, it will give the same solution), using the following equation:

$$a = \frac{||\vec{r}||}{2 - \frac{||\vec{r}|| \cdot ||\vec{V}||^2}{\mu}} \tag{2.7}$$

Here $\vec{r}$ and $\vec{V}$ are the position and velocity vectors, respectively, and μ is the gravitational parameter of the central body, in this case the Sun. The semi-major axis is then used to calculate the orbital period T, using:

$$T = 2\pi \sqrt{\frac{a^3}{\mu}} \tag{2.8}$$

The semi-major axis and orbital period are calculated for both the spacecraft and the target asteroid. In order to satisfy the resonant orbit constraint, the following equation must be satisfied:

$$T_{sc} \cdot n_{sc} = T_{bo} \cdot n_{bo} \tag{2.9}$$

(a) RESOTRAJ Solution

(b) HORIZONS Solution
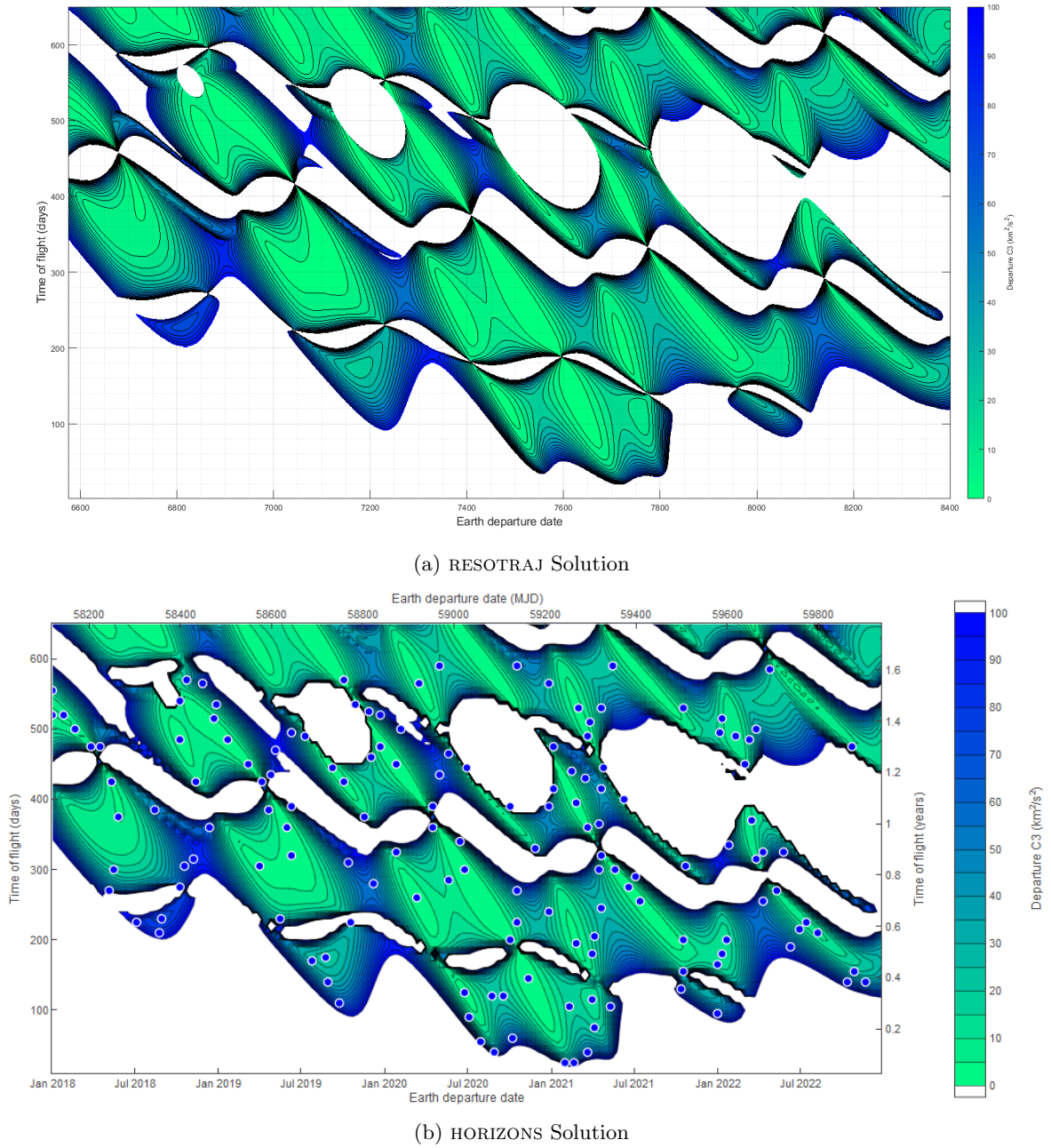
Figure 2.2: Porkchop Plots for Asteroid Apophis

In this equation n_{sc} and n_{bo} are the number of complete revolutions around the Sun of the spacecraft and the target body, respectively, before returning at the exact point in space. To keep things simple only 1:1 resonant orbits have been assessed for this thesis, meaning both n_{sc} and n_{bo} are set to one. The orbital periods of the spacecraft and the target body thus have to be the same to achieve resonance.

Another important thing to note is that to generate the solutions, both for the porkchop data and the resonance data, two Lambert problems have in fact been solved consecutively instead of just one. The reason for this, is that the trajectory consists of a flyby with a certain distance to the target asteroid. With the Lambert problem, all targets are assumed to be point masses and the centre of a body is targeted. One of the solutions in order to target the asteroid flyby at a certain distance from the target body centre is to solve a second Lambert problem. In order to set up this second Lambert problem, the B-plane parameters of the flyby are calculated using the solution from the first Lambert problem. This can be done since the $\vec{V}_{\infty,a}$, calculated with Equation (2.5) is in fact the same as the $\vec{V}_{\infty,in}$ at the flyby B-plane. This is needed to calculate the velocity at pericentre of the flyby, using the following equation:

$$V_p = \sqrt{V_\infty^2 + \frac{2\mu}{r + h_p}} \tag{2.10}$$

Where r is the body radius, h_p is the flyby altitude and μ is the gravitational constant of the flyby body. However, since for this analysis it is assumed that the flyby body has a negligible mass, gravitational constant and radius, meaning the spacecraft will feel no gravitational pull from the target, the trajectory will not deflect during the flyby and will in fact travel in a straight line. This means that for this particular case the following relation holds, in the inertial frame with the flyby target as the origin:

$$\vec{V}_{\infty,in} = \vec{V}_{\infty,out} = \vec{V}_p \tag{2.11}$$

Then, the B_T and B_R parameters of the flyby B-plane are chosen in such a way that the desired flyby geometry is met, which is the driving factor for solving this second Lambert problem. The definitions of all the parameters of the B-plane can be seen in Figure 2.3.
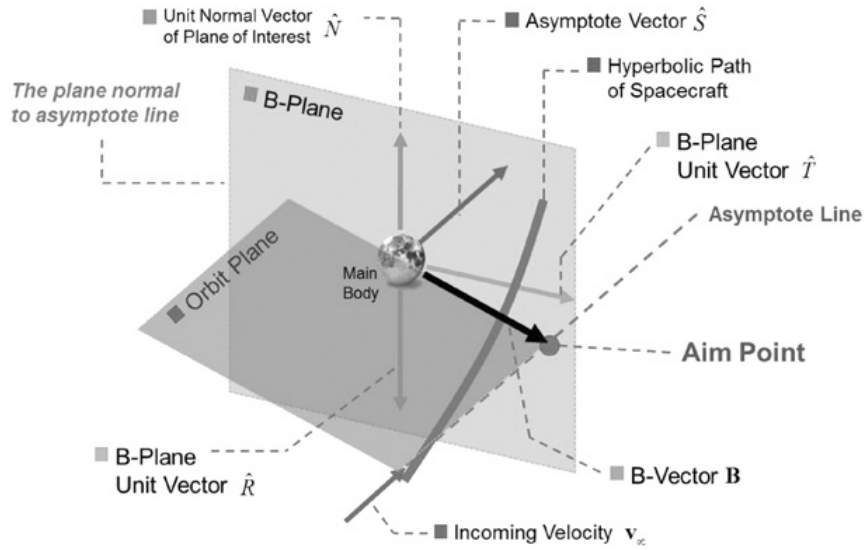
Figure 2.3: B-Plane Definition [25]

The relations between the impact parameter $\vec{B}$, also known as the miss parameter or the B-vector, its magnitude and its components are the following:

$$B_T = \vec{B} \cdot \hat{T} \tag{2.12}$$

$$B_R = \vec{B} \cdot \hat{R} \tag{2.13}$$

$$\vec{B} = B_T \cdot \hat{T} + B_R \cdot \hat{R} \tag{2.14}$$

$$B = \sqrt{B_T^2 + B_R^2} \tag{2.15}$$

A flyby distance of 600 km has been chosen for this analysis. The reason for this, is that the 1-σ uncertainty of Apophis's largest position component from JPL HORIZONS data is in the order of 200 km, which will be discussed later and can be seen in Table 3.4. A flyby distance of 600 km has thus been chosen since it equals more or less the 3-σ uncertainty which will ensure the spacecraft will not collide with the asteroid during the flyby. It would have been possible to select a gradually decreasing flyby distance for every subsequent flyby, but since the flyby velocity is quite high (as will be discussed further in Section 2.5) the actual flyby distance will not matter much, as the spacecraft will only be at that distance a fraction of a second. As will become clear in Section 2.4, the chosen flyby distance entails in all combination of the B_T and B_R parameters where one is 0 km and the other is either 600 or -600 km. The effects of the second and each additional flyby are of interest for this study. However, four or more flybys would entail in a long mission duration. For this reason it has been decided to perform this analysis for a total of three flybys.

2.4. High-Fidelity Trajectory Generation

The initial solutions from the porkchop plots are used to create more realistic high-fidelity ephemerides. This is done using NASA's General Mission Analysis Tool, or GMAT. As mentioned on GMAT's website: "GMAT is designed to model, optimise, and estimate spacecraft trajectories in flight regimes ranging from low Earth orbit to lunar applications, interplanetary trajectories, and other deep space missions."[7] The program is open source and available for free[8]. The scripting language is very similar to MATLAB and it is actually possible to link the program to MATLAB in order to use some of its internal routines, such as the well known FMINCON optimiser[9].

First, the used multiple shooting model will be introduced in Subsection 2.4.1, after which design choices for the model will be discussed in Subsection 2.4.2.

2.4.1. Multiple Shooting Model

The methods and routines used for this thesis's trajectory tool are heavily inspired from two tutorials available in the GMAT user guide: "Mars B-Plane Targeting"[10] and "Optimal Lunar Flyby using Multiple Shooting"[11] [26]. For this analysis, a trajectory optimisation method known as multiple shooting has been implemented. The idea is to efficiently solve the problem by breaking down the sensitive boundary value problem into smaller, less sensitive problems [26]. This is done by introducing patch and control points. Control points are fixed, from which the spacecraft is propagated both forward and backward. Patch points are flexible and are continuously shifted in order to find a valid solution. The idea is to match the state of the forward trajectory from a control point exactly with the state of the backwards trajectory from the next control point at the patch point in between the two control points. While this description may seem complex, it can be easily understood using Figure 2.4.

Figure 2.4: Multiple Shooting Method Basic Idea

The main steps of the model used for this thesis can be summarised as follows:

1. Vary all relevant variables: control epochs, elapsed days from control epochs to patch epochs, spacecraft states at the control epochs and TCM elements
2. Apply B-plane constraints
3. Forward and backward propagation from control points to patch points
4. Apply patching constraints
5. Minimise dV

The variation of a parameter simply entails in changing that parameter's value within the upper and lower bounds the parameter can be varied within. Applying B-plane constraints entails in the simple step of constraining the B_T and B_R values at the flyby control points. One of the analysis to be performed during the covariance analysis is the effect of the flyby geometry during the flyby, as will be discussed in Section 3.4. Therefore, four different cases have been set up targeting four points in the B-plane in order to be able to understand the effect of the flyby geometry on the covariance analysis results. These four cases are basically an arbitrary point in the B-plane at the chosen flyby distance and 90, 180 and 270 degrees rotated from that in the B-plane. To keep things simple, it has been decided to choose the points on the B-plane axes. Since the flyby distance has been selected to be 600 km, as will be discussed in Section 2.5, the four cases are (all units in km): $B_T = 600$ and $B_R = 0$, $B_T = -600$ and $B_R = 0$, $B_T = 0$ and $B_R = 600$ and finally $B_T = 0$ and $B_T = -600$. Visualisation of the four points will follow in Figure 2.10 in the results section.

The forward and backward propagation is the core of the multiple shootings method and has been discussed earlier in this section, recall Figure 2.4. Applying the patching constraints means the difference

---

of the spacecraft state after the forward and backward propagation is checked to be within the specified tolerance. In case this tolerance is met, it means that this solution will be the same as if one would propagate the spacecraft forward from one control point to the next one directly.

Finally, the dV is minimised. The model will often find a valid solution, but will keep iterating to find other viable solutions until the dV does not decrease anymore. A valid solution satisfies the set threshold accuracy of 10^{-4} km/s when patching, meaning the dV solution has an equal accuracy. Furthermore, the dV only contains the TCM burns and not the launch dV, as for this application it is assumed the launcher will put the spacecraft in a ballistic trajectory directly without the need of additional spacecraft burns. It should be noted that due to the nature of this complex problem, especially due to the many inputs and sensitivity of the model, the solver will usually find a local optimum rather than a global optimum.

2.4.2. Model Choices

The setup of the force model in GMAT is a powerful feature and has many options. The equations of motion are directly related to the force model choice. Since it was found that by using a complex force model straight away the model had trouble converging, the problem has been split in two iterations. The first iteration having a simple force model with only the central body as perturbing body and a second iteration with the Sun, Jupiter and Saturn as perturbing bodies, and including SRP effects. The respective equations of motion in heliocentric coordinates for the two force models are thus [27]:

$$\frac{d^2\vec{r}}{dt^2} = -\frac{\mu}{r^3}\vec{r} \tag{2.16}$$

$$\frac{d^2\vec{r}}{dt^2} = -\frac{\mu}{r^3}\vec{r} + G\sum_{\substack{k=1 \\ k \neq j}}^{n_b} m_k \left(\frac{\vec{r}_{ks}}{r_{ks}^3} - \frac{\vec{r}_{kj}}{r_{kj}^3} \right) + \frac{P_{SR}C_R A_\odot}{m_s}\hat{r}_{s\odot} \tag{2.17}$$

Since a quick convergence of the trajectory tool is desired as well as a physically realistic case, the three biggest gravitational perturbers (Sun, Jupiter and Saturn) as point masses and SRP have been chosen as the perturbations. The SRP model within GMAT can be either a complex so called SPAD (Solar Pressure and Aerodynamic Drag) model or a simple spherical model. While the SPAD model gives more realistic results, it requires the setup of a file that contains many specific spacecraft parameters about its size and attitude. Since at this stage nothing is yet known about the spacecraft size, the simple spherical SRP model is used instead, which models the solar effects on the spacecraft as if it were a sphere.

A Prince-Dormand 78 propagator is chosen, which is an adaptive step, eight order Runge-Kutta integrator with seventh order error control[12]. Other choices in GMAT are Runge-Kutta 89, Runge-Kutta 68, Runge-Kutta 56, Adams-Bashforth-Moulton, Prince-Dormand 853 and Prince-Dormand 45. Results for running the same scripts for all these propagators can be seen in Table 2.4. The run cases on the very left in this table are the several tutorials of GMAT. Since this analysis is based on the lunar flyby and the mars transfer, those numbers are relevant. It can be seen that for the mars transfer the Prince-Dormand 78 has the fastest run and the error is one of the smallest between all the integrators, while for the lunar flyby it has an average run time but has the smallest error of all. Furthermore, Prince-Dormand 78 can be considered the best all purpose integrator within GMAT[12]. From this short analysis it can be concluded that the Prince-Dormand 78 is in fact a very good integrator choice for the trajectory to be generated for this analysis.

TCMs are assumed to be impulsive burns for this model. The impulsive burns will later be replaced by finite burns in Section 4.4, but for the trajectories used in the covariance analysis of Chapter 3 only impulsive burns are considered. The coordinate system used throughout the whole model is the EME2000 inertial frame with the Sun as origin. A Sequential Quadratic Programming (SQP) algorithm is used for the solver, which is an iterative method for constrained nonlinear optimisation [28]. The SQP algorithm comes from the MATLAB interface, and uses FMINCON.

As mentioned in the previous section, a total of three flybys is chosen for this analysis. There are thus a total of four control points: the launch epoch and the three flyby epochs. This means there will be three patch points, one in between each set of control points. For this scenario it is chosen to perform

---

[12]http://gmat.sourceforge.net/doc/R2018a/html/Propagator.html, accessed 12-09-2018

Table 2.4: Comparison Data for GMAT Integrators [26]

		RKV89	RKN68	RK56	PD45	PD78	ABM	PD853
ISS	Run Time	1.53	**1.00**	2.14	2.78	1.46	3.41	1.80
	Error (m)	0.003	64.060	0.022	0.002	0.006	0.012	0.013
Molniya	Run Time	1.32	1.47	1.99	3.08	**1.00**	3.35	1.92
	Error (m)	0.007	0.601	0.059	0.032	0.043	380.125	0.031
Lunar Flyby	Run Time	**1.00**	1.01	2.26	2.98	2.21	3.30	1.39
	Error (m)	0.063	0.017	0.002	0.023	0.000	0.236	0.080
Mars Transfer	Run Time	1.02	1.04	1.14	1.40	**1.00**	3.07	1.11
	Error (m)	0.030	0.001	0.043	0.194	0.009	25.231	0.030
Finite burn 1	Run Time	1.27	**N/A**	1.24	1.26	**1.00**	1.45	1.07
	Error (m)	0.002	N/A	0.006	0.002	0.002	0.000	0.002
Finite burn 2	Run Time	1.03	**N/A**	1.18	1.31	**1.00**	1.54	1.12
	Error (m)	0.002	N/A	0.000	0.000	0.001	0.003	0.002

the small TCMs needed to retarget the spacecraft accurately for the next flyby at exactly the patch points. This means that the patch points are in fact, besides being the epochs where the states of the backward and forward propagation from two control points match, the solution epochs that will give the solution with the lowest dV needs. However, since it is assumed the launcher will put the spacecraft into a ballistic trajectory towards the asteroid, the TCM at the first patch point is optional and solutions for both the one with a TCM and without TCM are generated. This is the reason why for this convention the optional patch 1 TCM is called *TCM0* rather than *TCM1*, since if the TCM will not take place, the names of the following TCMs will stay the same and it is immediately clear at which patch point the TCM takes place without needing the knowledge of the patch 1 TCM taking place or not. There will thus be a total of either two or three TCMs. The whole sequence can be seen in the Figure 2.5, where the blue dots are the control points, the grey dots the patch points, the blue arrows forward propagations and the green arrows backward propagations.
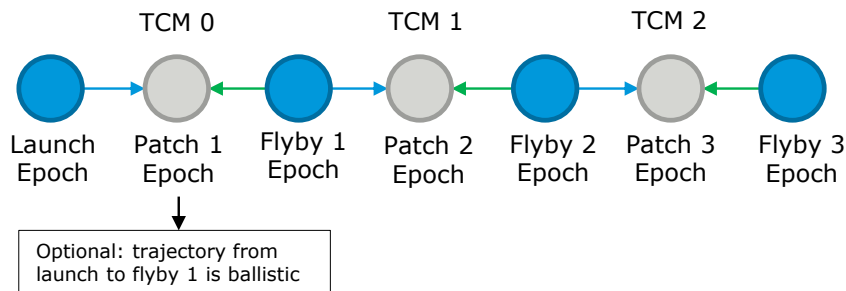
Figure 2.5: Mission Sequence with Multiple Shootings Method

2.5. Trajectory Results

In this section all the results from the trajectory analysis will be discussed. First all results concerning Apophis will be presented in Subsection 2.5.1, followed by results of asteroids UE34 and WN5 in Subsection 2.5.2.

2.5.1. Apophis

The initial guess solutions of Apophis generated with RESOTRAJ, using the methodology of Subsection 2.3.2, will now be presented. The resonance solutions in the porkchop plots are depicted with the red lines. The porkchop plot for zero number of complete orbital revolutions (nco0) is shown in Figure 2.6. In addition, the porkchop plots for the long and short solutions (recall Figure 2.1 for the definition of long and short solutions) for one complete orbital revolution (nco1l and nco1s) are also shown in Figures 2.7 and 2.8 for completeness.
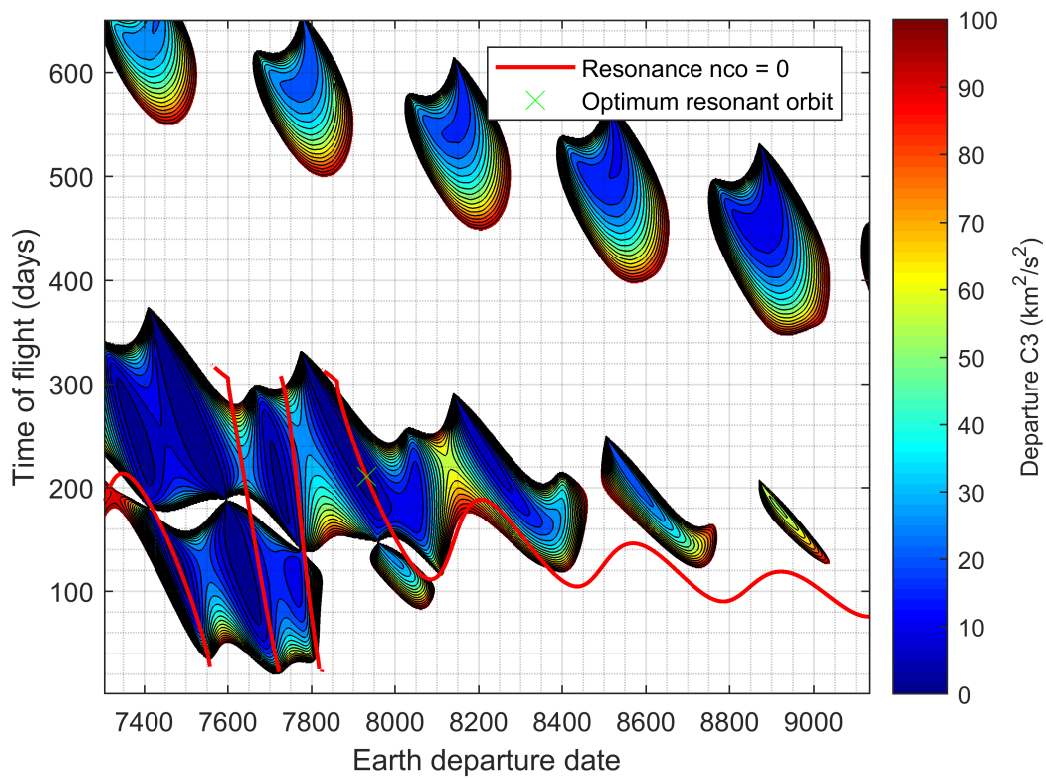
Figure 2.6: Apophis Porkchop Plot with Zero Orbital Revolutions
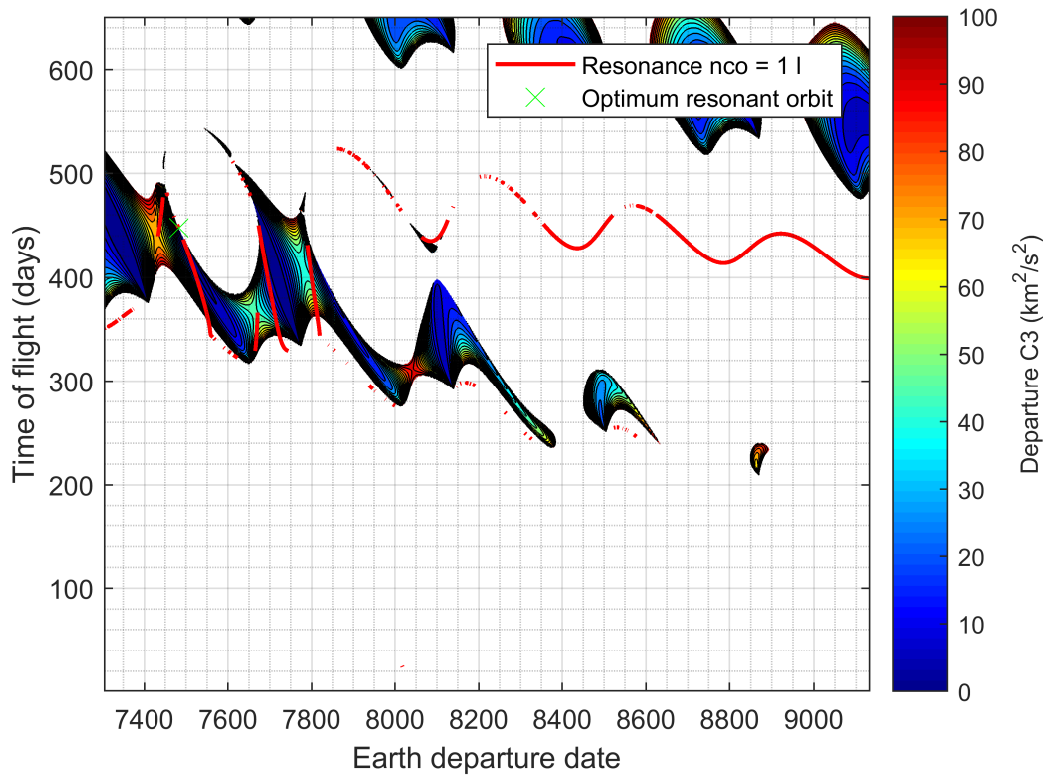
Figure 2.7: Apophis Porkchop Plot with One Orbital Revolution (Short Solution)
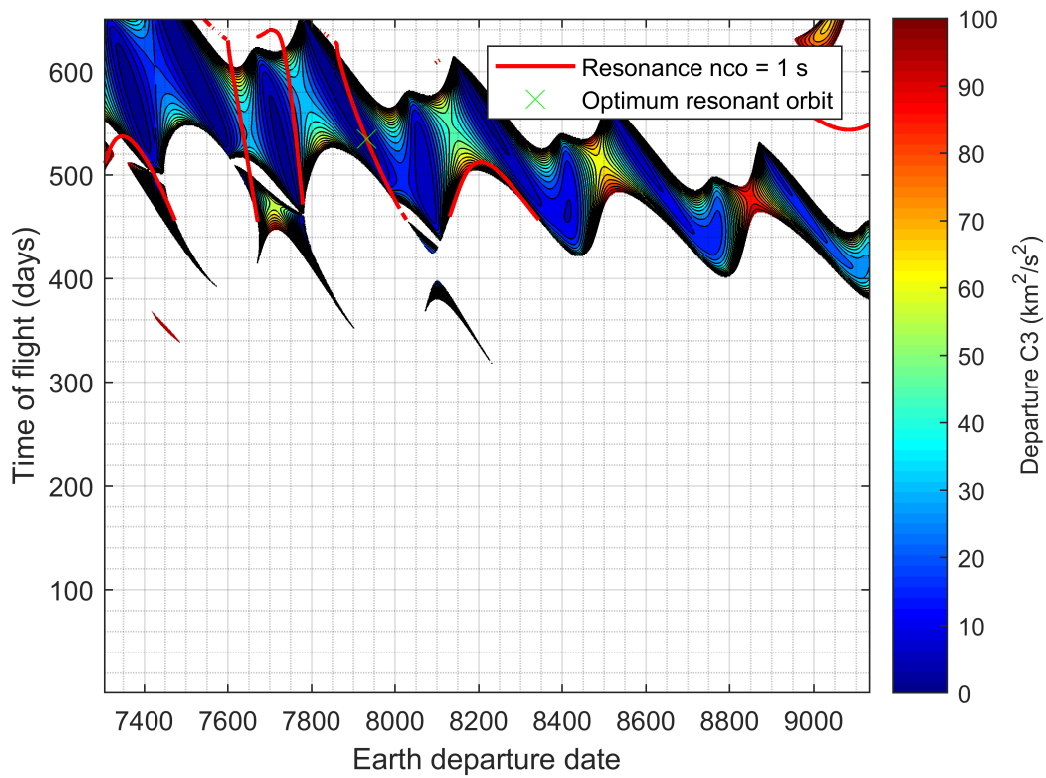
Figure 2.8: Apophis Porkchop Plot with One Orbital Revolution (Long Solution)

The most important parameters for the optimum solution for all three porkchop plots are summarised in Table 2.5, where E stands for epoch. The optimum solution is the result that has the lowest C_3 value.

Table 2.5: Apophis Optimum Solutions from RESOTRAJ

Solution	C_3 $[km^2/s^2]$	TOF [days]	Launch Epoch	Flyby 1 E	Flyby 2 E	Flyby 3 E
nco0	2.8912	210.7608	7931.7584 (18/09/2021)	8142.5192	8466.2386	8789.9580
nco1s	2.5724	447.6527	7482.4281 (26/06/2020)	7930.0808	8253.7501	8577.4193
nco1l	2.8912	534.4802	7931.7584 (18/09/2021)	8466.2386	8789.9580	9113.6774

The very feasible solution in the bottom left corner in Figure 2.6, with a TOF of about 100 days and Earth departure epoch around 7500, has been omitted from this table since the launch date is slightly too soon for the proposed mission to be developed and launched in time. Since a short time of flight is desired, nco0 is the preferred trajectory. The data from this solution, which includes in addition to the parameters of Table 2.5 the states of the spacecraft at the various epochs, is then passed onto GMAT for the high-fidelity trajectory optimisation. All relevant data results for the four Apophis nco0 trajectories are summarised in Table 2.6. The launch velocities are in heliocentric EME2000 coordinates, and $||V_s - V_e||$ (subscripts stand for spacecraft and Earth, respectively) shows the needed Earth escape dV.

Table 2.6: Apophis High-Fidelity Trajectory Results

	$B_T = 600$ $B_R = 0$	$B_T = -600$ $B_R = 0$	$B_T = 0$ $B_R = 600$	$B_T = 0$ $B_R = -600$
Epochs [MJD2000]				
Launch	7931.7599	7931.7565	7931.7578	7931.7577
Patch 1	8098.4737	8106.1405	8101.4782	8103.0016
Flyby 1	8142.5228	8142.5161	8142.5177	8142.5177
Patch 2	8276.6215	8268.3215	8258.5446	8250.9709
Flyby 2	8466.2616	8466.2557	8466.2572	8466.2573
Patch 3	8562.4476	8552.6850	8581.1950	8575.0170
Flyby 3	8790.0114	8790.0055	8790.0071	8790.0071
Launch Velocity [km/s, EME2000]				
V_x	1.8326	1.8336	1.8331	1.8332
V_y	26.3839	26.3839	26.3838	26.3839
V_z	10.2507	10.2508	10.2509	10.2507
$||V_s - V_e||$	1.7001	1.6998	1.6998	1.7000
TCM Velocities [m/s, EME2000]				
$TCM1_x$	0.5862	0.4590	0.4473	0.4189
$TCM1_y$	-0.1110	-0.1172	-0.1042	-0.0983
$TCM1_z$	-0.8015	-1.2314	-1.2331	-1.3227
$||TCM1||$	0.9992	1.3194	1.3159	1.3910
$TCM2_x$	0.1198	0.0924	0.1625	0.1724
$TCM2_y$	-0.0322	-0.0323	-0.0374	-0.0355
$TCM2_y$	-0.5771	-0.6477	-0.4304	-0.4015
$||TCM2||$	0.5903	0.6551	0.4616	0.4384
Total TCMs	1.5895	1.9745	1.7776	1.8294

Visualisation of the four trajectories can be seen in Figure 2.9.
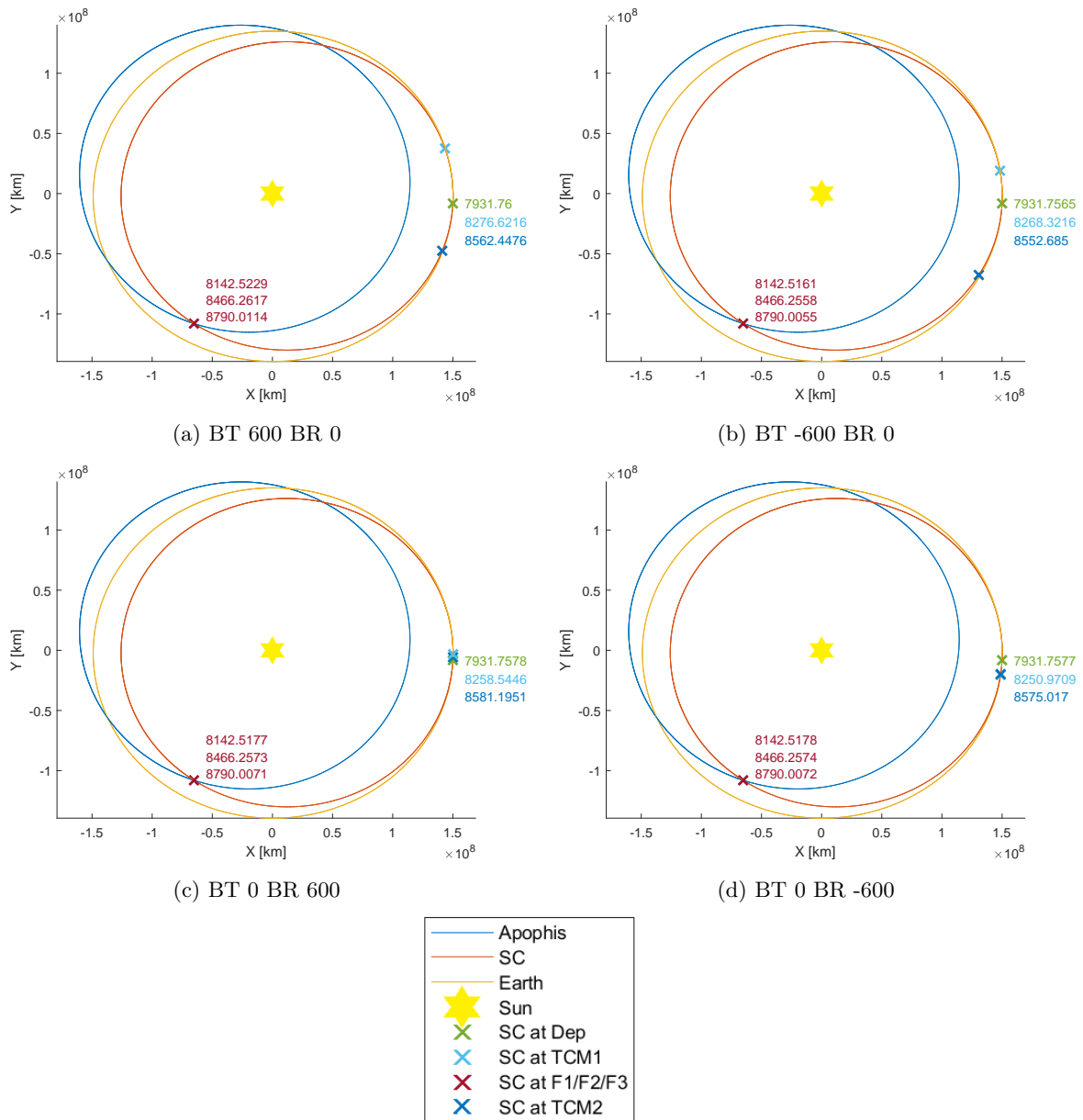
Figure 2.9: Apophis Trajectories

While these solutions seem correct, it is important to do a precise final verification check using SPICE in MATLAB at the flyby epoch itself to see whether the trajectories in fact target the correct point in the B-plane. This is done by loading the solution kernel in MATLAB and performing B-plane calculations at the flyby epochs. The results for the first flyby can be visualised in Figure 2.10.
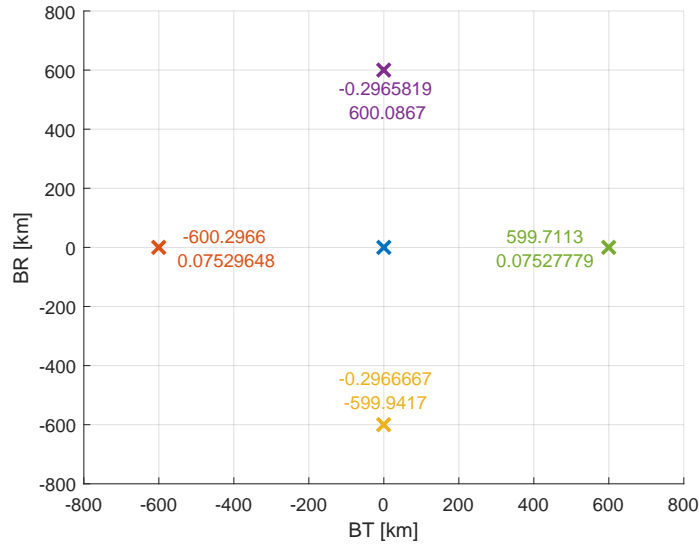
Figure 2.10: Apophis Trajectory B-plane Verification - First Flyby

As can be seen, the values do not exactly correspond to 600, -600 and 0 km, which GMAT optimised for. This has been repeated for the second and third flybys, and the discrepancies between the values has been tabulated in Table 2.7.

Table 2.7: GMAT and MATLAB Verification B-plane Values [km]

		$B_T = 600$ $B_R = 0$	$B_T = -600$ $B_R = 0$	$B_T = 0$ $B_R = 600$	$B_T = 0$ $B_R = -600$
		Flyby 1			
B_T	GMAT	600.0000	-600.0000	0.0000	-0.0000
	Verification	599.7113	-600.2966	-0.2965	-0.2966
B_R	GMAT	-0.0000	0.0000	599.9999	-599.9999
	Verification	0.0752	0.0752	600.0867	-599.9417
		Flyby 2			
B_T	GMAT	600.0004	-600.0000	0.0000	0.0000
	Verification	599.6969	-600.3055	-0.3047022	-0.3047
B_R	GMAT	-0.0000	-0.0000	599.9999	-600.0000
	Verification	0.1017	0.1018	600.1145	-599.8982
		Flyby 3			
B_T	GMAT	600.0008	-600.0006	-0.0020	-0.0016
	Verification	599.6843	-600.3454	-0.3214	-0.3210
B_R	GMAT	-0.0007	0.0000	600.0003	-599.9997
	Verification	0.1208	0.1216	600.1347	-599.8951

As can be seen, the values have a discrepancy in the order of magnitude of 100 meters. In order to determine whether this discrepancy is acceptable, the flyby velocity has to be determined. The flyby velocity is dependent of the solution set from the porkchop plot and cannot be altered or constrained, as any alteration would cause the spacecraft and the asteroid to not be in resonance anymore. The velocities for every flyby have been tabulated in Table 2.8.

Table 2.8: Apophis Flyby Relative Velocities [km/s]

	Flyby 1	Flyby 2	Flyby 3
$B_T = 600$, $B_R = 0$	8.7343	8.7332	8.7319
$B_T = -600$, $B_R = 0$	8.7340	8.7327	8.7313
$B_T = 0$, $B_R = 600$	8.7341	8.7326	8.7313
$B_T = 0$, $B_R = -600$	8.7341	8.7325	8.7311

Since in this particular case the relative velocity of the spacecraft with respect to Apophis is roughly 8.73 km/s, those about 100 meters discrepancy will not matter since it corresponds with the distance travelled in roughly 0.01 seconds. What is more important is proving that with these trajectories the spacecraft performs an actual flyby with the asteroid at the specified epoch and is in fact in a resonance with the asteroid, which has been proved to be the case in this section. Note that the relative velocities of the four Apophis trajectories are quite high, meaning the proposed trajectories would be on the borderline of being realistic for a real mission.

2.5.2. UE34 and WN5

Now that Apophis has been discussed, the results for asteroids UE34 and WN5 presented as well. Only the porkchop plots for zero orbital revolutions are shown in order to keep these results concise, and can be seen in Figures 2.11 and 2.12.
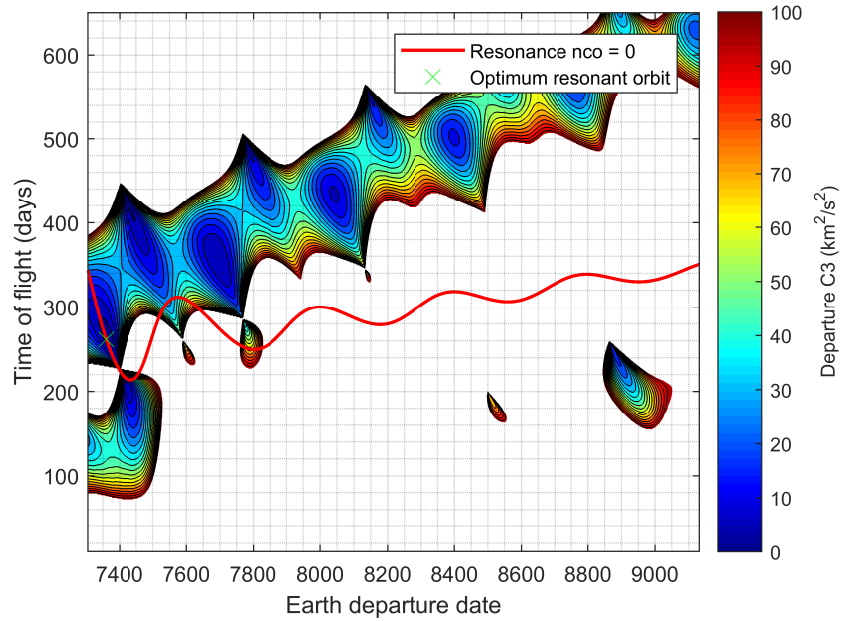
Figure 2.11: UE34 Porkchop Plot with Zero Orbital Revolutions
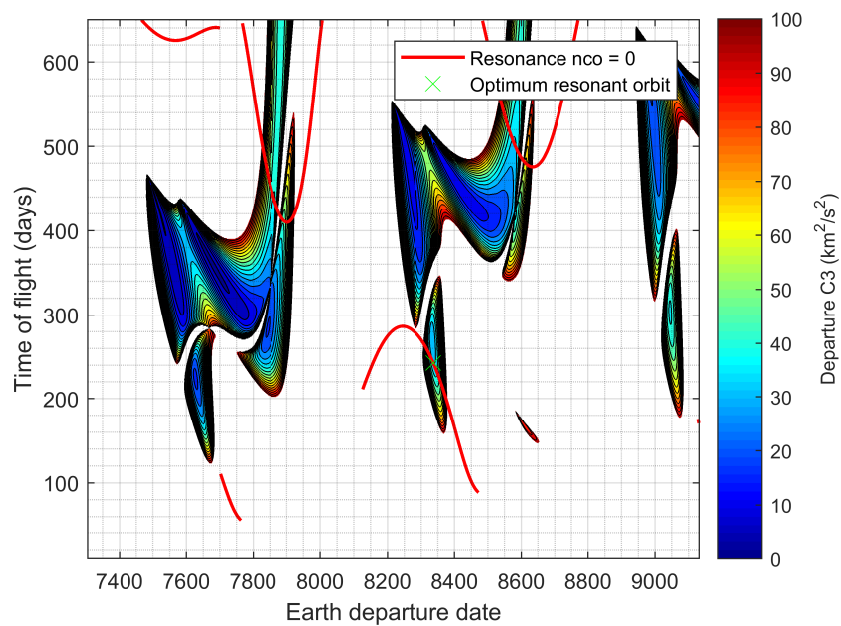
Figure 2.12: WN5 Porkchop Plot with Zero Orbital Revolutions

The main data of the high-fidelity GMAT trajectories that follow from these porkchop plot solutions is summarised in Table 2.9, while the visualisation of the trajectories can be seen in Figures 2.13 and 2.14 for asteroids UE34 and WN5, respectively.

Table 2.9: UE34 and WN5 High-Fidelity Trajectory Results

	UE34	WN5
Epochs [MJD2000]		
Launch	7360.57	8336.49
Patch 1	7410.19	8551.95
Flyby 1	7621.97	8579.20
Patch 2	7668.52	8690.79
Flyby 2	8046.51	9397.31
Patch 3	8056.83	9661.06
Flyby 3	8471.03	10215.44
Launch Velocity [km/s, EME2000]		
V_x	-12.3469	-20.2756
V_y	-26.2053	27.5852
V_z	-12.2811	9.7655
$\|\|V_s - V_e\|\|$	1.7835	5.9312
TCM Velocities [m/s, EME2000]		
$TCM0_x$	-0.2238	6.0582
$TCM0_y$	0.0468	-8.1450
$TCM0_z$	0.2428	-0.1254
$\|\|TCM0\|\|$	0.3335	10.1518
$TCM1_x$	0.8181	-7.3429
$TCM1_y$	1.2871	0.6893
$TCM1_y$	2.4001	5.3751
$\|\|TCM1\|\|$	2.8437	9.1261
$TCM2_x$	-0.4216	2.1630
$TCM2_y$	1.1120	-0.2094
$TCM2_y$	3.5540	-19.2549
$\|\|TCM2\|\|$	3.7477	19.3772
Total TCMs	6.9250	38.6552

WN5 turns out to be a rather unfeasible option, both in terms of orbital elements (high eccentricity and orbital period, recall Table 2.2) and spacecraft trajectory. The latter becomes clear from the data of Table 2.9: the high needed launch *dV* of 5.93 km/s and total TCM *dV* of 38.66 m/s, especially when compared to the Apophis (launch of 1.70 km/s and TCMs of roughly 1.80 m/s) and UE34 (launch of 1.78 km/s and TCMs of 3.75 m/s) trajectories, make this option not quite attractive. Therefore the covariance analysis is based primarily on the Apophis trajectories, while the WN5 case is kept as a bonus case.
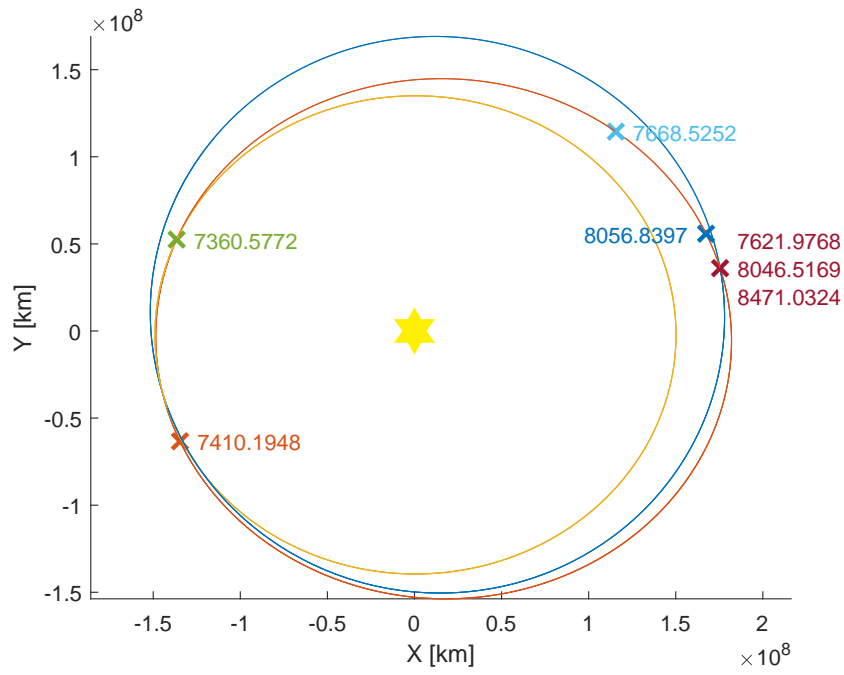
Figure 2.13: UE34 Trajectory
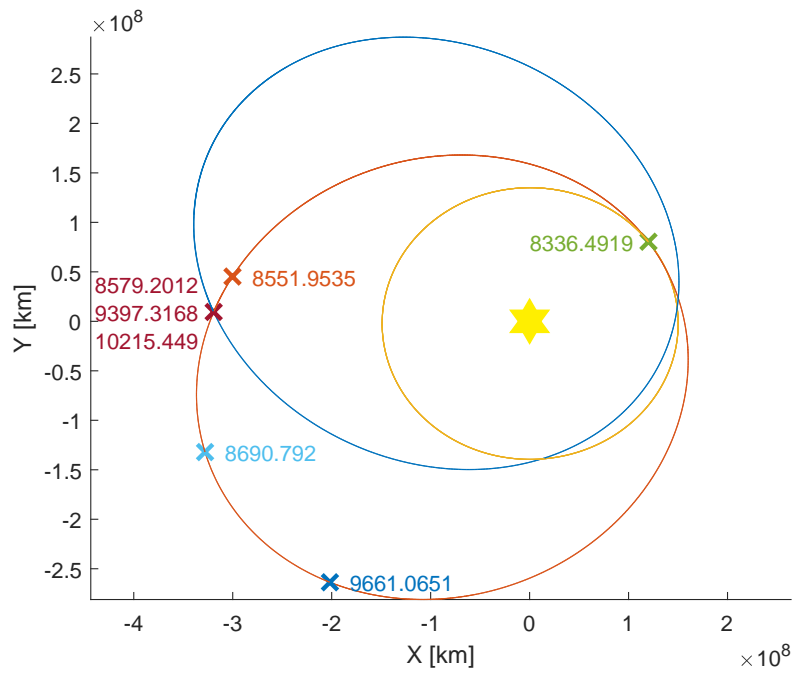
Figure 2.14: WN5 Trajectory
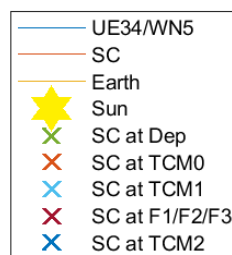
Finally, the flyby velocities at the closest approach will be discussed. In Table 2.10 all the relative velocities of the spacecraft with respect to the target asteroid are tabulated at the three flybys. The flyby velocity of UE34 is fairly low, which is favourable and realistic, while the relative velocity for WN5 is very high and not realistic at all, but since WN5 is considered a bonus study case the trajectory is used nonetheless for the covariance analysis.

Table 2.10: UE34 and WN5 Flyby Relative Velocities [km/s]

	Flyby 1	Flyby 2	Flyby 3
UE34	5.411	5.5424	5.5416
WN5	13.4427	13.4598	13.4435

To summarise this chapter, several 1:1 resonant trajectories have been generated to perform flybys at a distance of 600 km to asteroids Apophis, UE45 and WN5. For the trajectory to Apophis four different points in the B-plane have been targeted: $B_T = 600$ and $B_R = 0$, $B_T = -600$ and $B_R = 0$, $B_T = 0$ and $B_R = 600$ and finally $B_T = 0$ and $B_T = -600$. Results from the Lambert's problem to these asteroids have been visualised in porkchop plots, in combination with resonance data, to generate a robust first guess. This first guess is then used in a GMAT script that implements the multiple shooting method in order to find a high-fidelity trajectory. The force model of this trajectory entails in the Sun, Jupiter and Saturn as point masses, and includes SRP effects. The trajectories found for Apophis and UE34 are near-circular and around 1 AU, while the trajectory to WN5 is highly elliptical reaching roughly 2 AU. The TCMs that are needed to reach Apophis, UE34 and WN5 are roughly 2 m/s, 7 m/s and 39 m/s, respectively. The relative flyby velocities for the generated trajectories are 8.73 km/s, 5.54 km/s and 13.46 km/s, respectively.

3

Asteroid Orbit Determination

Now that the trajectory generation and results have been discussed in detail, it is time to present the asteroid orbit determination by means of a covariance analysis. The goal of this covariance analysis, using the generated trajectory kernels discussed in Chapter 2 as in puts, is to understand whether a flyby mission in a resonant orbit with the target asteroid is a feasible option to improve the asteroid position knowledge, in order to decrease the uncertainties of a potential impact with Earth. The covariance analysis is performed using a tool written in MATLAB called GALICOV (Galilean Covariance), written by ESOC mission analyst Waldemar Martens for ESA's JUICE (Jupiter Icy Moons Explorer) mission. The orbit determination model will be discussed in detail in Section 3.2. Then, the three-step verification and validation of the model will follow in Section 3.3. Finally, the results of several case studies will be presented in Section 3.4. But before discussing the orbit determination model, the reference frames and rotations matrices used throughout this chapter will be discussed in Section 3.1.

3.1. Reference Frames

It is important to clarify which reference frames are used throughout the model. All the references frames used for this chapter, including the orientation of its axes, are summarised in Table 3.1, where Centre of Mass is abbreviated with CoM and the type states whether it is an inertial or fixed frame.

Table 3.1: Summary of Reference Frames

Frame Name	Type	Origin	Axes Orientation
EME2000	I	Sun	x: along first point of Aries y: complete right-handed coordinate system z: normal to celestial equatorial plane
ECEF	F	Earth	x: towards intersection of equatorial plane and Greenwich meridian y: complete right-handed coordinate system z: normal to equatorial plane
SCI	I	Spacecraft CoM	x: along first point of Aries y: complete right-handed coordinate system z: normal to celestial equatorial plane
CAM	F	Camera CCD Centre	x: along projection of Sun into focal plane y: complete right-handed coordinate system z: along spacecraft-Earth axis
RADEC	I	Spacecraft CoM	x: along EME2000 RA direction y: along EME2000 DEC direction z: along spacecraft-Earth axis
TNW	F	Body CoM	T: along velocity vector N: complete right-handed coordinate system (should be along $\mathbf{W} \times \mathbf{T}$ vector) W: along the orbital angular momentum vector (should be perpendicular to orbital plane)
RST/QSW/RTN	F	Body CoM	R: along radius vector S: along the orbital angular momentum vector (should be perpendicular to orbital plane) T: complete right-handed coordinate system (should be along $\mathbf{T} \times \mathbf{R}$ vector)
B-Plane/TRS	F	Body CoM	$\hat{S}$: parallel to infinite velocity vector $\hat{T}$: perpendicular to $\hat{S}$ and in the equatorial plane of flyby body $\hat{R}$: complete right-handed coordinate system

Important is to know the relations between some of these frames, as data will often be transformed to another coordinate system in the model. One way to do this is using a transformation matrix. This is particularly useful since the data can be transformed in both directions using a single matrix. For example, to transform matrix $\mathbf{D}$ from coordinate system A to coordinate system B and the other way around, the following transformations are used:

$$\mathbf{D}_B = \mathbf{R}_{A \to B} \mathbf{D}_A \mathbf{R}_{A \to B}^T \tag{3.1}$$

$$\mathbf{D}_A = \mathbf{R}_{A \to B}^T \mathbf{D}_B \mathbf{R}_{A \to B} \tag{3.2}$$

In this equation $\mathbf{R}_{A \to B}$ is a rotation matrix from frame A to frame B, and the subscript of $\mathbf{D}$ denotes its frame. Note that the transformation matrices discussed in this section are all 3×3 matrices that can be used to transform both the position and velocity vectors. Four frequently used transformations will be discussed using this approach. The first, and most complex, is the rotation from the CAM frame to the RADEC frame, which is particularly of interest during the optical navigation calculations in Subsection 3.2.1. In order to do this, two transformations take place:

$$\mathbf{R}_{CAM \to RADEC} = \mathbf{R}_{RADEC \to EME2000}^T \mathbf{R}_{CAM \to EME2000} \tag{3.3}$$

The transformation, which is derived in Appendix A, can be written as:

$$\mathbf{R}_{CAM \to RADEC} = \left[\begin{pmatrix} -\sin(\alpha) \\ \cos(\alpha) \\ 0 \end{pmatrix}, \hat{r} \times \begin{pmatrix} -\sin(\alpha) \\ \cos(\alpha) \\ 0 \end{pmatrix}, \hat{r} \right]^T \cdot \left[\frac{(\vec{e} \times \vec{s}) \times \vec{e}}{||(\vec{e} \times \vec{s}) \times \vec{e}||}, \frac{\vec{e} \times \vec{s}}{||\vec{e} \times \vec{s}||}, \vec{e} \right] \tag{3.4}$$

The second transformation that will be discussed, is the inertial EME2000 to RST, which is especially useful for transforming a priori covariance data. Three equations are needed for this computation:

$$\vec{R} = \frac{\vec{r}}{||\vec{r}||} \tag{3.5}$$

$$\vec{T} = \frac{\vec{R} \times \vec{v}}{||\vec{R} \times \vec{v}||} \tag{3.6}$$

$$\vec{S} = \vec{T} \times \vec{R} \tag{3.7}$$

The rotation matrix is then, where inertial has been dubbed IN:

$$\mathbf{R}_{IN \to RST} = \left[\vec{R}, \vec{S}, \vec{T} \right]^T \tag{3.8}$$

The inertial EME2000 to B-plane (or TRS) transformation is also used frequently, especially during post-processing of the results. This can be calculated using:

$$\vec{S} = \frac{\vec{V}_\infty}{||\vec{V}_\infty||} \tag{3.9}$$

$$\vec{T} = \frac{\vec{V}_\infty \times \vec{P}}{||\vec{V}_\infty \times \vec{P}||} \tag{3.10}$$

$$\vec{R} = \vec{S} \times \vec{T} \tag{3.11}$$

where $\vec{P}$ is a vector denoting the orientation of the north pole of the flyby body in the inertial frame. For this study the orientation of the Earth pole at J2000 in EME2000 is used, which is:

$$\vec{P} = [0, 0, 1]^T \tag{3.12}$$

Recognising that $\vec{S}$, $\vec{T}$ and $\vec{P}$ are in fact all three units vectors, they can thus also be referred to as $\hat{S}$, $\hat{T}$ and $\hat{P}$. The latter notation will be used in Subsection 3.2.6. The rotation matrix for this transformation is then

$$\mathbf{R}_{IN \rightarrow TRS} = \left[\vec{T}, \vec{R}, \vec{S} \right]^T \tag{3.13}$$

Finally, the inertial EME2000 to TNW transformation is frequently used as well during post-processing of the results. This is calculated using the following equations:

$$\vec{T} = \frac{\vec{V}}{||\vec{V}||} \tag{3.14}$$

$$\vec{W} = \frac{\vec{r} \times \vec{T}}{||\vec{r} \times \vec{T}||} \tag{3.15}$$

$$\vec{N} = \vec{W} \times \vec{T} \tag{3.16}$$

The rotation matrix is

$$\mathbf{R}_{IN \rightarrow TNW} = \left[\vec{T}, \vec{N}, \vec{W} \right]^T \tag{3.17}$$

3.2. Orbit Determination Methodology

This section will describe in great technical detail the methodology for orbit determination used in this thesis. Methodology and equations are explained as much as possible rather than GALICOV implementation, but some information regarding implementation is necessary to fully understand the model. The optical navigation and ground station scheduling methods will be analysed in Subsections 3.2.1 and 3.2.2, respectively. The equations of motion and the derivation of the variational equations will be discussed in Subsection 3.2.3, followed by a discussion of additional essential modelling in Subsection 3.2.4, such as the way Non-Gravitational Accelerations (NGAs) are implemented. The covariance analysis itself, including the used filtering technique, follows in Subsection 3.2.5. Finally, all used post-processing methods of the covariance matrix, such as generating the covariance error ellipse, are discussed in Subsection 3.2.6 followed by all the inputs necessary for the tool to be run, including recurring input values, in Subsection 3.2.7.

3.2.1. Optical Measurements and Scheduling

To generate an optical measurement schedule, several constraints have to be set up. For an asteroid flyby case, the three most important constraints are the Sun exclusion angle, the phase angle and the visibility. The Sun exclusion angle is the angle between Sun, spacecraft and asteroid. In order to have a good optical measurement, it is important that camera is not blinded by the Sun. If this angle is too small, the camera will be facing directly into the Sun. It is therefore important to set a minimum constraint for this angle. The phase angle on the other hand is the angle between Sun, asteroid and spacecraft. It is used to determine whether the spacecraft is not positioned on the dark side of the asteroid (eclipse), since a completely black image will be useless. It is therefore important setting a maximum on this angle, in order to make sure at least a part of the asteroid will be visible. Lastly, the visibility of the asteroid is whether the asteroid itself is visible enough at the moment of the optical measurement. In other words, it is a measure for the luminosity of the asteroid. For this analysis, the visibility constraint will be determined using the apparent magnitude. The calculations for all constraints will now be discussed.

The method for calculating the Sun exclusion angle and the phase angle is the same, since for both the angle between two vectors needs to be calculated. For the Sun exclusion angle the angle between $\vec{r}_{sc/a}$ and $\vec{r}_{sc/S}$ has to be calculated, where subscripts a, sc and S stand for asteroid, spacecraft and Sun, respectively. For the phase angle the angle between vectors $\vec{r}_{a/S}$ and $\vec{r}_{a/sc}$ needs to be calculated. To generalise the equations, the subscripts are replaced by i, j and k. The angle α between $\vec{r}_{ij}$ and $\vec{r}_{ik}$ thus needs to be calculated. Starting from the very basics, these vectors are simply:

$$\vec{r}_{ij} = \vec{r}_j - \vec{r}_i \tag{3.18}$$

$$\vec{r}_{ik} = \vec{r}_k - \vec{r}_i \tag{3.19}$$

First, the cosine of the angle is calculated, by computing the dot product:

$$\cos \alpha = \vec{r}_{ij} \cdot \vec{r}_{ik} \tag{3.20}$$

Since for small angles the cross product is much more precise than the dot product, it has to be checked whether the angle is close to either 0 or π. If this is the case, the cross product is calculated:

$$\sin \alpha = \vec{r}_{ij} \times \vec{r}_{ik} \tag{3.21}$$

For angles sufficiently far away from 0 or π, α is simply calculated by taking the inverse cosine of the dot product. For angles close to 0, to calculate α the inverse sine is taken of the cross product, while for angles close to π, the inverse sine of the cross product is subtracted from 180 degrees to yield α.

The visibility constrained is calculated using the apparent magnitude. The apparent magnitude (m) is calculated as follows[1]:

$$m = H + 2.5 \log_{10} \left(\frac{r_{BS}^2 r_{BO}^2}{p(\chi) r_0^4} \right) \tag{3.22}$$

where H is the absolute magnitude, which is the visual magnitude an observer (in this case the spacecraft) would record if the body (in this case the asteroid) was placed at exactly 1 AU away from both the observer and the Sun while being at a zero phase angle[2]. The parameters r_{BS} and r_{BO} are the scalar distances between body and Sun, and body and observer, respectively, and r_0 equals 1 AU. Finally, $p(\chi)$ is the phase integral, which in this case is approximated as an ideal diffuse reflecting sphere using

$$p(\chi) = \frac{2}{3} \left[\left(1 - \frac{\chi}{\pi} \right) \cos \chi + \frac{1}{\pi} \sin \chi \right] \tag{3.23}$$

For a phase angle between 0 and 180 degrees, which is applicable for this case, the phase integral ranges from roughly 2/3 to 0, see Figure 3.1.
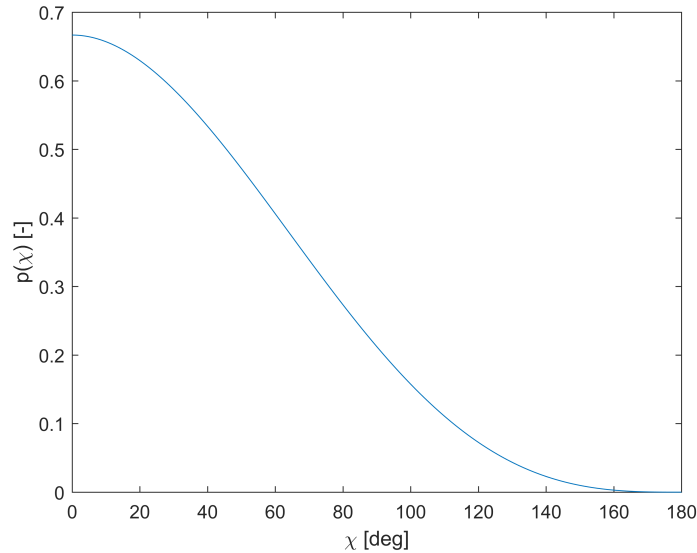
Figure 3.1: Phase Integral

The phase integral is a way to account for both light diffusion and for the fact that only a part of the object might be visible when pointing towards it, depending on the phase angle which is based on the orientation of the spacecraft and asteroid at a determined epoch. The separate effect of these two and

[1]https://comethunter.lamost.org/scwrk/THECAL/opam.pdf, accessed 03-12-2018
[2]https://cneos.jpl.nasa.gov/glossary/h.html, accessed 22-09-2018

the combined effect can be seen in Figure 3.2. Note that the asteroid is modelled as a perfect sphere for this study, which is however almost never the case for an asteroid. Since data regarding shape will not be available for the asteroid until very close encounter, modelling the asteroid as a perfect sphere is a valid first approximation.

(a) Shadow and Light Side   (b) Light Diffusion[3]   (c) Combined[3]
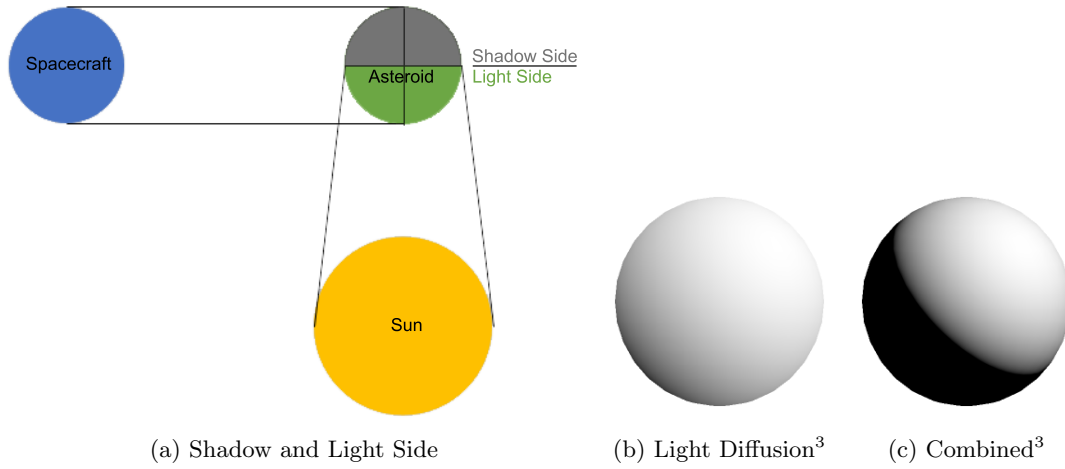
Figure 3.2: Phase Integral Effect

The effect of light diffusion can be seen very clearly from Figure 3.1: even for a zero phase angle, thus where the spacecraft sees the the light side of the asteroid completely, the phase integral equals about 2/3. For the absolute magnitude, the value found on the HORIZONS page of the specific asteroid is used, which can be found in Table 2.2.

Conservative values for minimum Sun exclusion angle (30 degrees) and maximum phase angle (150 degrees) have been used [29]. While for the visibility a maximum value of 8.5 mag has been used, to be conservative as well since an asteroid will become somewhat visible at roughly 9 to 9.5 mag [30] [31]. Because of the logarithmic scale, the lower the magnitude the more visible it will be. For most cases, an interval between optical measurements of 30 minutes has been used, but other intervals have been experimented with as well, as will become clear in Section 3.4.

A last step is to compute the weights for all optical measurements, and then filter all the measurements according to their kilometric weight. The lower the weight of the measurement, the more it will have an impact on the covariance analysis. Since no Image Processing (IP) model has been used for this analysis, as will be discussed in Subsection 3.2.7, the IP covariance matrix simply equals a matrix with the constant value of the optical measurement noise on the diagonal. However, these values are in the RADEC frame, and need to be transformed to the CAM frame in order to be meaningful. This is done by combining Equation (3.4) with Equation (3.2) to yield the following

$$\mathbf{IP}_{CAM} = \mathbf{R}_{CAM \to RADEC}^{T} \cdot \mathbf{IP}_{RADEC} \cdot \mathbf{R}_{CAM \to RADEC} \tag{3.24}$$

To extract the weights in degrees, $\mathbf{W}_{deg}$, the square root of the diagonal values have to be taken from the IP covariance matrix. To get the weights in terms kilometres, the following relation hold:

$$\mathbf{W}_{km} = \sin\left(\mathbf{W}_{deg}\right) \cdot \vec{r}_{a,sc} \tag{3.25}$$

where $\vec{r}_{a,sc}$ is the position vector of the spacecraft with respect to the asteroid. Now that all measurements have been assigned a kilometric weight, it is checked against the maximum weight of a measurement. Only keeping measurements with a kilometric lower than 20 km has shown to give good results and has been used throughout this study [32].

---

[3]http://blog.stevemcauley.com/2011/12/03/energy-conserving-wrapped-diffuse/, accessed 24-09-2018

3.2.2. Radiometric Measurements and Scheduling

Combining radiometric measurement of the spacecraft from Earth with optical measurements of the asteroid from the spacecraft is of crucial importance, since a link can then be created from the Sun all the way to the asteroid. This link can be visualised in Figure 3.3.
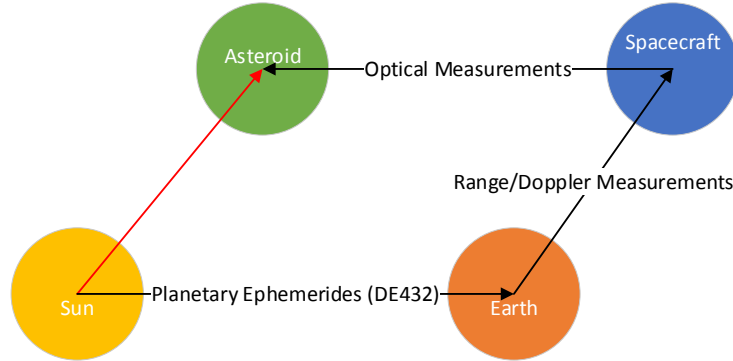
Figure 3.3: Link between Measurements

In the covariance analysis, discussed in Subsection 3.2.5, both the radiometric and optical measurements will be processed in order to improve the asteroid orbit knowledge (the red arrow in Figure 3.3). As will become clear in Subsection 3.2.5, for this study no optical, range or Doppler measurements are actually modelled, which is why no equations for observations are discussed in this subsection. Only the partials of these measurements will be needed for the filtering, which are derived in Appendix B.

Measuring the time it takes for the radio signals to travel to and from a spacecraft gives the distance to the GS (two-way range measurement), while measuring the signal's Doppler shift provides the spacecraft's velocity along that Line of Sight (two-way Doppler measurement). Light time effects have been taken into account. The calculations for spacecraft visibility times from the GS will now be discussed. It is assumed that the time the spacecraft receives the signal (which is also the time the spacecraft resends the signal) is known. The times the GS transmits (t_1), the spacecraft sends and receives (t_2) and the GS receives (t_3) the signal back are then:

$$t_1 = t_2 - \frac{||\vec{r}_{sc} - \vec{r}_{GS,t1}||}{c} \tag{3.26}$$

$$t_3 = t_2 + \frac{||\vec{r}_{sc} - \vec{r}_{GS,t3}||}{c} \tag{3.27}$$

where c is the speed of light and the position vector $\vec{r}_{GS}$ is the position of the GS in EME2000, which is determined with SPICE routines and GS orientation data. The transmit and receive times of the signal are then used to calculate the elevation of the spacecraft at those times. Only measurements for which the GS elevation is 10 degrees or higher are taken into account.

Visibility occultation is discussed next. To calculate the occultation, two angles are needed: the apparent radius of the occulting body as seen from the spacecraft (here arbitrarily called α) and the apparent angular distance from the GS to the occulting body as seen from the spacecraft (arbitrarily called β). This is calculated as follows:

$$\alpha = \sin^{-1}\left(\frac{r_{ob}}{||\vec{r}_{sc,bo}||}\right) \tag{3.28}$$

$$\beta = \cos^{-1}\left(\frac{\vec{r}_{sc,GS} \cdot \vec{r}_{sc,bo}}{||\vec{r}_{sc,GS}|| \cdot ||\vec{r}_{sc,bo}||}\right) \tag{3.29}$$

where r_{ob} is the radius of the occulting body and $\vec{r}_{sc,bo}$ and $\vec{r}_{sc,GS}$ the vectors from the spacecraft to the occulting body and GS, respectively, both in the Earth-fixed frame. The view from the spacecraft to the GS is blocked in case $\alpha > \beta$. Occultation is calculated for the transmitting and receiving signal. For this study, only the Sun is taken as the occulting body.

Now that the visibility times and occultation epochs have been calculated, the radiometric schedule can be generated. The radiometric measurement frequency has been chosen to be 1 hour for most study cases in this thesis, which will be discussed in Subsection 3.2.7.

3.2.3. Equations of Motion and Variational Equations

Since it is a complex task to solve the state variables of a body directly from a given set of observations and the model for the motion of the body, it is customary to linearise the relation between the observables and the independent parameters in order to obtain simplified expressions that can be solved more easily. In order to do this, the State Transition Matrix (STM) and variational equations are introduced. This subsection relies heavily on equations and theory from Satellite Orbits by Montenbruck [33] and Statistical Orbit Determination by Tapley [34].

While modelling the STM was not part of this thesis, as it was already available in ESOC's flight dynamics infrastructure, it is a vital part of the model, and the fundamentals will be discussed without going into too much detail. First, the equations of motion have to be discussed. For a model where an asteroid orbits the Sun, it is sufficient to model the planets in the system as point masses. Non-gravitational perturbations are not incorporated in the equations of motion. The way these are modelled will be discussed in Section 3.2.4. The equation of motion is thus rather basic:

$$\frac{d^2\vec{r}}{dt^2} = -\frac{\mu}{r^3}\vec{r} + G\sum_{\substack{k=1\\k\neq j}}^{n_b} m_k \left(\frac{\vec{r}_{ks}}{r_{ks}^3} - \frac{\vec{r}_{kj}}{r_{kj}^3}\right) \tag{3.30}$$

The central body of this equation of motion is the Sun. Additional point masses present in the model are Jupiter, Saturn and Earth. The gravitational pull of both the spacecraft and asteroid is negligible.

The STM and variational equations will now be discussed. The idea of the State Transition Matrix is to relate a small initial displacement to displacements in the final state. When the equations of motion for the STM contain more than just the central body as perturbation, it is a hard task to compute the STM analytically, so it is computed numerically instead. This is done by differentiating the State Transition Matrix:

$$\dot{\mathbf{\Phi}}(t, t_0) = \mathbf{F}\,\mathbf{\Phi}(t, t_0) \tag{3.31}$$

Where $\mathbf{\Phi}$ is the STM and $\mathbf{F}$ is called the propagation matrix, which can be written as:

$$\mathbf{F} = \begin{bmatrix} \mathbf{0}_{3\times 3} & \mathbf{I}_{3\times 3} \\ \frac{\partial \vec{a}(\vec{r},\vec{v},t)}{\partial \vec{r}(t)} & \frac{\partial \vec{a}(\vec{r},\vec{v},t)}{\partial \vec{v}(t)} \end{bmatrix}_{6\times 6} \tag{3.32}$$

Since the model described by Equation (3.30) is not a function of the velocity, the $\frac{\partial \vec{a}(\vec{r},\vec{v},t)}{\partial \vec{v}(t)}$ term in Equation (3.32) becomes 0. The only remaining term which is non-zero or an identity matrix is $\frac{\partial \vec{a}(\vec{r},\vec{v},t)}{\partial \vec{r}(t)}$. This consists of two parts: the central potential partial and the third body perturbation partial. The derived central potential partial is given in Equation (3.33), while the derived third body perturbation can be divided in the partial with respect to $\vec{r}$ and the partial with respect to $\vec{s}$, which are given in Equations (3.34) and (3.35).

$$\frac{\partial \vec{a}_n}{\partial r_m} = -G(m_1 + m_2)\left(\frac{3r_n r_m}{||\vec{r}||^5} - \frac{\delta_{nm}}{||\vec{r}||^3}\right) \tag{3.33}$$

$$\frac{\partial \vec{a}_n}{\partial r_m} = Gm_3\left(\frac{3(r_m - s_m)(r_n - s_n)}{||\vec{r} - \vec{s}||^5} - \frac{\delta_{nm}}{||\vec{r} - \vec{s}||^3}\right) \tag{3.34}$$

$$\frac{\partial \vec{a}_n}{\partial s_m} = -Gm_3\left(-\frac{\delta_{nm}}{||\vec{r} - \vec{s}||^3} + \frac{3(r_n - s_n)(r_m - s_m)}{||\vec{r} - \vec{s}||^5} + \frac{\delta_{nm}}{||\vec{s}||^3} - \frac{3s_n s_m}{||\vec{s}||^5}\right) \tag{3.35}$$

In these equations $\vec{r}$ is the position of a body whose acceleration a appears on the left-hand side of the differential equation, $\vec{s}$ is the position of a third body, m_1 is the mass of the central body, m_3 the mass of the body corresponding to $\vec{r}$ and δ_{nm} is defined as:

$$\delta_{nm} = \frac{\partial r_n}{\partial r_m} \tag{3.36}$$

The set of equations to be solved for this application, also called the variational equations, can be thus summarised to be

$$\dot{\boldsymbol{\Phi}}(t, t_0) = \begin{bmatrix} \mathbf{0}_{3\times 3} & \mathbf{I}_{3\times 3} \\ \frac{\partial \vec{a}}{\partial \vec{r}} & \mathbf{0}_{3\times 3} \end{bmatrix}_{6\times 6} \cdot \boldsymbol{\Phi}(t, t_0) \tag{3.37}$$

where $\frac{\partial \vec{a}}{\partial \vec{r}}$ is calculated with Equations (3.33), (3.34) and (3.35). Important to note is that so far the STM for only one body has been discussed (and is thus 6×6), but for this study the STM in Equation (3.37) needs to consider two bodies (spacecraft and asteroid) and the STM should thus be 12×12. This 12×12 matrix consists of a 6×6 STM matrix, that has been discussed so far, for each of the two bodies concatenated diagonally. The remaining, off-diagonal, terms depict the interaction of the velocity and position components between the two bodies. The STM thus has the following shape, where the "sc,ast" subscript means the correlations between spacecraft and the asteroid:

$$\boldsymbol{\Phi}(t, t_0) = \begin{bmatrix} \boldsymbol{\Phi}_{sc}^{6\times 6} & \boldsymbol{\Phi}_{sc,ast}^{6\times 6} \\ \boldsymbol{\Phi}_{ast,sc}^{6\times 6} & \boldsymbol{\Phi}_{ast}^{6\times 6} \end{bmatrix} \tag{3.38}$$

Now that the complete model has been set up, the system of equations in Equation (3.37) can be integrated simultaneously to calculate the STM, using the initial conditions $\boldsymbol{\Phi}(t_0, t_0) = I$. The STM is used in many parts of the orbit determination model, especially for propagating the covariance to another epoch. This will be discussed in Subsection 3.2.6, as the purpose of this subsection is only to describes the methodology for setting up the STM and variational equations.

3.2.4. Remaining Essential Setup

Before discussing the covariance analysis itself, there are a few essential steps that need to be covered first. In this section the following will be discussed: naming the close approaches consistently, modelling the TCM uncertainty, defining reset epochs and modelling NGAs and their uncertainty.

It is useful to have a naming convention for the various specific epochs during a mission, in particular the close approach. For this study, the notations used within ESA for the Consolidated Report on Mission Analysis (CReMA) are used. Three elements are needed for this notation: the total amount of flybys in the mission so far, the upcoming flyby body, and the amount of times the upcoming flyby body has been flown by before during the mission. These three elements are then concatenated, where only the first letter of the flyby body is used. For example, in the JUICE tour *14C6* means the upcoming flyby will be the 14th of the tour, the flyby body will be Callisto, and it will be the 6th flyby to Callisto in this tour. It is useful to have this naming convention for flybys, as additional information can be concatenated after the CA name to specify another epoch, such as an event that will occur a few days after the CA: *27G13+3d*. This naming convention will be frequently used from now on.

In the model for the spacecraft trajectory generation, described in Chapter 2, it was assumed that the asteroid orbit was perfectly known. In reality there will be additional TCMs for navigational purposes when nearing the asteroid due to asteroid position uncertainties, orbit determination errors and manoeuvre execution errors. In the present model, this is taken into account by means of introducing a mechanisation error covariance for each expected navigation TCM, which basically takes the effect of the manoeuvre misperformance in the knowledge into account. Usually this mechanisation error covariance is generated using guidance software, but, for simplicity, a fixed covariance at fixed dates before the CA epoch is used for this study. An error value of 30 mm/s has been found to be an adequate recurring value for this purpose, and the TCM epochs have been chosen to occur at exactly 30, 14 and 3 days before the CA [35].

In order to avoid the accumulation of model errors, reset epochs have been defined in the model. When a reset epoch occurs, the spacecraft covariance and correlations between spacecraft and target asteroid in the covariance matrix are reset to their a priori values. This means that after a reset epoch, only the target asteroid covariance is preserved in the covariance matrix. Ideally, the reset epochs occur somewhere a few days to weeks before the upcoming CA [35]. For this study the reset epochs have therefore been set to 30 days before each CA.

As mentioned in Subsection 3.2.3, Non-Gravitational Accelerations (NGAs) are not part of the equations of motion, as they are modelled in a separate way. NGAs have been modelled as impulsive stochastic manoeuvres, which occur at least once every 24 hours. The 1-σ impulsive dV, in km/s, for every NGA is computed as follows:

$$dV_{NGA} = a_{NGA} \cdot \sqrt{dt_{NGA,avrg} \cdot dt_{dV}} \tag{3.39}$$

where a_{NGA} is the 1-σ value for all NGAs in the EME2000 frame in km/s^2, $dt_{NGA,avrg}$ is the NGA averaging time, which is the interval during which the NGA can be assumed to be constant, and dt_{dV} is the time between the current and next output epoch. Similar to the TCMs, the mechanisation error covariance matrix for every NGA will account for the dV_{NGA} misperformance. Throughout this study, a NGA averaging time of 10 days has been used and a NGA of $1 \cdot 10^5$ mm/s^2, which are the same inputs used for JUICE [36].

3.2.5. Covariance Analysis

Now that all the essentials have been discussed, the covariance analysis setup for this thesis can finally be presented. In this subsection it will become clear how all of the previously discussed equations and theory in Subsections 3.2.1 through 3.2.4 work together.

3.2.5.1. Filter Choice

In the covariance analysis two key elements play a role to increase the knowledge of the target: the simulated estimation of the state, using the STM and variational equations discussed in Subsection 3.2.3, and the optical, range and Doppler measurements discussed in Subsections 3.2.1 and 3.2.2. Together, these can be used to precisely estimate the state of the desired object. This is achieved using a so called filter, which is a general term used for estimation procedures in time varying systems. For applications where there exists some uncertainty about the system, the filter can be used to make an accurate guess about the (future) behaviour of the system. The general idea behind a filter is to convert a measurement error to a state error and to retrieve the best possible estimate of the state.

There exist several filtering techniques, also called filter mechanisations. These can be divided into two types: covariance filters and inverse covariance filters. Covariance filters, such as the Kalman filter, propagate the covariance matrix while inverse covariance filters, also called information filters, such as the Square Root Information Filter (SRIF), propagate the inverse of the covariance matrix. Both techniques have advantage and disadvantages. The main advantages of using the covariance filters are that the state variables and covariance matrix can be continuously estimated at no extra computational cost and that the filter appears to be more flexible and easier to modify to perform sensitivity and error analyses. On the other hand, advantages of information filters are that large batches of data are processed efficiently from a computational point of view, and that in theory no information concerning the initial state is needed to start the process, meaning the inverse covariance matrix at the initial epoch may be zero [37] [38] [39] [40]. However, in practice a decent initial guess is still needed, since the linear model will only converge if the initial linearisation point was sufficiently close to the true value. The main advantage of an information filter is that since it deals with the square root of the covariance matrix, it is less prone to numerical errors resulting from badly conditioned matrices, which especially occur in highly non-linear systems like flyby trajectories [41].

The SRIF, like all other least-squares filter algorithms, is based on an iterative approach: starting from given a priori conditions an a priori covariance matrix can be generated, the trajectory is integrated over the entire arc and the differences between observations and modelled measurements, called the residuals, are obtained. Then, using the partial derivatives with respect to the parameters of interest, corrections of the a priori parameters can be calculated from the least-squares solution, which are stored in an updated covariance matrix. This updated covariance matrix is then used as the new a priori input for the propagation of the next arc. The covariances are initially large, but reduce as more measurements are added to the system over the arcs. In order to cope with non-linear problems, a few iterations are required and convergence is typically achieved with a few iterations. On the other hand, the Kalman filter is recursive: the estimated state vector and its covariance matrix at the initial conditions are propagated to the next epoch where measurements are available. At this epoch, an update of the state occurs: the data from observations are merged into the propagated state using a weighting factor, called the Kalman gain, which depends on the accuracy of the measurements and the propagated covariance. This process is continued as long as new observations become available. The key difference is that the Kalman filter requires less computation time and has less computer memory needs while the SRIF has

a better smoothness of the estimated trajectory and is in general more robust where there are some gaps in the data. For this reason, for real-time applications the Kalman filter is more suitable due to the low computation time. For ground-based simulations ahead of time, where computational time is not as important, the preference goes to the SRIF [42]. In the flight dynamics department of ESOC, the SRIF is always used for orbit determination. Therefore, the SRIF will be used for this thesis too and the mathematical model will be described in detail. Note that for this application it is assumed that the state at which the partials are evaluated is already the true state. In other words, the SRIF will not perform iterations per arc, as was explained at the beginning of this paragraph.

3.2.5.2. SRIF Mathematical Model

The equations of the SRIF will now be discussed, starting from the solution and working back to the basics. The solution of the SRIF can be written as:

$$\mathbf{x}_0^{lsq} = \mathbf{x}_0^{ref} + \Delta\mathbf{x}_0^{lsq} \tag{3.40}$$

where $\Delta\mathbf{x}_0^{lsq}$ can be found using Cholesky's algorithm for the following equation:

$$(\mathbf{H}^T\mathbf{H})\Delta\mathbf{x}_0^{lsq} = (\mathbf{H}^T\Delta\mathbf{z}) \tag{3.41}$$

In this equation, $\mathbf{H}$ is the Jacobian matrix containing the partial derivatives of the modelled observations with respect to the state vector at the reference epoch t_0 and $\Delta\mathbf{z}$ is the difference between the actual observations and predictions from the simulation results. In mathematical form these variables can be written as

$$\mathbf{H} = \left.\frac{\partial\mathbf{h}(\mathbf{x}_0)}{\partial\mathbf{x}_0}\right|_{\mathbf{x}_0=\mathbf{x}_0^{ref}} \tag{3.42}$$

$$\Delta\mathbf{z} = \mathbf{z} - \mathbf{h}(\mathbf{x}_0^{ref}) \tag{3.43}$$

The derivation of all the partials, both for the optical measurements and for the range and Doppler measurements, is shown in Appendix B. For the remainder of this section, it is assumed that the partials, and therefore the matrix $\mathbf{H}$, are known. The solution can be improved by iterating the reference state and treating it as an a priori state for each iteration. However, following the assumption that the state at which the partials are derived is already the true state, the solution for this thesis requires no iterations.

The diagonal matrix $\mathbf{S}$ includes both the noise and systematic errors in order to treat the several types of measurements differently. In other words, it is the square root of a covariance matrix containing the measurement errors. It is used to update Equations (3.42) and (3.43):

$$\hat{\mathbf{H}} = \mathbf{SH} \tag{3.44}$$

$$\Delta\hat{\mathbf{z}} = \mathbf{S}\Delta\mathbf{z} \tag{3.45}$$

A distinction should be made between estimation and consider parameters. Estimated parameters are (as the name implies) parameters that will be estimated during the covariance analysis. Consider parameters on the other hand are parameters that are not estimated in the solution and that are not used to improve the solution state, but the effect of these parameters on the state is however considered, thus the correlations are still computed. This way, the systematic errors that these parameters would bring in the system are still considered. For this application, a third type of parameter is introduced, dubbed Implicitly Estimated Parameter (IEP). Implicitly estimated parameters are parameters that are estimated but are not included in the covariance matrix in order to prevent the covariance matrix from becoming too large. They are thus treated the same way as estimation parameters, without including them in the covariance matrix. IEPs have been introduced in the system to model NGAs.

Now that this distinction is made, it should be noted that the matrix $\mathbf{H}$ in Equation (3.44) consists of four main elements: the a priori covariance matrix and the partial derivative matrix of the measurements with respect to the estimation, consider and IEP parameters: $\mathbf{P}$, $\mathbf{H}_E$, $\mathbf{H}_C$ and $\mathbf{H}_{IEP}$, respectively.

In order to overcome numerical problems when finding the direct solution of the least-squares problem, QR factorisation can be used to find the solution of the SRIF, once the $\mathbf{H}$ matrix has been set up and has been updated using Equation (3.44) to yield $\hat{\mathbf{H}}$. This splits the matrix $\hat{\mathbf{H}}$ in an orthonormal matrix $\mathbf{Q}$ and an upper triangular matrix $\mathbf{R}$. The QR factorisation can be visualised as follows:

$$\hat{\mathbf{H}}_{n \times m} = \mathbf{Q}_{n \times n} \begin{bmatrix} \mathbf{R}_{m \times m} \\ \mathbf{0}_{(n-m) \times m} \end{bmatrix} \tag{3.46}$$

An efficient way to perform the QR factorisation is using Householder transformations. The covariance matrix $\mathbf{P}$ can then be easily computed with:

$$\mathbf{P} = (\mathbf{R}^T \mathbf{R})^{-1} = (\mathbf{R}^{-1})(\mathbf{R}^{-1})^T \tag{3.47}$$

Since the covariance matrix can be generated directly from the upper triangular matrix $\mathbf{R}$ without the need of any other variables, $\mathbf{R}$ can be seen as the solution of the SRIF and has been dubbed SRIA (Square Root Information Array) in this study.

3.2.5.3. Covariance Analysis Flow

A lot of equations have been discussed so far in this chapter. In Figure 3.4 a flow diagram to visualise the flow between the several parts of the covariance analysis is shown in order to get a good overview of which equations are used where. A discussion of every step follows after the figure.
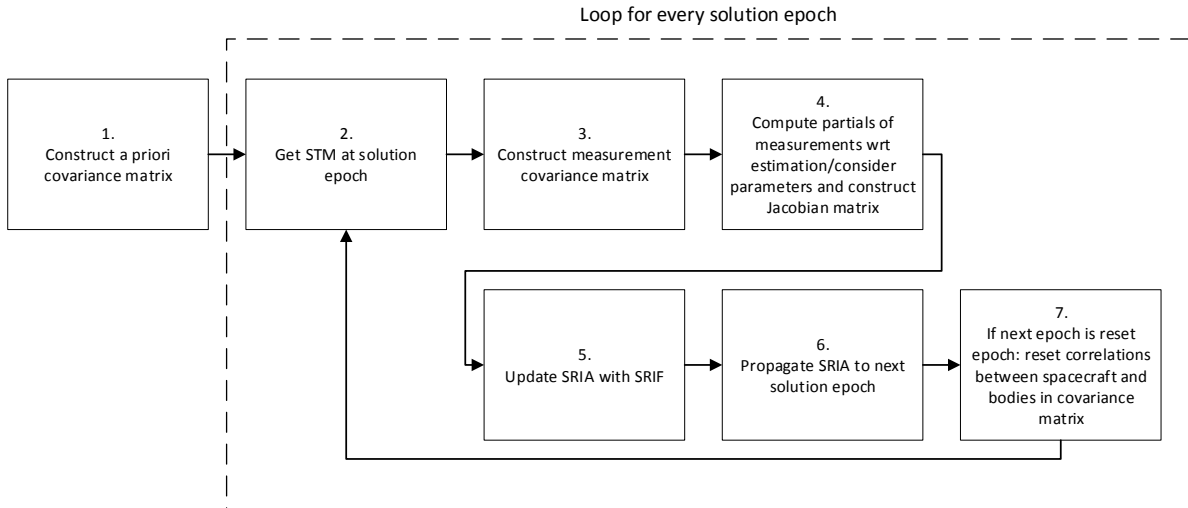
Figure 3.4: Covariance Analysis Flow

1. This step entails in creating $\mathbf{P}_{E,apr}$, $\mathbf{P}_{C,apr}$ and $\mathbf{P}_{IEP,apr}$, which are the a priori matrices for the estimation, consider and implicitly estimated parameters, respectively. They are constructed by simply concatenating the a priori data for that specific parameter type.
2. Here the STM valid for the current epoch is extracted from previously calculated STM matrices.
3. In step 3 the measurement covariance matrix is constructed, which is $\mathbf{S}$ in Equation (3.44). This matrix contains the noise for each measurement. For this thesis no optical noise measurement model is used, but rather a constant value is used, as will be clear from Subsection 3.2.7.
4. All the calculations described in Appendix B take place in this step, in order to get the Jacobian matrices $\mathbf{H}_E$, $\mathbf{H}_C$ and $\mathbf{H}_{IEP}$, recall Equation (3.42).
5. Step 5 is then the core step of the covariance analysis, which is where all the measurements are combined with the current knowledge in the filter to produce an updated knowledge. This is basically implementing Equations (3.44) and (3.46), in order to find the SRIA, $\mathbf{R}$ in Equation (3.46).
6. Here the SRIA is propagated to the next solution epoch, in order to prepare it for the next covariance analysis loop. Propagating the SRIA will be discussed in Subsection 3.2.6.
7. Finally, it is checked whether the upcoming solution epoch is a reset epoch. If this is the case, only the asteroid covariance is kept, meaning the spacecraft covariance is reset to the a priori and the correlations between spacecraft and asteroid are reset to zero, as discussed in Subsection 3.2.4.

3.2.6. Post-Processing of Results

The covariance analysis has now been fully explained and the result of the analysis is clear: it will consist of the SRIA, $\mathbf{R}$ in Equation (3.46), at every solution epoch. However, there are some steps to be taken in order to extract the useful data for plotting purposes.

In order to propagate, also often referred to as mapping in this thesis, the covariance matrix $\mathbf{P}$ and SRIA $\mathbf{R}$ from epoch t_j to t_k the following equations are used:

$$\mathbf{P}_k = \mathbf{\Phi}(t_k, t_j) \cdot \mathbf{P}_j \cdot \mathbf{\Phi}^T(t_k, t_j) \tag{3.48}$$

$$\mathbf{R}_k = \mathbf{R}_j \cdot \mathbf{\Phi}^{-1}(t_k, t_j) \tag{3.49}$$

Another post-processing result is converting the results to the TNW frame, recall Table 3.1. The results so far are in the heliocentric EME2000 frame, but when plotting the results these will not be as interpretable because of the x, y and z coordinates oscillating with the position in the orbit. Much more useful would be to have the results in a Local Orbital Frame (LOF). The elements T (along-track), N (cross-track) and W (radial) of the chosen LOF do not oscillate with the orbit. In order to get the covariance matrix results in TNW frame Equations (3.14) through (3.17) are used.

An important step for this thesis is to map the asteroid knowledge evolution in the B-plane of the Earth at the expected asteroid close approach (or impact) epoch with Earth. In other words, this entails in converting the asteroid knowledge evolution in the B_T and B_R parameters in the Earth B-plane, from which it can be directly seen how the asteroid impact uncertainty changes for such a flyby mission. This will be one of the most important results of the thesis. Note that this should absolutely not be confused with the spacecraft close approaches with the asteroid (which is when optical measurements are taken). From now on the expected Earth impact or close approach epoch will be referred to as the threat epoch, to avoid confusion. To convert the data, a couple of steps are needed.

First of all, the asteroid state vector at the Earth flyby pericentre is needed. This entails in simply reading the state from the asteroid ephemeris at exactly the expected threat epoch. The SRIA is then propagated to the threat epoch, using Equation (3.49). The mapped SRIA is then converted to the covariance matrix, using Equation (3.47). The mapped covariance is currently in heliocentric EME2000 coordinates, and needs to be converted to the TRS (B-plane) frame, recall Table 3.1. A rotation matrix is needed to accomplish this, recall Equation (3.1). To calculate the rotation matrix from the inertial frame to the TRS frame, Equations (3.9) through (3.13) are used. However, for these equations the $\vec{V}_\infty$ is needed, more specific: the $\vec{V}_{\infty,in}$. Differently than the asteroid flybys, the $\vec{V}_{\infty,in}$ and $\vec{V}_{\infty,out}$ for the asteroid at the threat epoch will be two different vectors, since the Earth gravitational parameter cannot assumed to be zero. In order to calculate these vectors, first the scalar magnitude V_∞ is needed:

$$V_\infty = \sqrt{V_p^2 - \frac{2\mu}{r_p}} \tag{3.50}$$

where V_p is the scalar magnitudes of the velocity at pericentre and r_p is the position at pericentre, which is equal to the flyby body radius plus the flyby altitude. Furthermore, μ is the gravitational parameter of the flyby body, in this case Earth. Then, the magnitude of the impact parameter, which was introduced in Subsection 2.3.2, is calculated with:

$$B = \frac{r_p V_p}{V_\infty} \tag{3.51}$$

When combining Equation (3.51) with the square of Equation (3.50), the impact parameter, also called the B-vector, magnitude can be expressed as:

$$B = \sqrt{r_p^2 + \frac{2\mu r_p}{V_\infty^2}} \tag{3.52}$$

This is needed to calculate the eccentricity e, which will then be used to calculate the true anomaly at infinity τ_∞:

$$e = \sqrt{1 + \frac{B^2 \cdot V_\infty^4}{\mu^2}} \tag{3.53}$$

$$\tau_\infty = \cos^{-1}\left(\frac{-1}{e}\right) \tag{3.54}$$

Two unit vectors are then defined as:

$$\hat{e}_r = \frac{\vec{r}_p}{||\vec{r}_p||} \tag{3.55}$$

$$\hat{e}_v = \frac{\vec{v}_p}{||\vec{v}_p||} \tag{3.56}$$

The $\vec{V}_{\infty,in}$ can now be calculated, which concludes the equations needed to calculate $\mathbf{P}_{TRS}$. This is done using:

$$\vec{V}_{\infty,in} = -V_\infty \cdot \cos(\tau_\infty) \cdot \hat{e}_r - \sin(\tau_\infty) \cdot \hat{e}_v \tag{3.57}$$

$$\vec{V}_{\infty,out} = V_\infty \cdot \cos(\tau_\infty) \cdot \hat{e}_r + \sin(\tau_\infty) \cdot \hat{e}_v \tag{3.58}$$

In addition to the knowledge evolution, the covariance error ellipse (also known as covariance ellipse or simply error ellipse) is also analysed in this thesis. Starting from the previously computed $\mathbf{P}_{TRS}$ matrix, the B_T and B_R variances and covariances of the asteroid are extracted. The eigenvalue and eigenvectors of this position covariance matrix will then be calculated, after which the angle between the principal axes and the original axes system can be calculated. This is done using the following equation:

$$\phi = \tan_2^{-1}\left(\frac{LE_y}{LE_x}\right) \tag{3.59}$$

Where LE_x and LE_y are the x and y components of the eigenvector corresponding to the largest eigenvalue (LE), respectively. The semi-major axes a_i and minor axes b_i are then calculated with

$$a_i = \sqrt{l_i^2 \lambda(max)} \tag{3.60}$$

$$b_i = \sqrt{l_i^2 \lambda(min)} \tag{3.61}$$

With i ranging from 1 to 3. The ellipsoids for $l_i = 1$, 2 and 3 are called the 1-σ, 2-σ and 3-σ error ellipsoids, respectively. Using a_i, b_i and ϕ the error ellipsoid can be plotted [34]. However, the origin for positioning the error ellipses, thus the nominal position of the asteroid in the Earth B-plane at the threat epoch, is needed to correctly place the error ellipses in the plot. For this, the previously found asteroid state at flyby pericentre (which can be read directly from the asteroid ephemeris) is used to calculate the B-vector, recall Figure 2.3. The asymptote vector $\hat{S}$, a unit vector in the direction of $\vec{V}_{\infty,in}$, was already previously calculated in Section 3.1: recall Equations (3.9) and (3.10). In these equations, $\vec{V}_{\infty,in}$ (previously calculated with Equation (3.57)) should be used for $\vec{V}_\infty$ as well as the same pole unit vector as Equation (3.12). The unit vector of the impact parameter ($\hat{B}$) and previously calculated asymptote unit vector ($\hat{S}$) can form a coordinate system, where the third element, denoted by $\hat{h}$ in this thesis, to complete this right-handed coordinate system will be normal to the orbital plane. The unit vector $\hat{h}$ is not included in Figure 2.3, although an idea of its orientation can be formed when considering it is normal to the orbital plane included in the figure. This unit vector can thus be calculated with

$$\hat{h} = \frac{\vec{V}_{\infty,in} \times \vec{V}_{\infty,out}}{||\vec{V}_{\infty,in} \times \vec{V}_{\infty,out}||} \tag{3.62}$$

where $\vec{V}_{\infty,in}$ and $\vec{V}_{\infty,out}$ are calculated with Equations (3.57) and (3.58), respectively. The B-unit vector $\hat{B}$ can now be defined by combining Equation (3.52) with the following equations of the B-vector:

$$\hat{B} = \frac{\vec{B}}{||\vec{B}||} = \hat{S} \times \hat{h} \qquad (3.63)$$

from which B-vector $\vec{B}$ can be calculated as well. Lastly, $\vec{B}$ can be combined with $\hat{T}$ and $\hat{R}$, which were calculated with Equations (3.10) and (3.11), to yield the B_T and B_R, as was shown in Equations (2.12) and (2.13). These B_T and B_R coordinates will be the origin of the error ellipses.

One last thing needed for the covariance ellipse plots is the B-vector magnitude radius. When the covariance ellipse overlaps with the Earth radius, there is a probability of a direct impact of the asteroid with Earth. However, there could be a possibility of an Earth impact besides a direct impact due to the Earth gravitational attraction: the asteroid seems to flyby the Earth at first but gets caught by the gravitational pull and impacts the Earth after a deflection from its original trajectory. To approximate when this could be the case, the B-vector magnitude radius is calculated. When the error ellipse overlaps with this radius, there could be a potential non-direct impact. This radius is calculated using Equation (3.52), with the Earth radius and expected asteroid $V_{\infty,in}$ for r_p and V_∞, respectively.

3.2.7. Model Inputs

Now that the complete mathematical model has been explained, all the inputs of the model can be discussed. The inputs values used for all cases in this research, unless stated otherwise, are summarised in Table 3.2, where bias and noise values are 1-σ and R stands for Range, D for Doppler and GS for Ground Station. Extra attention should be paid to the units in Table 3.2, which differ from the usual km and km/s.

Table 3.2: GALICOV Input Values

Optical Measurements		Range/Doppler Measurements	
Noise [μrad]	40 ($\sim 0.5\,px$)	Minimum elevation [deg]	10
Bias [μrad]	40 ($\sim 0.5\,px$)	GS [-]	Malarg
Camera FoV [deg]	4×4	R noise [m]	10
CCD Pixels [-]	1024×1024	R bias [m]	20
Opnav Constraints		R sampling rate [days]	1/24
Min Sun exclusion angle [deg]	30	D noise [m/s[	$8 \cdot 10^{-5}$
Max phase angle [deg]	150	D bias [m/s]	0
Minimum Visibility [mag]	8.5	D sampling rate	1/24
		GS position bias [m]	0.3

As stated in Table 3.2, the navigation camera, which is also used for optical measurements, is assumed to have a 4×4 deg Field of View (FoV) with a Charge-Couple Device (CCD) of 1024×1024 pixels. This is based on recurring values of reference missions summarised in Appendix D. The noise and bias of the optical measurements are roughly 0.5 pixels (1 pixel equals 4/1024). All parameters for range and Doppler measurements are based on recurring values for other interplanetary missions (especially JUICE) [32]. With the current sampling rate there will be one radiometric measurement every hour. While the values for the Optical Navigation (opnav) constraints were discussed in Subsection 3.2.1. The GS position bias value is used for each of the three space directions.

As was explained in detail Subsubsection 3.2.5.2, a covariance analysis consists of a set of to be estimated parameters and to be considered parameters. In that subsubsection Implicitly Estimated Parameters (IEPs) were also introduced. The estimated and considered parameters setup that will be used throughout this research, unless stated otherwise, is summarised in Table 3.3

The a priori covariance for the spacecraft is kept the same as the JUICE case, as this is based on typical values for interplanetary travel, and consists of a 1-σ value of 15 km for the position and 0.1 m/s^2 for the velocity, all in the heliocentric EME2000 frame.

The a priori covariances for the asteroids on the other hand are retrieved from HORIZONS. Using the HORIZONS web-interface[4], a diagonal 1-σ a priori covariance matrix can be retrieved. The use of RST

---

[4]https://ssd.jpl.nasa.gov/horizons.cgi, accessed 05-10-2018

Table 3.3: Estimation and Consider Parameters Setup

Estimated	Considered	Implicitly Estimated
State of target bodies	Range bias	NGAs
State of spacecraft	GS position bias	
Optical measurement bias		
TCMs		

a priori data (which is called RTN - radial, transverse, normal - in HORIZONS) is preferred over data in the inertial EME2000 frame. The reason for this is that in the RST frame the correlations are expected to be smaller than in the inertial frame and also less time-dependent. The following RST a priori data has been used for the three asteroids:

Table 3.4: Apophis, UE34 and WN5 a priori RST Data [MJD2000, km and km/s]

Asteroid	Epoch	r_R	r_S	r_T	v_R	v_S	v_T
Apophis	7945	507.7665	14007.70056	7.2853	7.6514e-10	2.2588e-13	3.5258e-14
UE34	7362	1.5228e6	1.5119e8	4.6250e4	4.6673e-6	2.7935e-10	3.3299e-10
WN5	8351	39.6740	1599.0814	1226.0724	6.2033e-12	2.2434e-13	6.8004e-13

3.3. Verification and Validation

Now that the complete orbit determination mathematical model has been discussed, it is extremely important to verify and validate the correctness of the results. This verification and validation is done in three steps, consistent with the strategy used for expanding GALICOV's capabilities. These phases are:

1. Expand capabilities while keeping JUICE inputs
2. Keep functionality while transitioning to adapted JUICE inputs similar to an asteroid case
3. Keep functionality while transitioning to asteroid inputs

Each of these phases will be described in detail in the following three subsections. Note that the initial version of GALICOV, before making any changes, has undergone many (undocumented) verification and validation tests by ESOC's mission analysis section during its development stages and it has since then been used for official ESA documents. Results of the initial version of the tool can thus be assumed to be fully correct.

3.3.1. Phase 1: Expanding Capabilities

During the first phase, functionality of GALICOV was expanded by making the tool applicable for a wide range of applications rather than only being able to produce results for the JUICE mission. Very important during this phase was to make sure the tool would keep its JUICE functionality. Several features, such as plotting the error ellipses discussed in Subsection 3.2.6, were adding during this phase as well. The used strategy to verify these changes will be explained in detail.

The JUICE CReMA 3.2 tour has a total of 29 flybys to the four Galilean icy moons: none to Io, 2 to Europa, 15 to Ganymede and 12 to Callisto. A shortened version of this tour has been set up for this phase to reduce the covariance analysis computation time greatly. This altered tour only includes the first two flybys, which are both at Ganymede: *1G1* and *2G2* (recall Subsection 3.2.4 for the notation). All the other inputs, as discussed in Subsection 3.2.7, are unaltered.

In order to be absolutely certain the results would be unaffected, it has been decided to use regression tests after every change to verify the tool functionality. After the changes, but before being regression tested, the version of GALICOV is called experimental. After a successful regression test, the tool is referred to as stable. During a GALICOV run, ASCII data files are created containing parts of the covariance results. There are four instances where this happens (the star indicates parts which are not applicable for this thesis but have been tested nonetheless to keep JUICE functionality):

1. After covariance analysis
2. After B-plane propagation
3. *After flyby reconstruction
4. *After flyby pointing reconstruction

Before starting any alteration to the tool, GALICOV has been run with the altered CReMA 3.2 tour and the data files have been saved. These are referred to as the nominal ASCII files. A tool called Automated Regression Test (ART) has been set up, which has been used after every change to perform the regression test. ART performs the following tasks:

1. Run experimental GALICOV with the same input file (altered CReMA 3.2 tour)
2. Compare ASCII files of experimental run with nominal ASCII files. No discrepancies means a successful regression test
3. In case of any discrepancies: highlight the discrepancies in the ASCII files

For this phase the tool should output the exact same results after any change since the changes are purely to expand the capabilities of GALICOV without altering any results, meaning the experimental ASCII files should be identical to the nominal files. This process of making changes and running ART is repeated until the GALICOV expansion is complete, meaning the tool is fully verified up to this point and is ready for an asteroid case.

3.3.2. Phase 2: Transition to Adapted JUICE Inputs

After all the functionality has been added and the tool is successfully regression tested, the next phase starts. The version at the beginning of this phase works perfectly with the JUICE inputs, however it is expected that when migrating to an asteroid case some aspects will no longer function due to bugs. Therefore, the migration to the asteroid case is done gradually. During this phase the JUICE inputs are changed gradually to eventually simulate an asteroid flyby case as much as possible. This is done by gradually deleting the bodies to be estimated. Until this point five bodies are estimated: the spacecraft and the four icy moons Io, Europa, Ganymede and Callisto, which results in a 30×30 covariance matrix since there are 6 variables for each body's state. The asteroid case will have two estimated bodies: the spacecraft and the asteroid, thus a 12×12 covariance matrix.

In order to simulate the asteroid case as much as possible with JUICE inputs, estimated bodies are gradually removed from the system until only Ganymede is left. With the altered tour two flybys at Ganymede take place and only Ganymede and the spacecraft is estimated, which greatly resembles the resonant asteroid flyby case of this thesis. Since the estimated bodies are changed, the correlations between them change as well, meaning the covariance data will be different than the nominal data of phase 1. ART can thus no longer be used during this phase, as significant discrepancies are expected. The strategy is thus to gradually remove bodies from the system and closely look at the data and figures for big changes, especially for the spacecraft and Ganymede since these are the most relevant bodies during this phase. For this phase, successfully verification entails in yielding results that are in the expected order of magnitude and show a behaviour similar to the original JUICE results.

First of all Io is removed from the estimated bodies. This is expected to have very little changes on the spacecraft and Ganymede results, since no flybys and no measurements take place at Io, meaning its state is improved due to the correlations it has with the other bodies. Afterwards, Callisto and Europa are removed from the estimated bodies. The knowledge of a body changes significantly during optical measurements at that specific body, compared to changes due to correlations with other bodies. Since in this shortened tour there are also no flybys of Callisto and Europa, the results are not expected to change much for the spacecraft and Ganymede knowledge. Just like the case of Io, there are however correlations, so small changes are still expected. The results of this verification part can be seen in Appendix C.1, in Figures C.1 through C.3. As can be seen, the figures are near identical, which means this phase can be considered verified.

3.3.3. Phase 3: Transition to Asteroid Case

Up to now the extended capabilities of GALICOV have been verified to be correct, but this has always been tested in the JUICE environment. When fully transitioning to a completely new environment, such as the asteroid case, the results can no longer be expected to be correct, as was assumed before, since the tool was initially never intended to be used for any other case than JUICE. Therefore, either analytical calculations to verify the data or numerical validation of the data using another software needs to be done. For the former option many simplifications need to be made in order to yield an analytical solution, and has therefore not the preference. Luckily, in ESOC's mission analysis section another tool is available to perform a numerical covariance analysis: GMV's Interplanetary Navigation Tool (INTNAV). INTNAV has been used to verify and validate all aspects of GALICOV. This will be explained in detail in this subsection.

The reason why INTNAV has not been used for the research of this thesis rather than extending GALICOV

to make it applicable for the asteroid case, is that GALICOV is specifically made for a covariance analysis of a flyby mission with optical measurements and offers the user a large variety of flexible inputs due to being developed in-house and changes can be constantly made to suit the user's needs, while INTNAV is a much broader tool where the user has less flexibility on the inputs since it is developed by GMV and not in-house. Furthermore, for this thesis specifically, expanding GALICOV capabilities meant all the equations and theory behind it had to be properly understood and provided a huge increase in astrodynamics knowledge for the author, rather than just setting some inputs in a tool and letting it run without properly understanding the mathematical model behind it, as would have been the case for INTNAV.

First of all, a completely new inputs are needed for the asteroid case. The biggest changes with respect to the JUICE case are: a priori covariance matrix of Apophis instead of the four icy moons, custom spacecraft trajectory spice kernel instead of the JUICE CReMa 3.2 tour and changing the central body from Jupiter to the Sun. A very simple script in GMAT has been set up to generate a spacecraft trajectory for a single flyby to Apophis, with a ballistic trajectory from Earth. Then, the exact same mission profile was set up in INTNAV, using exactly the same input values as in GALICOV such as the a priori covariances, bias and noise values. Several validation cases have been set up to test the various parts of GALICOV, starting from the basics and working up towards the complete asteroid mission, which can be seen in Table 3.5.

Table 3.5: Phase 3 Validation Cases with INTNAV

Case	Measurement Types	Estimated Parameters	Consider Parameters
1	Doppler	SC	-
2	Doppler and Range	SC	Range Bias
3	Doppler and Range	SC	Range and GS Bias
4	Doppler, Range and Optical	SC	Range, GS and Optical Bias
5	Doppler, Range and Optical	SC and Asteroid	Range, GS and Optical Bias
6	Doppler, Range and Optical	SC, Asteroid and NGAs	Range, GS and Optical Bias

The interesting part starts in case 5, since here the asteroid is being estimated as well. This means correlations between spacecraft and asteroid are taken into account as well. The spacecraft knowledge results for this case can be seen in Figure 3.5 and the asteroid knowledge results can be seen in Figure 3.6. The plotted covariance is the consider covariance.

(a) GALICOV   (b) INTNAV
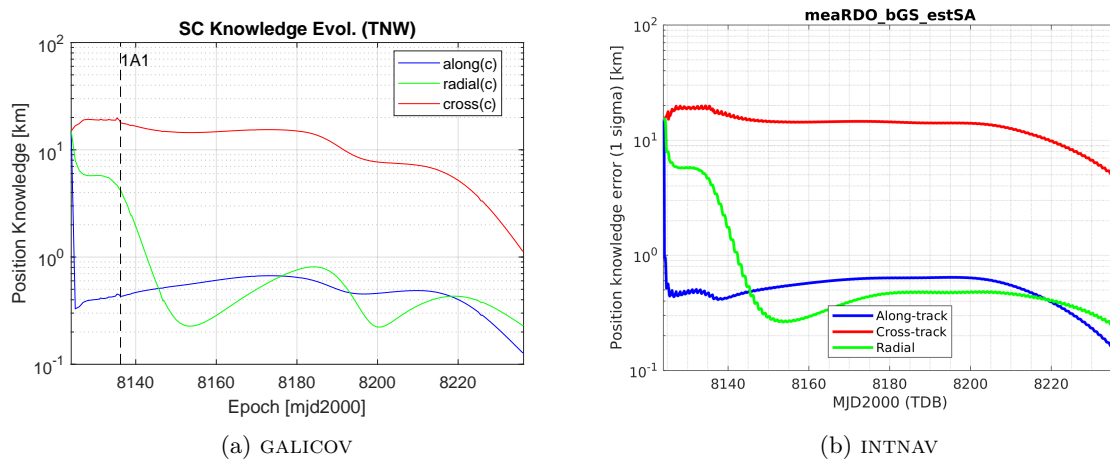
Figure 3.5: Spacecraft Position Knowledge - Case 5

(a) GALICOV

(b) INTNAV
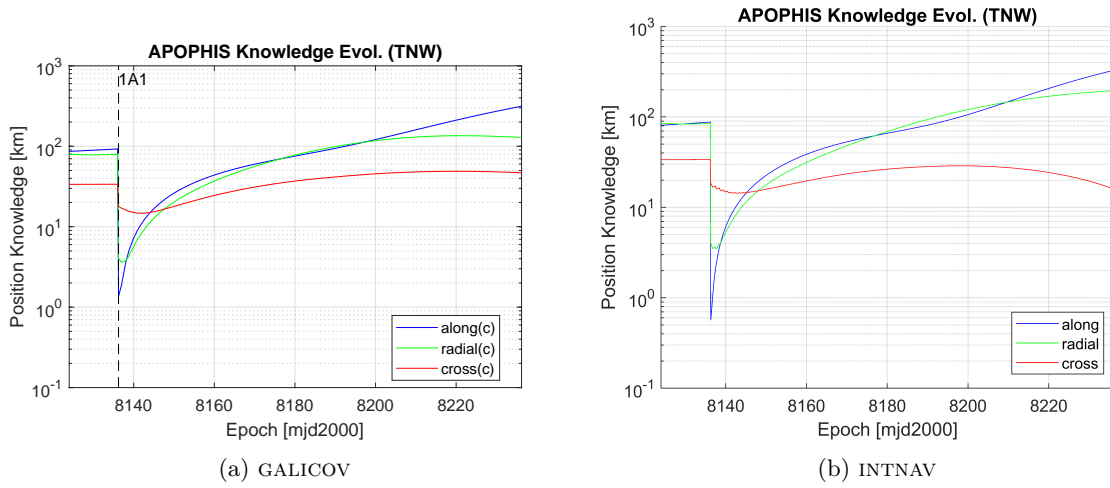
Figure 3.6: Asteroid Position Knowledge - Case 5

As can be seen from Figure 3.5, the along-track and cross-track components are very similar and behave in the same way for both tools. The order of magnitude is exact as well. The radial component however is slightly different, but shows a similar behaviour without any excessive unexpected peaks and furthermore almost converges to the same order of magnitude. The spacecraft knowledge for this case can thus be validated.

The asteroid knowledge is the most important aspect of this validation, and is what all the previous validation cases were working towards. As can be seen in Figure 3.6, the results of both tools match perfectly. Only at the very end the cross-track component differs slightly. The order of magnitude at all epochs are very similar, which means the asteroid knowledge with the functionalities of case 5 can be considered fully validated.

Finally, the results of both tools for case 6 can be seen in Figure 3.7 for the spacecraft and in Figure 3.8 for the asteroid.

(a) GALICOV

(b) INTNAV
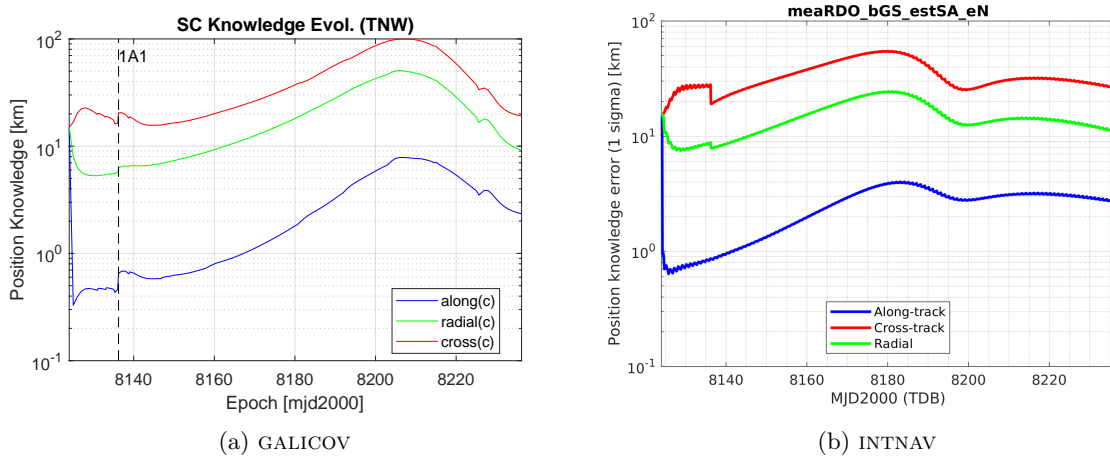
Figure 3.7: Spacecraft Position Knowledge - Case 6

(a) GALICOV
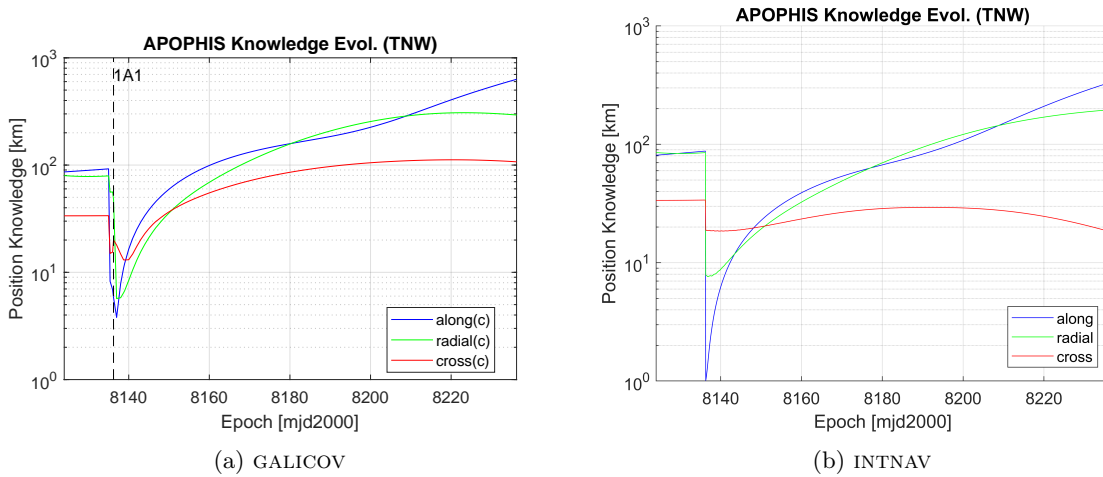
(b) INTNAV

Figure 3.8: Asteroid Position Knowledge - Case 6

As can be seen, the results of these tools differ somewhat. The NGAs are modelled in a different way in both tools, which means that discrepancies can be expected: in INTNAV the NGAs are modelled as exponentially correlated random variables while in the present model as impulsive stochastic manoeuvres. The main differences between the two models lies in the fact that in INTNAV the NGAs are correlated while in GALICOV the accelerations are completely independent form each other, which is less realistic. Since the evolution knowledge is plotted, a small but constant discrepancy over all epochs can eventually lead to very different results, which is what happens for case 6. As can be seen in Figure 3.8, the trend of the plot and the order of magnitude matches for both tools. Therefore, even though the results differ, the method discussed in Subsection 3.2.4 for the implementation of NGAs can be assumed to be a valid one. This concludes the verification and validation of GALICOV, and it can be concluded the results of GALICOV are valid.

The results of the spacecraft knowledge of cases 1 through 4 can be seen in Appendix C.2, in Figures C.4 through C.7.

3.4. Orbit Determination Results

Now that the model has been fully discussed and GALICOV has been verified and validated, it is time to perform the actual research by running the study cases and presenting the results. The study cases can be divided in the following categories:

- **Case 1**: Effect of B-plane flyby geometry
    - Target 4 different points in the asteroid B-plane at CA
- **Case 2**: Effect of input parameters
    - Optical measurements: time interval between measurements, amount of measurements, distance to target at measurement and noise/bias values
    - Range/Doppler measurements: time interval between measurements
    - A priori covariance
- **Case 3**: Effect of asteroid target
    - With similar mission profile
    - With different mission profile

For study cases 1 and 2 the target asteroid is Apophis, while for study case 3 the targets are asteroids WN5 and UE34. Only the spacecraft covariance, asteroid covariance and the correlations between these two have been analysed in these cases. The correlations between all the other parameters have not been investigated in this study. Each of these study cases will now be discussed in detail.

3.4.1. Case 1: Effect of B-Plane Flyby Geometry

The goal is to understand how the asteroid state knowledge results change when approaching the asteroid from a different point and taking optical measurements at different locations. Therefore four different spacecraft trajectories have been set up targeting four different points in the B-plane at the close approach with Apophis, as discussed in detail in Chapter 2. As was discussed in that chapter, the four

generated trajectories are almost identical both before and after the flyby. Therefore, both the optical and radiometric measurement schedule are almost identical for the four cases, and to avoid duplicate figures, only the results for the trajectory targeting B_T 0 km and B_R 600 km are showed (arbitrarily chosen from the four trajectories). Note however that all the optical and radiometric measurement plots are valid for all four trajectories.

The value of the three constrains to be taken into account for the optical navigation schedule over the whole mission duration can be seen in Figure 3.9.
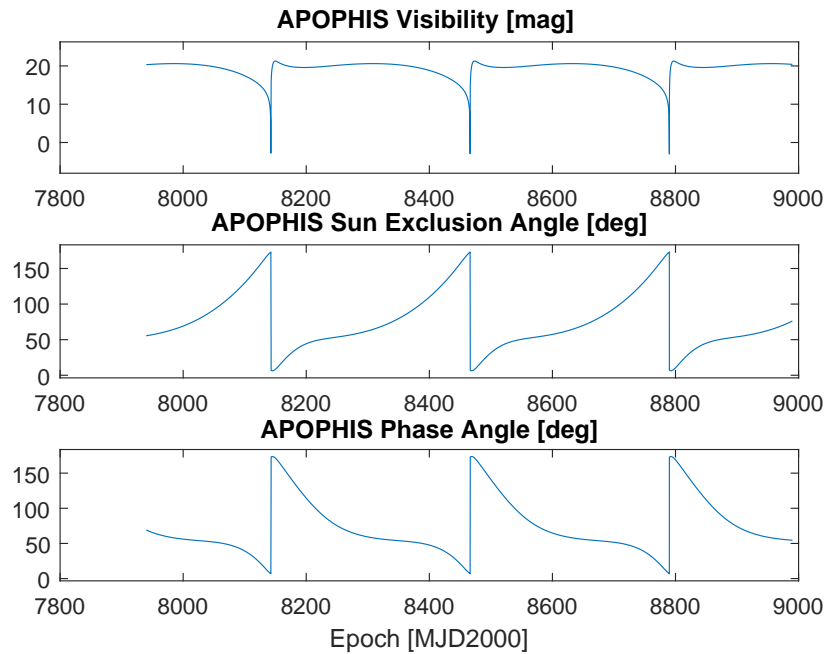
Figure 3.9: Optical Measurement Constraints for Case 1

Considering the constraint value for these three parameters, discussed in Subsections 3.2.1 and 3.2.7 and tabulated in Table 3.2, the intervals when optical measurements are possible can be seen in Figure 3.10.
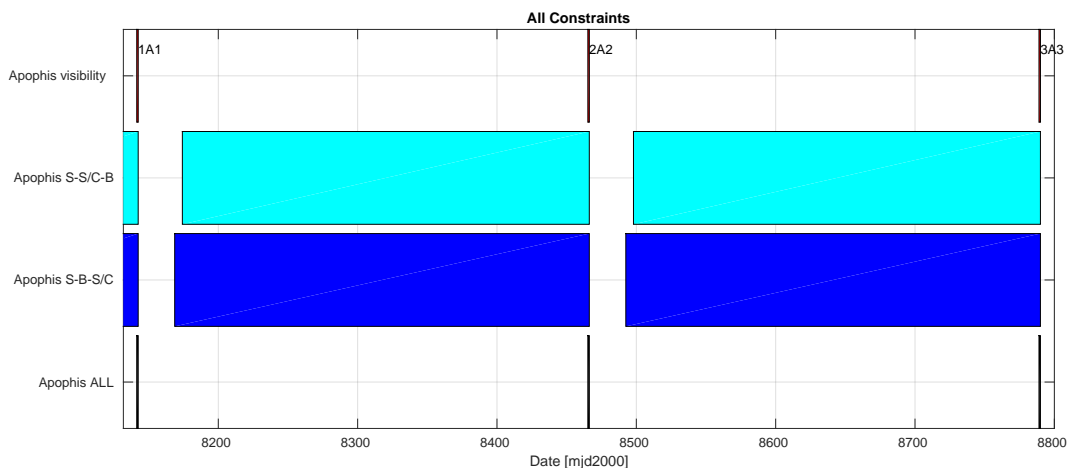
Figure 3.10: Optical Measurement Intervals for Case 1

The positions of the spacecraft and asteroid at the optical measurement epochs can be seen in Figure 3.11, while the distance between the spacecraft and asteroid at the measurement epochs can be seen in Figure 3.12. Note that Figure 3.11 is in fact a close up of Figure 2.9 at the flyby itself, with an addition

of the positions where optical measurements are taken. Recall Equation (3.25) for the relation of the target's distance and the kilometric weight of the measurement.
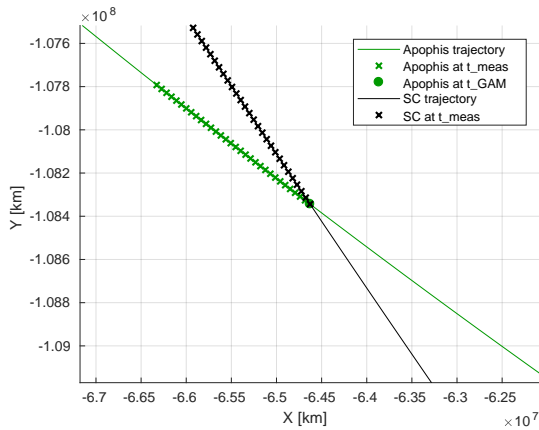
Figure 3.11: Optical Measurement Geometry for Case 1
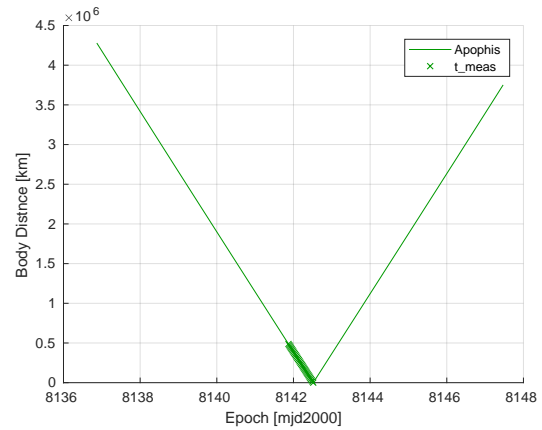
Figure 3.12: Optical Measurement Distance for Case 1

As can be seen from these two figures, all the optical measurements occur before the closest approach. The reason for this can be seen in Figure 3.9: right after the closest approach, both the phase angle and the Sun exclusion angle rapidly change to a point where the constraints are not met anymore. When the angles constraints are again met, the visibility constraint is no longer met. Although only the B_T -600 km and B_R 0 km case is shown, the exact same occurs for the other three trajectories of this case. The radiometric schedule can be seen in Figure 3.13.
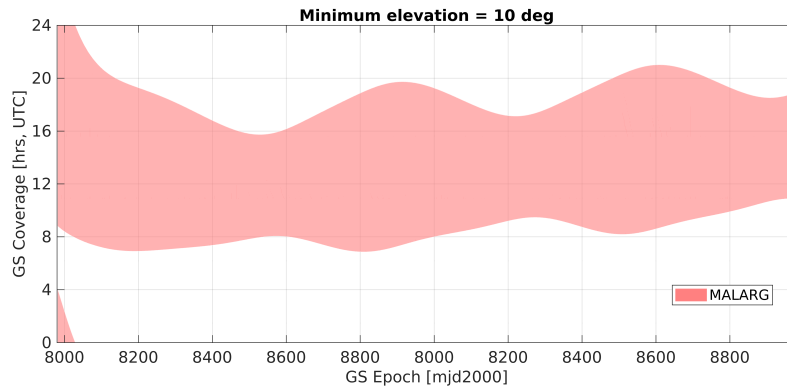
Figure 3.13: Radiometric Measurement Schedule for Case 1

In this figure the exact times (in UTC) at which radiometric measurements are possible from the GS Malarg, which means the spacecraft is visible from Earth (and including light-time effects, as discussed in Subsection 3.2.2). As can be seen, measurements are possible every day for about 8 hours. Since the radiometric measurement interval is 30 minutes, as discussed in Subsection 3.2.7, there will be about 16 radiometric measurements per day over the span of the entire mission duration. ESA's ESTRACK (European Space Tracking) network has two other deep space ground stations usable for deep space missions such as this one, New Norcia and Cerbreros, which have not been analysed in this research.

Moving on to the covariance analysis results for this case. First, all the results will be shown while the discussion will follow later. Since all results are fairly similar, one case is taken as the baseline case while for the other cases the differences are plotted with respect to the baseline case in order to better visualise the differences of the knowledge evolution. The case for $B_T = 0$ and $B_R = 600$ km has been chosen as the baseline, and can be seen in Figure 3.14, where the letters (c) and (f) in the legend correspond to consider covariance and formal covariance, respectively. The differences, for the consider covariance, can be seen in Figure 3.15.
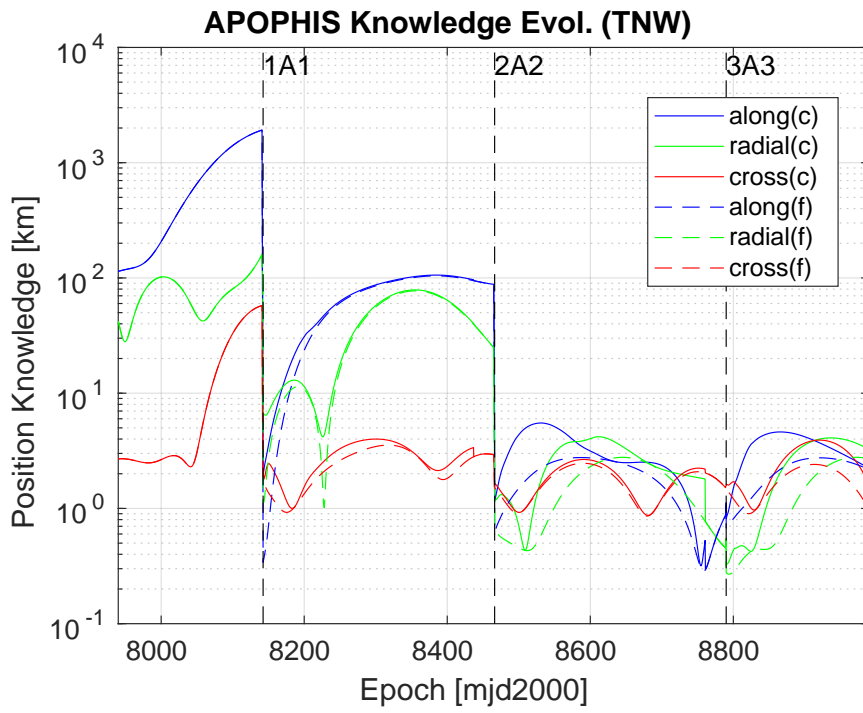
Figure 3.14: Apophis Position Knowledge Evolution - B_T 0 km and B_R 600 km Trajectory
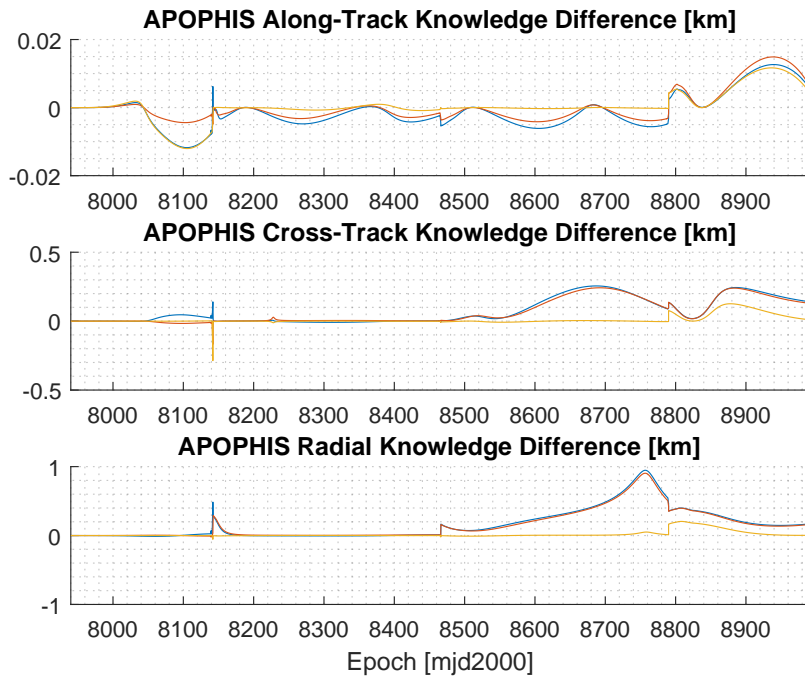
Figure 3.15: Apophis Position Knowledge Evolution - Differences wrt Figure 3.14
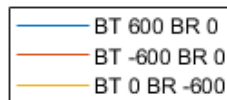
Then, the knowledge evolution of Apophis in the Earth B-plane at ECA (Earth Close Approach) is shown. Again, the results for the baseline trajectory of $B_T = 0$ and $B_R = 600$ km are plotted in Figure 3.16, while for the other three trajectories the differences are shown in Figure 3.17.
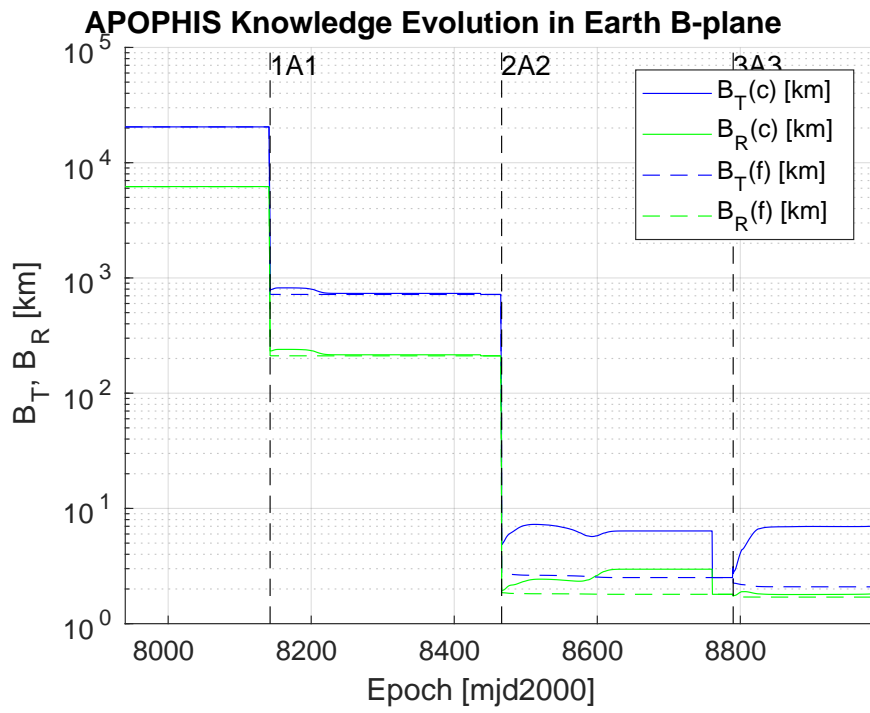
Figure 3.16: Apophis Position Knowledge Evolution in Earth B-plane at ECA - B_T 0 km and B_R 600 km Trajectory
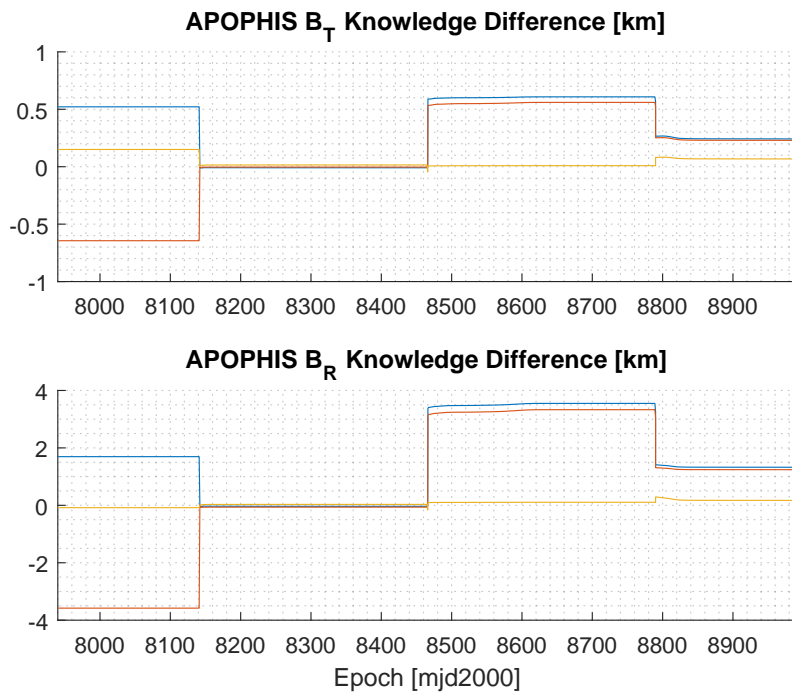
Figure 3.17: Apophis Position Knowledge Evolution in Earth B-plane at ECA - Differences wrt Figure 3.16

Note that no noise for the asteroid is present in the mapping of the SRIA, which means the knowledge is not deteriorating between last flyby and ECA while there are no measurements, while in reality the

knowledge should deteriorate due to the non-gravitational accelerations that act on the asteroid such as the Yarkovsky effect, which affects primarily small bodies such as asteroids. This cannot be solved with NGAs since the NGAs in GALICOV only apply to the spacecraft knowledge. In order to accurately model this effect, NGAs need to be added to the asteroid as well, which is not done in this thesis. Finally, the 1, 2 and 3-σ a priori and a posteriori covariance error ellipses in the Earth B-plane at ECA are shown in Figure 3.18. For this plot it has been decided to only show the result for the baseline case of $B_T = 0$ and $B_R = 600$ km, since all four look identical, which was expected considering Figure 3.17. Note that for this figures the consider covariance has been plotted. Also note that in this figure the a posteriori 3-σ ellipse has been made thick, since it was otherwise too little to be seen in the graph. Crosses are also added at the edges of the ellipses, as it would otherwise be hard to see the edges of the 2 and 3-σ ellipses. Finally, in this figure the current estimate of the nominal point of the asteroid in the Earth B-plane is assumed to be correct, since this has not been analysed in this thesis.
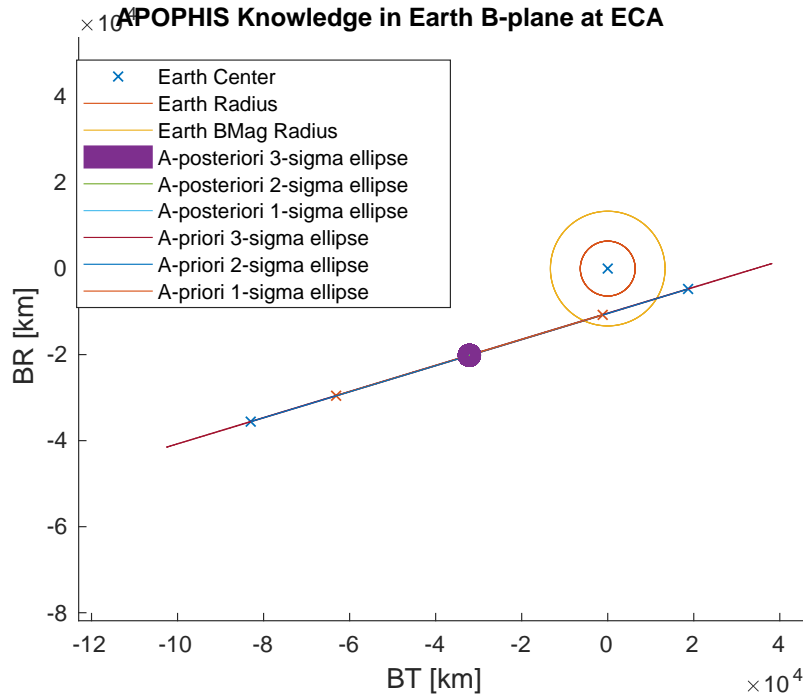
Figure 3.18: Apophis Position Error Ellipses in Earth B-plane at ECA - B_T 0 km and B_R 600 km Trajectory

The result of zooming in on this ellipse and additionally plotting the error ellipses of the knowledge after the 1st, 2nd and 3rd flybys can be seen in Figure 3.19, and in Figure 3.20 the result can be seen when zooming again on the final a posteriori error ellipse of Figure 3.19.
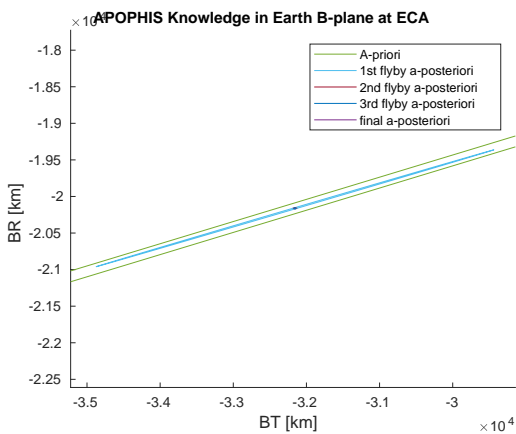
Figure 3.19: Zoomed Apophis Position Error Ellipses in Earth B-plane at ECA
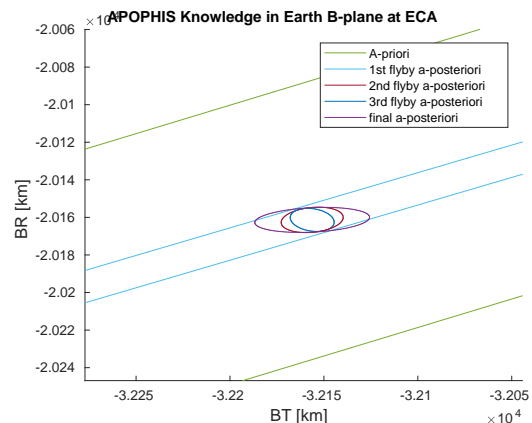
Figure 3.20: Additionally Zoomed Apophis Position Error Ellipses in Earth B-plane at ECA

The diameter of the initial and final 1, 2 and 3-σ ellipses can be seen in Table 3.6.

Table 3.6: Apophis Error Ellipse Diameter Knowledge Evolution [km]

	1-σ	2-σ	3-σ
a priori	64759.2471	106250.4033	146996.6629
1st Flyby a posteriori	2496.6997	4096.3316	5667.2451
2nd Flyby a posteriori	15.7164	25.7859	35.6746
3rd Flyby a posteriori	11.6416	19.1004	26.4252
Mission End a posteriori	27.5532	45.2064	62.5428

Finally, the spacecraft knowledge evolution is also needed to draw some conclusions. This can be seen in Figure 3.21.
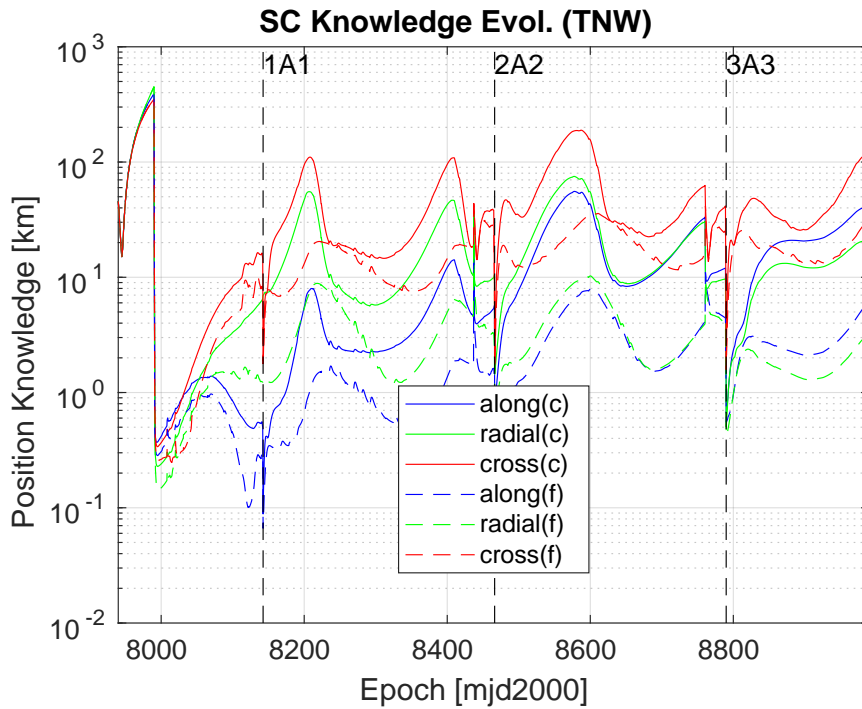
Figure 3.21: SC Position Knowledge Evolution - B_T 0 km and B_R 600 km Trajectory

Now that all the results of the four different flyby trajectories to Apophis have been shown, it is time to interpret the results and draw conclusions. All the conclusions drawn on both this case and further cases have been set up with the help of ESOC mission analysts Waldemar Martens and Ruaraidh Mackenzie.

The first conclusion that can be directly stated is that for this particular trajectory the Apophis knowledge results are independent of the flyby geometry. This can be very well seen from the Figure 3.15: the difference in knowledge evolution is less than 1 km at any point between all four trajectories.

In theory, the asteroid knowledge could be increased up until (but cannot become better than) the spacecraft knowledge. This is true as long as the kilometric weight of the optical measurements are significantly lower than the spacecraft knowledge, recall the end of Subsection 3.2.1. When comparing Figure 3.14 with Figure 3.21, it can be seen the asteroid knowledge improves a lot and becomes close to the spacecraft knowledge, which is as expected. Noted should be as well that for this specific flyby scenario, due to how the spacecraft is pointed towards the asteroid when approaching it, the along-track component is estimated well and the cross-track component relatively well. The radial component however is estimated rather poorly since the exact position of the asteroid in the Line of Sight (LOS) of the spacecraft is not known.

With one flyby the position can be defined quite accurately, however for the velocity two independent measurements are needed. That is why after the second flyby the knowledge improves even further

than the first flyby. At this point the orbital period can be estimated accurately as well, which means the semi-major axis uncertainties become smaller as well. The better knowledge of the orbital period prevents the covariance from increasingly exponentially after the flyby, and rather an oscillatory behaviour of the knowledge components is observed.

After some analysis, it can be concluded that the parameter that dominates the ECA B-plane knowledge is the semi-major axis knowledge, which is directly related to the orbital period by Kepler's third law. This can also be seen from the error ellipses: the reason why the error ellipses are thin is due to the time uncertainty: if the period of the asteroid is badly known, the time of ECA has a large uncertainty. As can be seen, the third flyby does not improve the knowledge as much as the first and second flyby, as there is no additional parameter that will be estimated at this point to give a huge improvement in knowledge (such as the position for the first flyby and the orbital period for the second flyby). From this it can be concluded that for this mission two flybys is the optimal solution in terms of asteroid position knowledge and mission duration.

3.4.2. Case 2: Effect of Input Parameters

Now that some important first conclusions have been drawn, a few input parameters will be changed in order to understand what their effect is, if any, on the knowledge evolution. For all these study cases the trajectory targeting B_T 0 km and B_R 600 km has been used. The same results could be found using any of the other three trajectories, since the results are independent of the flyby geometry for this trajectory, as was concluded before.

First, the optical measurement noise and bias values will be changed from roughly 0.5 pixels (recall Table 3.2) to 1, 2 and 10 pixels. Because of this, many optical measurements will be scrapped due to the kilometric weight constraint discussed at the end of Section 3.2.1. The higher the noise and bias, the lower the amount of measurements. The window to take optical measurements for this trajectory equals 0.645 days (928.8 minutes) due to the opnav constraints. For all trajectories in case 1 a total of 96 optical measurements are taken over the span of three flybys, meaning 32 per flyby. With one pixel bias and noise there will be 57 optical measurements (thus 19 per flyby) and with 2 pixels there will be 30 optical measurements (thus 10 per flyby). Ten pixels has been used to scrap most measurements: only 2 per flyby remain for a total of 6 optical measurements. The results are very similar, thus again only the differences with respect to the baseline case are plotted, as can be seen in Figures 3.22 and 3.23. The baseline case here is again the case from the previous section, thus Figure 3.14 for the knowledge evolution and 3.16 for the knowledge evolution in the Earth B-plane at ECA. Recall from Subsection 3.2.7 that the optical measurement noise and bias for the baseline case is roughly 0.5 pixels. From Figures 3.22 and 3.23 it can be concluded that the results seem to be close to being independent of the amount of measurements taken during a flyby, since the knowledge evolutions is very similar.

Two more cases are analysed, where only a single optical measurement is taken: in the first case the optical measurement is taken at the point in the trajectory where the distance between asteroid and spacecraft is maximised, while the optical navigation constraints are still met. Thus only the leftmost optical measurement of Figure 3.11 is taken into account. The second case is with a single optical measurement at the close approach itself, thus only accounting the rightmost optical measurement of Figure 3.11. The latter case is not physically meaningful, since taking a single optical measurement at exactly the close approach is nearly impossible due to the high relative velocity of roughly 8.73 km/s, recall Table 2.8. This also means that the spacecraft needs to rotate extremely quickly and precisely at the CA in order to successfully point the camera directly towards the asteroid, which is physically not feasible. The case has however been run to understand what theoretically would happen with the knowledge. Since the results differ visibly from the baseline case of Figure 3.14, the knowledge evolution is plotted for both cases and can be seen in Figures 3.24 and 3.25, while the Earth B-plane at CA evolution can be seen in Figures 3.26 and 3.27.

The following conclusions are all based on comparing Figures 3.22, 3.24 and 3.25. The knowledge evolution for all these cases is rather similar, with the exception of Figure 3.24. Especially up until the second flyby the evolution is almost identical. Compare Figure 3.24 with one of the similar figures, such as Figure 3.25: from the second to the third flyby the graphs have slightly different shapes, but nonetheless converge to the same order of magnitude at mission end, except the along-track component. From all these figures it can be concluded that the very first optical measurement is the most impacting one on the knowledge. Additional optical measurements improve the knowledge further, but not as much as the very first optical measurement does. As can be seen in Figure 3.24, the knowledge of a single measurement taken at the furthest point possible also improves the knowledge significantly, but
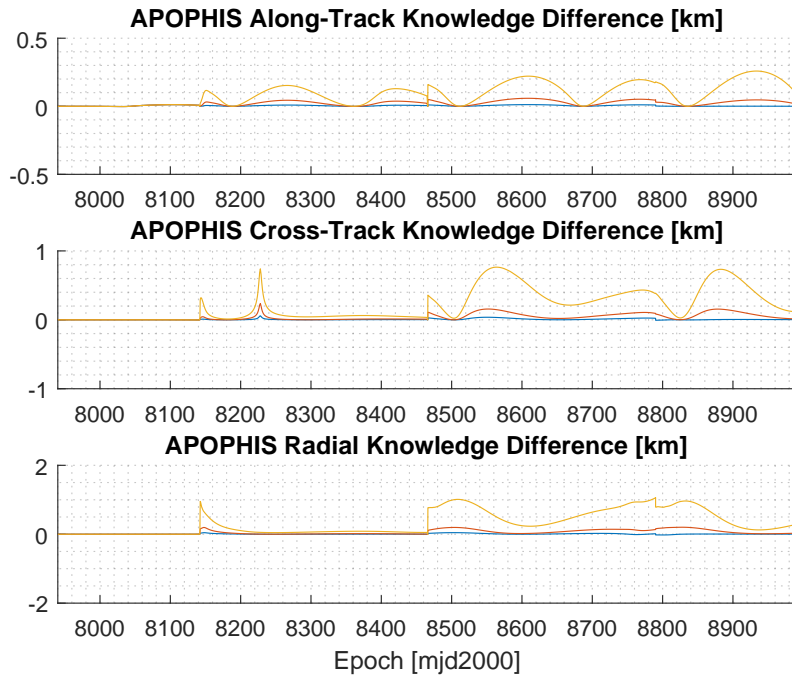
Figure 3.22: Apophis Position Knowledge Evolution - Differences wrt Figure 3.14 - Alternating Optical Measurement Noise/Bias
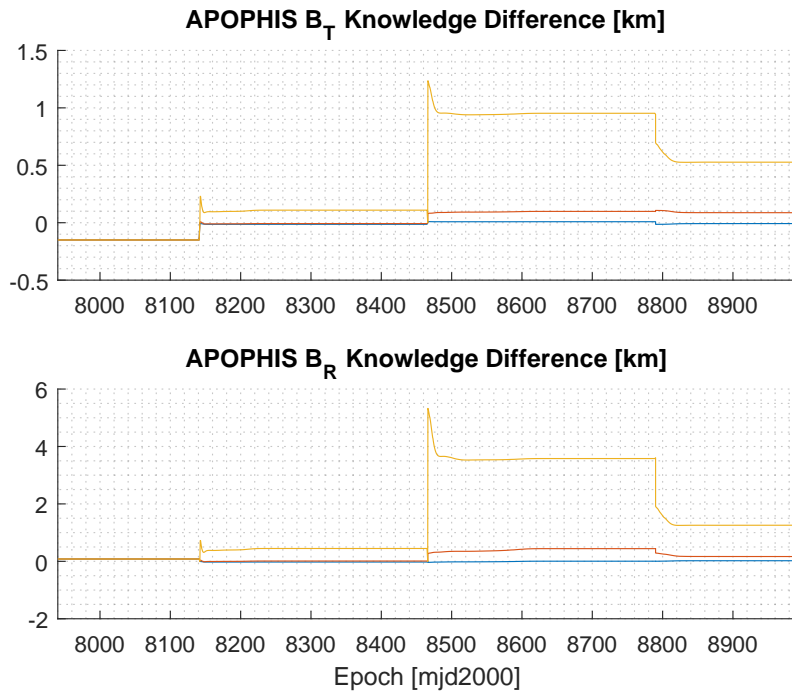
Figure 3.23: Apophis Position Knowledge Evolution in Earth B-plane at ECA - Differences wrt Figure 3.16 - Alternating Optical Measurement Noise/Bias
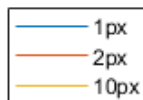
slightly less than a single measurement close to the flyby. Since in practice there will never be a mission with only a single optical measurement, but rather a few, the cases with a multiple measurements are much more relevant. From these figures it can be concluded that a series of optical measurements taken
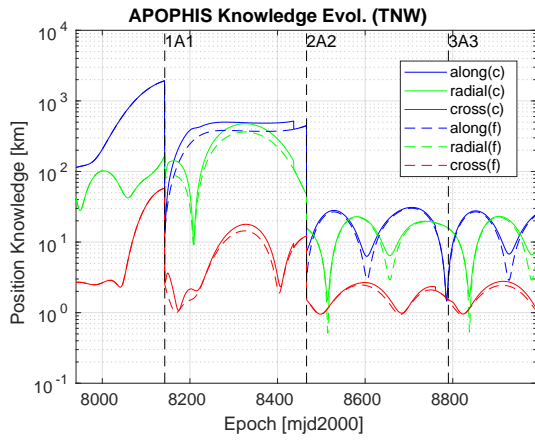
Figure 3.24: Apophis Position Knowledge Evolution - Far Away Single Optical Measurement
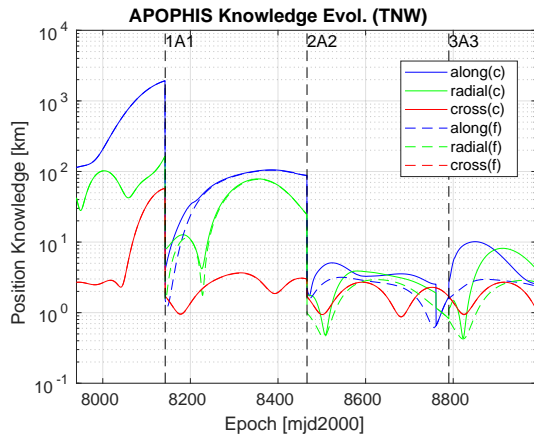
Figure 3.25: Apophis Position Knowledge Evolution - At CA Single Optical Measurement
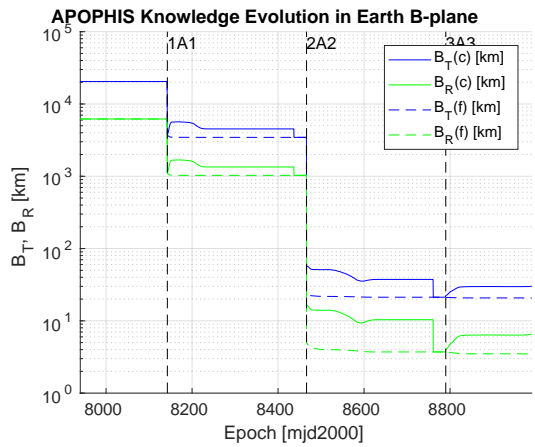
Figure 3.26: Apophis Position Knowledge Evolution in Earth B-plane at ECA - Far Away Single Optical Measurement
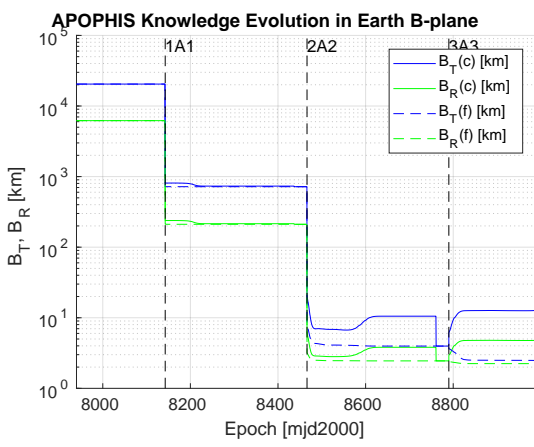
Figure 3.27: Apophis Position Knowledge Evolution in Earth B-plane at ECA - At CA Single Optical Measurement

from far away compared to a series of measurements taken close to the CA do not necessarily mean they are worse. Depending on the flyby geometry and the location of the spacecraft and asteroid at a specific measurement epoch, different components of the asteroid position will be measured. For example, close to the CA the radial and cross-track components will be measured for this particular trajectory, while measurements from far away improve the along-track component especially.

It would be very interesting to see what would happen in case only measurements are taken during the phase where the spacecraft is just flying by the asteroid, and the spacecraft is quickly rotating in order to keep pointing at the asteroid, which means it could be possible to measure all three TNW components accurately. However, for this trajectory it is not possible to take optical measurements after the CA, recall Figure 3.9. Therefore, this study case will be analysed with another asteroid target, in Subsection 3.4.3.

Additionally, the effect of the radiometric measurements is analysed. This is done by decreasing the time interval between measurements. Initially, the interval was 1 hour, which corresponds to 10790 radiometric measurements over a duration of 999.39 days. For this study case the interval has been changed to 2, 4, 6 and 8 hours, while keeping all the other inputs the same. The amount of measurements, in the same duration, is therefore reduced to 5612, 3025, 2206 and 1829, respectively. To draw conclusion on this study case, it is important to also include the spacecraft knowledge results, since the radiometric measurements directly apply to the estimated spacecraft position. Since for this model there are optical measurements throughout the entire mission duration (rather than only when approaching the asteroid), this effect has been shown to impact the asteroid knowledge results extremely little to the point it is barely visible in the graphs, despite the fact the spacecraft knowledge changes slightly. Therefore, once again, it is better to show the differences with respect to the baseline case. The

baseline case is again taken to be Figure 3.14 for the Apophis knowledge evolution, Figure 3.16 for the Apophis knowledge evolution in Earth B-plane at ECA and Figure 3.21 for the spacecraft knowledge evolution. Recall that the radiometric interval for this case was set to 1 hour. The results for this case can be seen in Figure 3.28 for the spacecraft, in Figure 3.29 for Apophis while the knowledge evolution in the Earth B-plane at ECA can be seen in Figure 3.30.
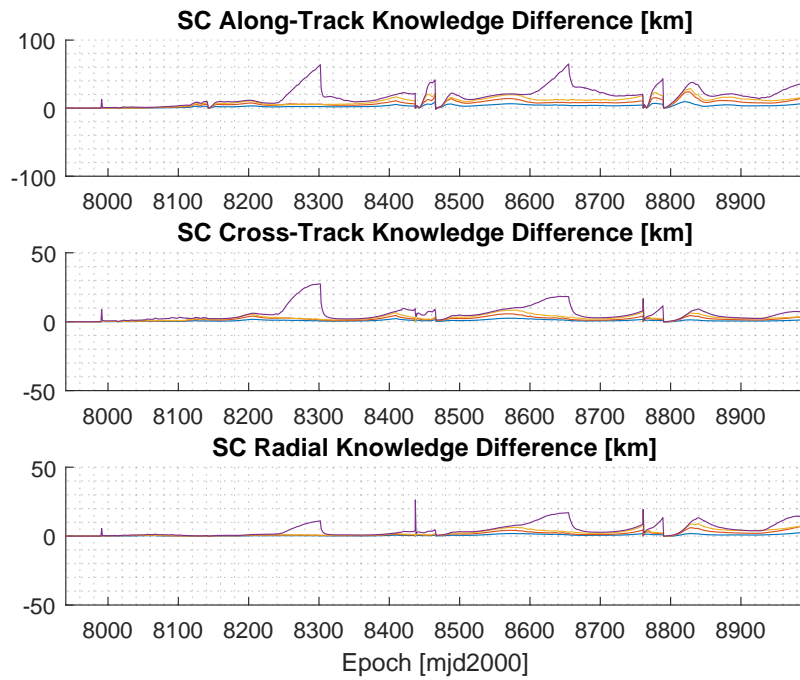
Figure 3.28: Spacecraft Position Knowledge Evolution - Differences wrt Figure 3.21 - Alternating Radiometric Interval
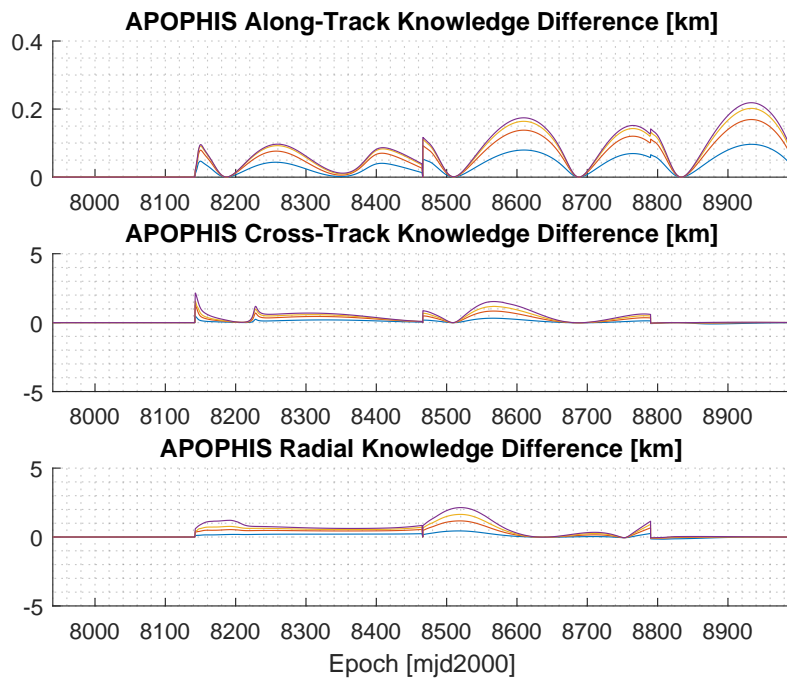
Figure 3.29: Apophis Position Knowledge Evolution - Differences wrt Figure 3.14 - Alternating Radiometric Interval
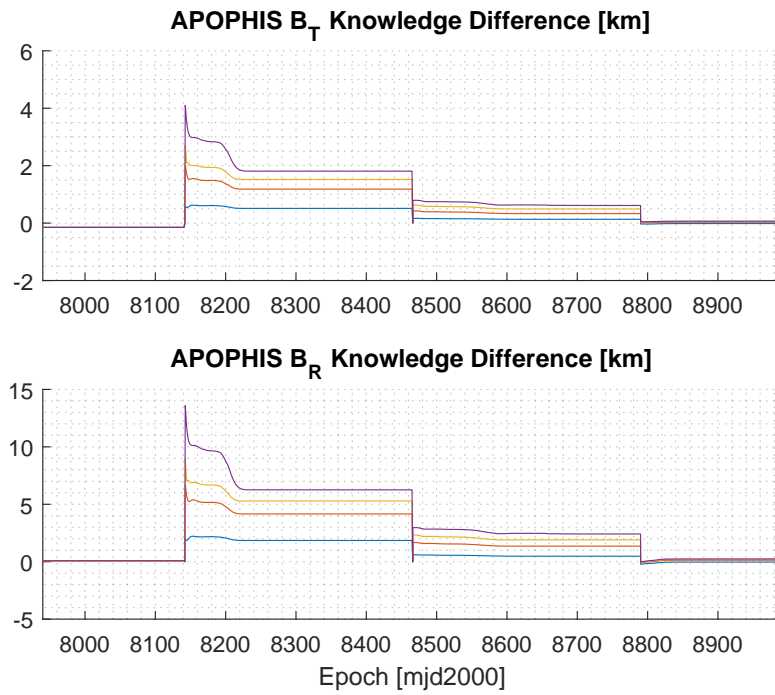
Figure 3.30: Apophis Position Knowledge Evolution in Earth B-plane at ECA - Differences wrt Figure 3.16 -
Alternating Radiometric Interval

Since the differences in Figure 3.28 are so small, it can be concluded that there is no need for many
radiometric measurements during the entire mission duration. Similar accuracy can be achieved with
few measurements, which are appropriately placed. The small differences in the spacecraft knowledge
directly relate to small differences in the asteroid knowledge, as can be seen in Figures 3.29 and
3.30. Possibly, there is no need for radiometric measurements during the entire orbit, but rather
only around the flyby phase, although this is not studied in this thesis and could be a study case for
future work.

Finally, the case where inertial a priori data has been used for Apophis is analysed. As was discussed
in Subsection 3.2.7, a priori RST data from HORIZONS has been transformed to heliocentric EME2000
coordinates to be used in the model. As was discussed in Subsection 3.2.7, the reason for this is that
in the RST frame the correlations are expected to be smaller than in the inertial frame and also less
time-dependent. For this study case, rather than taking RST data and converting to inertial, EME2000
data is taken directly from HORIZONS to see the impact of a priori data. The results can be seen in in
Figures 3.25 and 3.31b. The acronym "EBECA" has been used to shorten "Earth B-plane at ECA" in
the following few figures.

Compare the knowledge evolution of this case in Figures 3.31a and 3.31b with for example Figures
3.14 and 3.16. From this comparison it can be concluded that the simulation is extremely sensitive to
a priori data. The measured components show a very similar behaviour for both cases, but the case
with RST a priori data converges to position knowledge almost a whole order of magnitude lower than
the case with EME2000 a priori data. The only way to improve the situation would be to use a full
a priori covariance matrix that has been generated using the same dynamical model as in the present
analysis.

(a) Apophis Position Knowledge Evolution   (b) Apophis Position Knowledge Evolution in EBECA
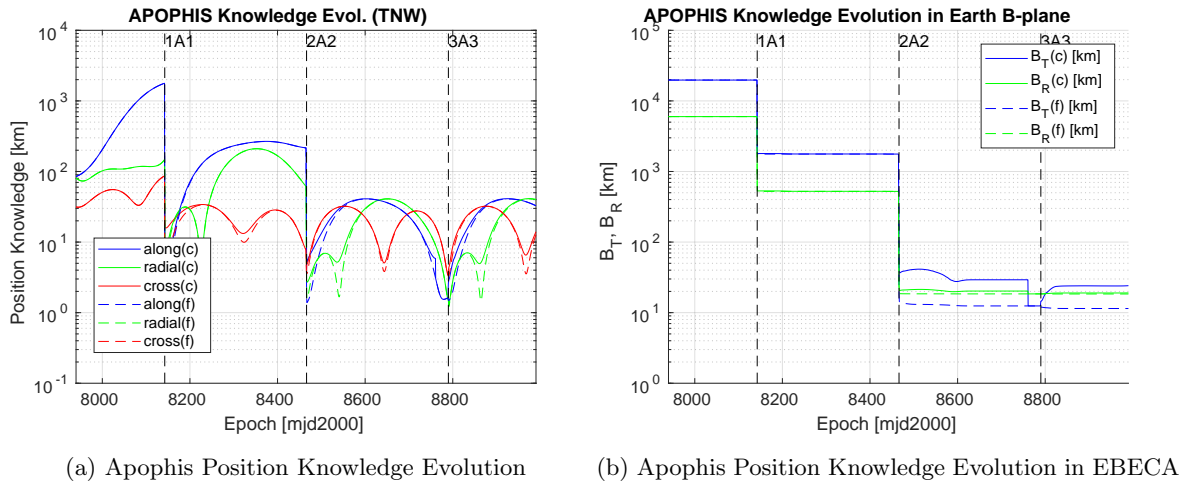
Figure 3.31: Inertial A Priori Results

3.4.3. Case 3: Effect of Asteroid Target

In this study case, the same inputs as study case 1 of Subsection 3.4.1 are used, with the exception of a different spacecraft trajectory kernel. Logically, it also has a different target asteroid and therefore different a priori data. Asteroids UE34 and WN5 have been analysed for this case. The previously mentioned case of having a lot of optical measurements around the exact flyby epoch in order to measure all components accurately, which was not possible for Apophis, has been analysed with asteroid UE34.

All the results as preparation for the covariance analysis for asteroid UE34, such as the flyby geometry and GS coverage, can be found in Appendix C.3. Note that for this trajectory optical measurements are taken both before and after the flyby, as can be seen in Figure C.10. The covariance results can be seen in Figures 3.32a and 3.32b. For this case there are 39 total optical measurements (thus 13 per flyby) over the duration of 0.25 days (360 minutes), and 13585 radiometric measurements over the span of 1258.83 days.

(a) Position Knowledge Evolution   (b) Position Knowledge Evolution in EBECA
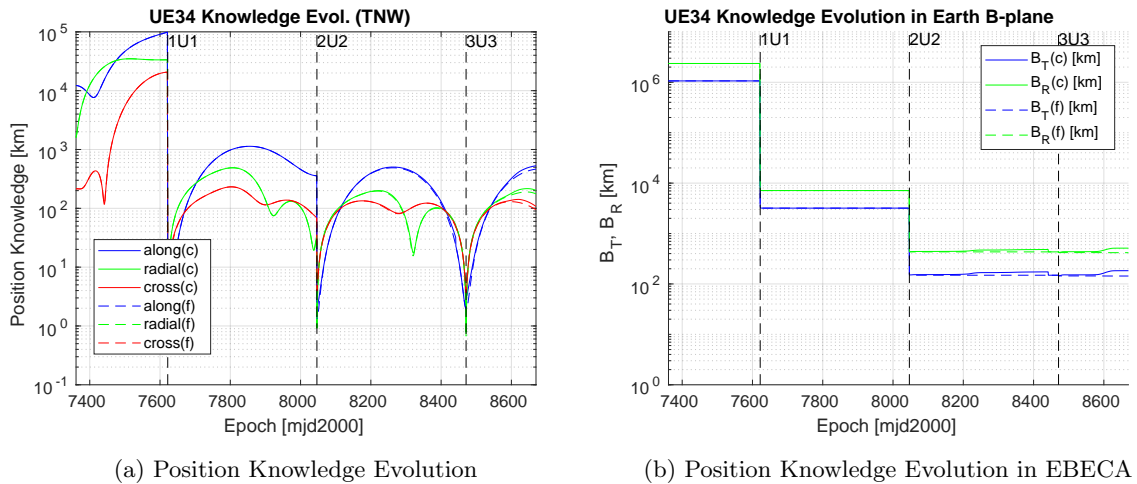
Figure 3.32: UE34 Results

When comparing the UE34 and Apophis position knowledge evolutions, thus Figures 3.32a and 3.14, it can be seen that the conclusions that were drawn for Apophis also hold for UE34: the first two flybys improve the knowledge significantly, while the subsequent flybys not as much. For the Apophis case the improvement was of about two orders of magnitude, since the a priori data for the along-track and cross-track components was roughly 10^2 and improved to roughly 10^0 after the second flyby. UE34 on the other hand improved the a-priori along-track data from roughly 10^4 to 10^2 and the cross-track from roughly 10^3 to less than 10^2, which can also be seen as an improvement of about two orders of

magnitude in two flybys. Because the flyby geometry and both the spacecraft and asteroid trajectories of UE34 and Apophis are very similar, the same conclusions can be found. The error ellipses of this case can be seen in Figure 3.33, while Figure 3.34 is zoomed in on the a posteriori ellipses.
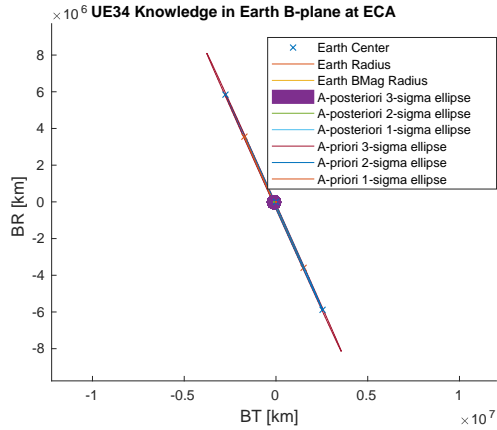
Figure 3.33: UE34 Position Error Ellipses in EBECA
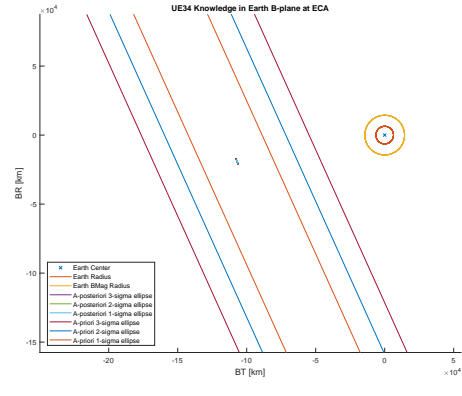
Figure 3.34: Zoomed UE34 Position Error Ellipses in EBECA

As can be seen, the error ellipse is completely outside of the Earth radius and BMag radius (discussed at the end of Subsection 3.2.6). However, this does not necessarily exclude a potential Earth impact. This is because the bias of the ellipse could be different, which means the magnitude of error ellipse is correct but error ellipse origin could be at the wrong position. The analysis in this thesis only reveals the estimated parameters covariance, but not the value of the parameters itself. The 1-σ error ellipse diameter of Figure 3.33 shrinks from 7839195 km to 1650 km, which is an improvement of 3 orders of magnitude.

The case with many optical measurements around the close approach has been analysed for asteroid UE34 as well. The results can be seen in Figures 3.35a and 3.35b. For this case, there are 12 optical measurements per flyby over the duration of 0.003819 days (5.4999 minutes) and 13585 radiometric measurements over 1258.83 days.
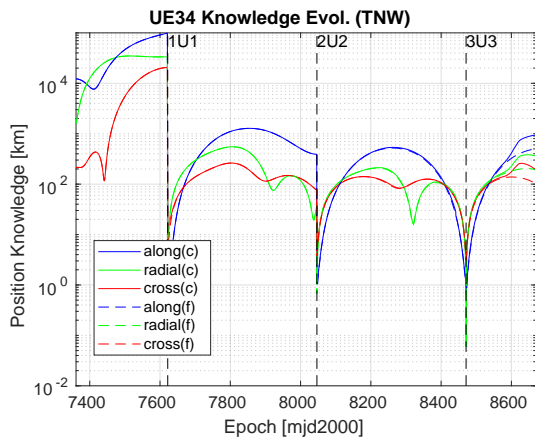
(a) UE34 Position Knowledge Evolution
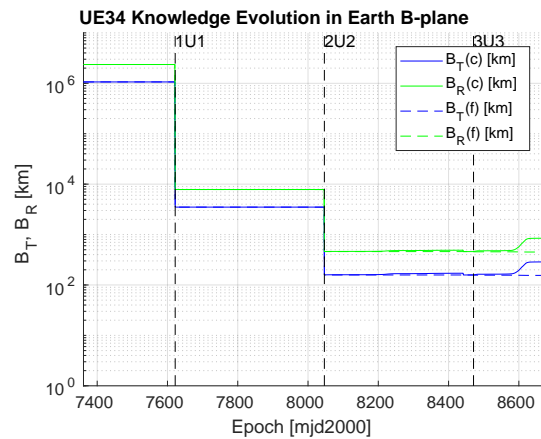
(b) UE34 Position Knowledge Evolution in EBECA

Figure 3.35: Many Optical Measurements around CA Results

These results are rather unexpected. It was expected that every component would have a significant improvement in knowledge due to being able to measure every component well by having all the measurements in a small time frame at the close encounter phase, but when comparing the knowledge to Figure 3.32a, the results are almost identical. Apparently spreading out the measurements over the interval where optical measurements are possible (due to the constraints) gives similar results to having many measurements close to the CA, for this particular target. As was concluded in Subsection 3.4.2, this behaviour could be due to the fact that a single measurement gives a big improvement in

knowledge, while additional measurements are not as impactful. This has however not been tested, as additional study cases would be needed.

Next, asteroid WN5 is shortly analysed. Recall from Section 2.1 that the covariance for this particular asteroid has been run as a bonus study case. It was known beforehand that the results would differ significantly from Apophis and UE34 due to the flyby geometry and spacecraft trajectory. Results that follow from this target asteroid are just generated for curiosity, as the main research of this thesis was based on Apophis and UE34.

All the results to prepare the covariance analysis, such as the flyby geometry and GS coverage, can be found in Appendix C.4. From the optical navigation analysis, it results that for this trajectory there is a 0.417 days (600.48 minutes) window per flyby for optical measurements, during which 21 measurements are taken (thus 63 in total). There are 21863 radiometric measurements over 2039.08 days. As can be seen in Figure C.15, for this case all the optical measurements are taken when approaching the asteroid, and none after the CA. The position knowledge results can be seen in Figure 3.36. Note that for this asteroid no Earth B-plane knowledge figures at ECA are available since the powerful number cruncher machine the simulation is run on runs out of available RAM. Since the trajectory to WN5 has a significantly longer mission duration than the previous cases, the covariance matrices are significantly larger as well. This is due to the fact how NGAs are implemented: at every solution epoch (and recall from Subsection 3.2.4 there is at least one every day) the NGA is estimated, which is modelled as an impulsive manoeuvre. For the case of WN5, the covariance matrix that is generated is approximately 3000×3000 for every output epoch (and there are roughly 2300 output epochs). When trying to propagate this 3000×3000 matrix, the machine runs out of RAM which makes it impossible to plot the Earth B-plane and error ellipse figures. Conclusions will thus have to be drawn based on the knowledge evolution alone.
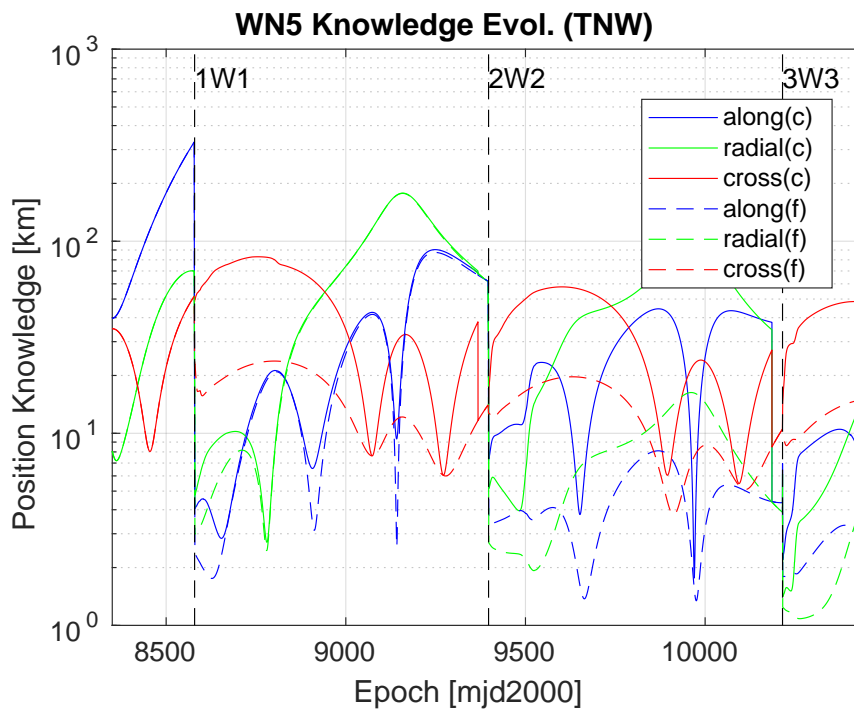
Figure 3.36: WN5 Position Knowledge Evolution

As can be seen from Figure 3.36, the evolution behaves very differently than for Apophis and UE34. The only thing that seems to be consistent, is the big knowledge improvement right after the first flyby. On the other hand, the a posteriori knowledge at mission end of the cross-track and radial components is worse than the a priori knowledge. Therefore, for this particular case, such a flyby mission cannot be justified. One of the main reasons for the difference in knowledge evolution, is the fact that the time between the flybys is much longer compared to Apophis and UE34, meaning the knowledge deteriorates much more. Furthermore, the high eccentricity of the asteroid orbit also plays a role: the encounter geometry is quite different than for the other two asteroids because of this high eccentricity, which means different asteroid state components are measured during the encounters. An interesting study

case would be to analyse the WN5 knowledge evolution with a 2:1 resonant trajectory, but since the WN5 case is a bonus study case, it falls out of the scope of this thesis.

To shortly summarise the results of this chapter, it can be stated that for potentially hazardous asteroids with a near circular orbit at a distance of roughly 1 AU, a multi-flyby mission taking optical measurement at the flybys is a very valid option to improve the orbital uncertainty. Two flybys are needed to accurately determine the orbital period, which will greatly benefit the orbital knowledge. Additional flybys improve the knowledge further, but not as much as the first two. For the two chosen asteroids Apophis and UE34 in particular, the position knowledge can be improved by roughly two orders of magnitude with the proposed mission, while the knowledge of the asteroid in the B-plane at expected impact date can be improved by roughly three orders of magnitude. Few measurements are needed to achieve these results, where the very first measurement is the most impacting for the results. Radiometric measurements could potentially only be needed around the flyby phase, since having radiometric measurements at regular intervals throughout the entire trajectory has been found to add little to no position knowledge.

Spacecraft Analysis

The next step of this research is to perform a first iteration design for the spacecraft, based on all the results gathered from the trajectory and orbit determination analysis in Chapters 2 and 3, respectively. The goal of this chapter is to identify and formulate important spacecraft design requirements. This is done by analysing the mission as a whole, followed by an analysis of all major subsystems using systems engineering techniques. Several design considerations for the relevant subsystems will be discussed as well, and crucial components for every subsystem will be identified, which allows for the generation of an initial mass budget. First, the various phases of the mission and the needed spacecraft modes are analysed in Section 4.1. The launch and Earth escape analysis is discussed in Section 4.2, followed by an instruments analysis in Section 4.3. Then, the propulsion system is assessed in Section 4.4, followed by a GNC analysis in Section 4.5. The data handling system, telecommunications and thermal control system will then be discussed in Sections 4.6, 4.7 and 4.8, respectively. Afterwards, the solar panels are sized and the power budget is set up in Section 4.9, followed by the mass budget assessment in Section 4.10. Feasible platforms for this mission are then analysed in Section 4.11. Finally, all the requirements will be recapitulated in Section 4.12. The methodology used for Sections 4.2 through 4.9 is the following: first an analysis is performed to identify the main requirements for the subsystem, after which design considerations and possible design choices are discussed for that subsystem. The book "Space mission analysis and design" by Larson and Wertz has been used frequently throughout this whole chapter [43].

To start this analysis, all the data from similar missions and studies is gathered, in order to find recurring design choices. Several flyby and rendezvous missions and concepts to small bodies have been researched. A summary of some of the most relevant parameters for all researched reference missions can be found in Appendix D. This data is used frequently throughout this chapter. In addition to this data, some documents of internal ESA studies have been used as a baseline, that can however not be cited. Several design values and considerations in this chapter, such as numbers and components in the mass budget and the performance and cost of the launchers, are based on these internal studies and can thus be considered realistic.

4.1. Mission Breakdown

To start the analysis of the spacecraft, the actual proposed mission for this thesis will be analysed in depth. First of all, it is important to understand the flow of the mission and to distinguish the several phases. A high-level flow of the mission can be seen in Figure 4.1.
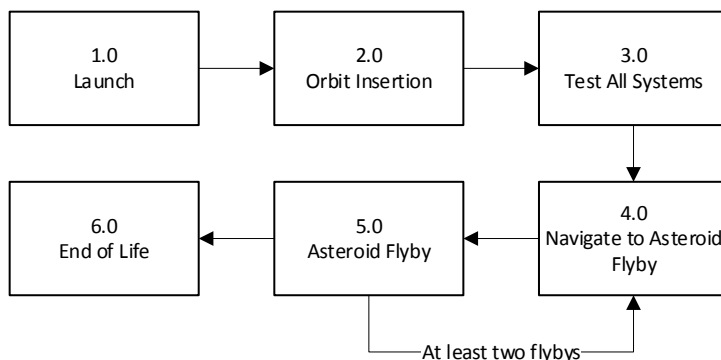
Figure 4.1: Functional Flow of the Mission

The launch phase includes the launch up until the spacecraft separation from the launcher, which is the second phase. During the second phase the spacecraft is separated from the launch vehicle and inserted in orbit. For this particular mission, it is assumed the launcher injects the spacecraft in the desired interplanetary orbit, without the need of the spacecraft propulsion system. Some considerations regarding the launcher will follow later in Section 4.2. Once the spacecraft is on its desired trajectory, all systems are activated and tested to verify everything works as intended. This includes the deployment of the solar array. Phases one through three are known as the Launch and Early Orbit Phase (LEOP). During LEOP, spacecraft controllers work around the clock to verify, check out and configure the satellite, ensuring that all flight control systems and communications are functioning as planned and that critical steps, such as the deployment of solar arrays or attaining a stable orientation and pointing, take place as scheduled[1]. The fourth phase, which is the first phase after the LEOP, entails in navigating the spacecraft towards the asteroid and targeting the desired B-plane parameters. The fifth phase is the science phase, during which the optical measurements are taken. Based on the conclusions of Chapter 3, the fourth and fifth phases are looped for at least two times, after which the End of Life (EOL) phase begins, during which the spacecraft is shut down and disposed. However, three flybys were chosen for this mission in the initial proposal and the trajectories generated in Chapter 2 are optimised for three flybys. For this mission two flybys can thus be considered the nominal case which would ensure mission success, while the third flyby and all further flybys are considered an extension of the mission, in case the spacecraft permits it. Since phases four and five are the most important phases of the mission, these are broken down in more detail, see Figure 4.2. Only the navigation aspects of the mission have been taken into account for this flow diagram.
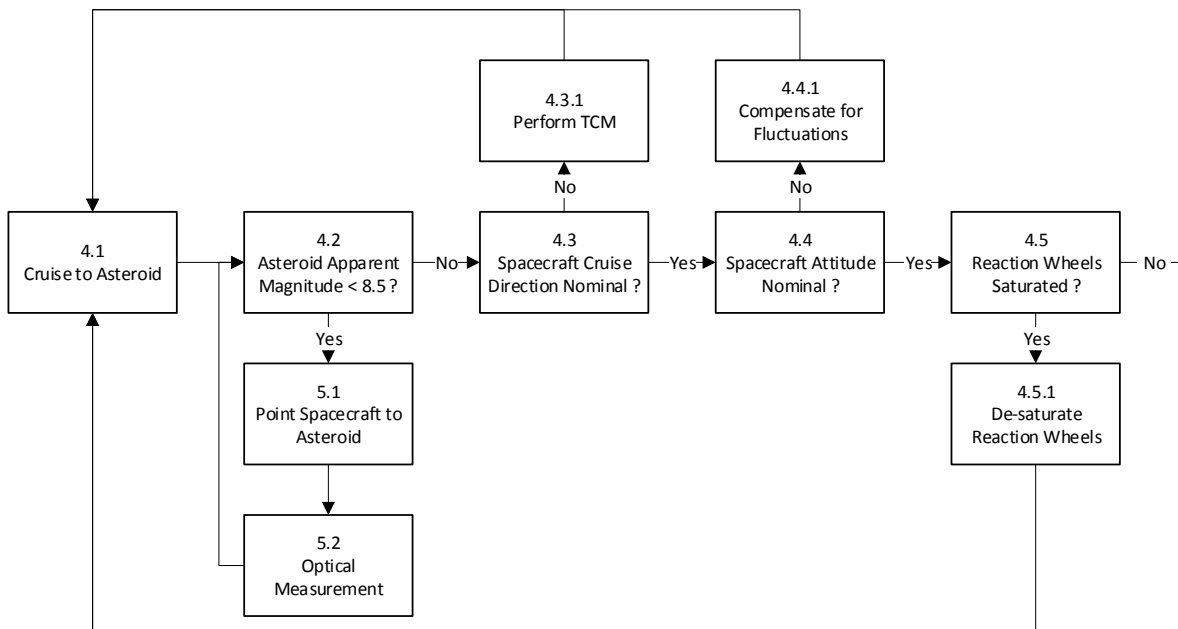
Figure 4.2: Functional Flow of the Core Parts of the Mission

During its cruise towards the asteroid, the spacecraft continuously checks whether the target asteroid is visible. In case the visibility of the asteroid is 8.5 mag or lower, as discussed in Subsection 3.2.1, it means the spacecraft is ready for the science phase, which entails in taking optical measurements. The spacecraft is thus continuously pointed towards the asteroid while optical measurements are taken. When approaching the closest approach point, the spacecraft needs to rotate rapidly in order to keep pointing towards the asteroid. In case the visibility is higher than 8.5 mag, it means the asteroid is still far and no optical measurements will be taken. Therefore the navigation phase continues and other steps can be taken instead. If TCMs are needed to adjust the cruise direction, the propulsion system will take care of this. In case the attitude deviates from the nominal situation, the reaction wheels can compensate for these fluctuations. In case the attitude is as expected, the reaction wheels can be checked for saturation, and desaturated if applicable using the thrusters. This whole process is continuously looped until at least the second flyby, after which it will be decided whether the EOL phase begins or whether an extension of the nominal mission is possible.

---

[1]https://m.esa.int/Our_Activities/Operations/Nonstop_LEOP_full_stop, accessed 23-10-2018

Based on this analysis, the needed spacecraft modes can be distinguished. These are listed below following, where the mentioned phases correspond to the phases in Figure 4.2. Note that only one phase can be activate at a time. Furthermore, these phases will only be applicable between the LEOP and the EOL phases.

1. **Cruise Mode**: this mode can be seen as the nominal mode during which nothing major happens. The spacecraft is oriented in such a way that Earth is visible through the antenna and the solar arrays can provide optimum power. Navigation will be done using the science camera while the star tracker will assure correct spacecraft orientation. The spacecraft will be in this mode when none of the other phases are active, thus during phases 4.1, 4.2, 4.3, 4.4 and 4.5. This means that during the various checks, such as checking spacecraft attitude, the spacecraft will be in cruise mode. Determining the asteroid visibility, phase 4.2, will be performed using the science camera. During cruise mode the communications transmitter is turned on in order to communicate with the ground station.

2. **Science Mode**: this is the mode activated when in proximity of the asteroid, if the magnitude is 8.5 mag or lower, which means optical measurements are possible. During this mode the spacecraft is continuously rotated such that the camera points directly towards the asteroid in order to take optical measurements. While this mode is active the spacecraft will rely on an autonomous navigation system. The mode will be active during phases 5.1 and 5.2.

3. **Manoeuvre Mode**: manoeuvres can either be TCMs using the thrusters or small corrections using reaction wheels. This mode will be active during phases 4.3.1 and 4.4.1.

4. **Momentum Dump Mode**: this mode can be activated during cruise mode if the reaction wheels are saturated. The excess momentum will be dumped using the thrusters, in order for the reaction wheels to be used again to correct for small fluctuations. The mode will be active during phase 4.5.1. It could be argued that it is also necessary to be able to activate momentum dump mode during science mode, in order to not overdesign the spacecraft's reaction wheels for the slew manoeuvres during science, especially if science mode is short. This is however a point to be revisited at a later stage of the design phase.

5. **Safe Mode**: this mode is not shown in Figure 4.2 but is very important nonetheless. When the spacecraft is in this mode, the spacecraft will be oriented in such a way that any residual angular momentum is damped, the solar arrays are in an appropriate orientation for power generation, the communications antenna points towards the Earth in order to communicate with the control room (in case the spacecraft is visible at that time) and the star trackers and navigation camera are pointed away from the Sun in order to avoid blinding. In order to determine the correct spacecraft orientation mentioned above, a Sun sensor is needed. The payload will be in stand-by. This mode will be activated in case of a failure on the spacecraft. The mode will also be active during the LEOP phase. The safe mode described here is based on ESA's AIM v3 study.

6. **Launch Mode**: this mode will be used during the early launch phases before separation. When in this mode, all subsystems are off and the battery is fully charged.

7. **Collision Avoidance Mode**: in case a previously unexpected possible collision is detected, with for example debris, this mode will be activate. When active, the propulsion system will be powered to place the spacecraft in a safe position, which will not result in a collision when switching back to cruise mode. This mode will always be followed up by safe mode.

8. **Hibernation** (Optional): in case only cruise is expected for an elongated period of time, it can be chosen to put the spacecraft in hibernation. Only some vital subsystems will be kept active, such as the thermal control system in order to avoid components from breaking, while the rest is shut off. Communication with the ground station will also not be possible, and the only way to get out of hibernation is to program the spacecraft to autonomously re-activate itself after a certain period of time. The spacecraft will consume very little power when in this mode due to most systems being shut off.

Now that all the modes have been analysed, the next step is to identify the interactions between all the modes. This can be visualised in Figure 4.3.
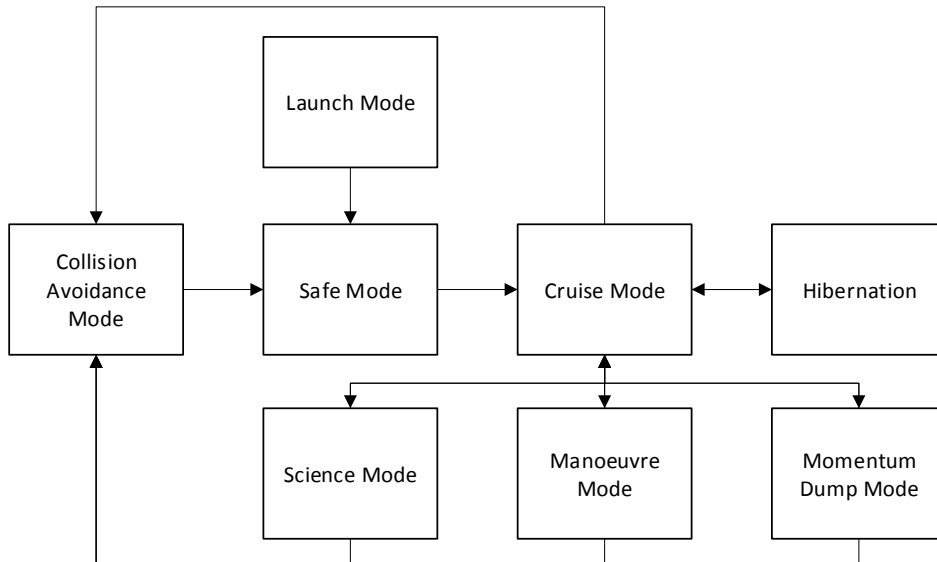
Figure 4.3: Interaction Between Spacecraft Modes

Note that, despite not being depicted in Figure 4.3, safe mode can be activated by all modes, including hibernation. Safe mode is always followed up by cruise mode. Collision avoidance mode can be activated by any of the active modes, thus when the spacecraft is not shut off. This mode is always followed up by safe mode.

From this mission breakdown, it becomes clear that the spacecraft will need at least reaction wheels, a star tracker and a Sun sensor in terms of GNC (Guidance, Navigation and Control), while an IMU is also needed to ensure three-axis attitude determination. It will furthermore need a solar array to power the various subsystems, will need a camera to take optical measurements which can also be used for navigation purposes and will need a propulsion system to perform TCMs and desaturate the reaction wheels. The RCS (Reaction Control System) will thus consist of reaction wheels and the propulsion system thrusters.

Now that these key components have been identified, their respective subsystems will each be analysed in more detail in the next sections. But first, a few general mission requirements will be identified. Here, the MFM identifier stands for multi-flyby mission and MIS for mission.

Table 4.1: Mission Requirements

Identifier	Requirement
MFM-MIS-01	The mission shall provide optical measurement data during at least two flybys to asteroid Apophis.
MFM-MIS-02	The mission cost shall be less than 100 M€, including launch and operations.
MFM-MIS-03	The spacecraft shall have a mission lifetime of at least 2.5 years.

4.2. Launch and Earth Escape

Regarding the launch, two main options are considered for this research in order to reach the desired interplanetary orbit. The first option is to use a medium-sized launcher, such as a Soyuz, to put the spacecraft directly into an Earth escape trajectory. The second option is to use a lighter launcher to bring the spacecraft into an Earth orbit and then using an upper stage for the Earth escape. In order to assess the two options, first a main requirement for the spacecraft configuration is identified in Table 4.2, based on reference data from Appendix D. The identifier CFG stand configuration.

Table 4.2: Spacecraft Configuration Requirements

Identifier	Requirement
MFM-CFG-01	The spacecraft shall have a dry mass less than 150 kg.

The option to have a medium-sized launcher is extremely expensive, especially considering the spacecraft proposed for this study will fall in the small satellite category (satellites with a mass up to 500 kg), according to requirement MFM-CFG-01. To have a dedicated launcher to bring such a small spacecraft into interplanetary orbit could mean the cost budget, as stated by requirement MFM-MIS-02 in Table 4.1, will not be satisfied. One of the cheapest options would be a Falcon-9, with a price of about 54 M€. Note that this would be an enormous overkill, since the performance to LEO of a Falcon-9 is 22800 kg[2].

On the other hand, using an upper stage for the Earth escape seems like a much more viable solution in terms of cost. Smaller launchers could be used in this case, as the spacecraft will be injected into a much lower demanding orbit in terms of dV. Some possible viable options have been summarised in Table 4.3, with the Falcon-9 included as reference.

Table 4.3: Possible Launchers

Launcher	Performance to LEO [t]	Cost [M€]
Vega	~ 2.4	~ 30
ROCKOT	~ 2.1	~ 30
PSLV	~ 3.2	~ 25
Falcon-1	~ 0.9	~ 7
Falcon-9	~ 22.8	~ 54
Delta-II	~ 5.8	~ 52
Dnepr	~ 4.5	~ 25

The cheapest option would be a rocket such as the Falcon-1, which itself is a retired rocket. However, most likely Vega is the preferred launcher due to being a European launcher and this thesis being developed in collaboration with ESA.

Some existing upper stages, to be used in case Vega would be chosen as a launcher, are for example the bi-propellant PROBA-IP upper stage, which was initially proposed for Lisa Pathfinder and has a cost of roughly 17 M€, or the well known solid propulsion STAR upper stages, which cost roughly 5 M€. The STAR upper stages have proven to be good choices for interplanetary missions. Deep Space 1 and Stardust successfully reached their interplanetary orbit using a STAR 37 upper stage, while Deep Impact, Dawn, NEAR Shoemaker and New Horizons (all researched in Appendix D) have flown with a STAR 48 engine.

Alternatively, the combination of having an upper stage and having a shared launch or piggybacking with another missions is possible as well. However, mass and volume restrictions could be a problem for this option, since the required upper stage to reach interplanetary trajectory for this option has a large mass and volume.

The option of using Vega in combination with an upper stage such as the STAR 48 seems the most viable solution for this mission. Note that the TCM calculations in Chapter 2 would still be valid for this case, since the dV required for Earth escape would be fully provided by the upper stage.

When using an upper stage, it is important to estimate the amount of propellant it will need in order to be able to confirm the full configuration mass (thus spacecraft and upper stage) does not exceed the launcher performance. Assuming the Vega launcher will put the spacecraft in a 300 km circular LEO orbit, some simple calculations will follow to get a first estimation for the propellant needed. The velocity of a circular orbit can be calculated with:

$$V = \frac{\mu}{r} \tag{4.1}$$

while the Earth escape velocity is calculated using:

$$V_e = \frac{2\mu}{r} \tag{4.2}$$

---

[2]https://www.spacex.com/about/capabilities, accessed 23-10-2018

The dV required to escape Earth can be estimated by subtracting the circular velocity from the Earth escape velocity. The result can be seen in Figure 4.4 for altitudes ranging from the Earth surface to 500 km.
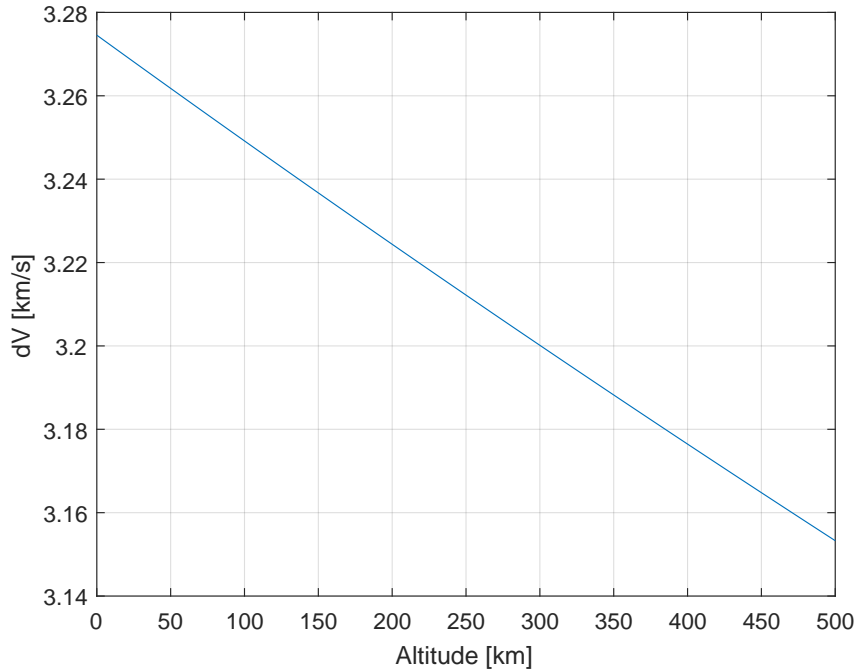
Figure 4.4: dV Needed for Earth Escape

As can be seen, a velocity increment of 3.2 km/s is needed for an altitude of 300 km. In order to get a first approximation of the propellant needed for this increment, the well known rocket equation is used.

$$\Delta V = g_0 \cdot I_{sp} \cdot \ln \left(\frac{m_d + m_f}{m_d} \right) \tag{4.3}$$

Where m_d, m_f are the dry mass and fuel mass, respectively. For this particular case, the dry mass consists of the full configuration mass without the upper stage fuel mass. This thus consists of the spacecraft mass, the spacecraft fuel mass, the upper stage dry mass and finally the mass of the adapter to attach the upper stage to the spacecraft. The result of rewriting the rocket equation for m_f, with a variable dry mass, can be seen in Figure 4.5. The I_{sp} of the STAR 48 upper stage is 287 s.

With this analysis it should only be checked whether the total configuration mass is within the limits of Vega. The dry mass limit of 150 kg, as stated in requirement MFM-CFG-01 in Table 4.2, is used for this assessment. Propellant mass will be assessed later in Section 4.4, but considering the TCMs shown in Section 2.5 a very conservative guess for the propellant mass of 10 kg will be used. The STAR 48 dry mass, including a 20% system margin, is expected to be roughly 250 kg, with the adapter mass roughly 20 kg. A very conservative estimation of the expected configuration dry mass will thus be 430 kg. Using the data from Figure 4.5, this means the STAR 48 fuel mass will be 910.50 kg. The total configuration wet mass at launch will thus be roughly 1340 kg, which is well within the Vega performance to LEO capabilities, which is 2.4 tonnes, recall Table 4.3. The proposed upper stage configuration for Earth escape is thus a valid option.

The spacecraft would still need its own propulsion system in order to perform the TCMs, as the upper stage is expended once it has reached the interplanetary orbit.
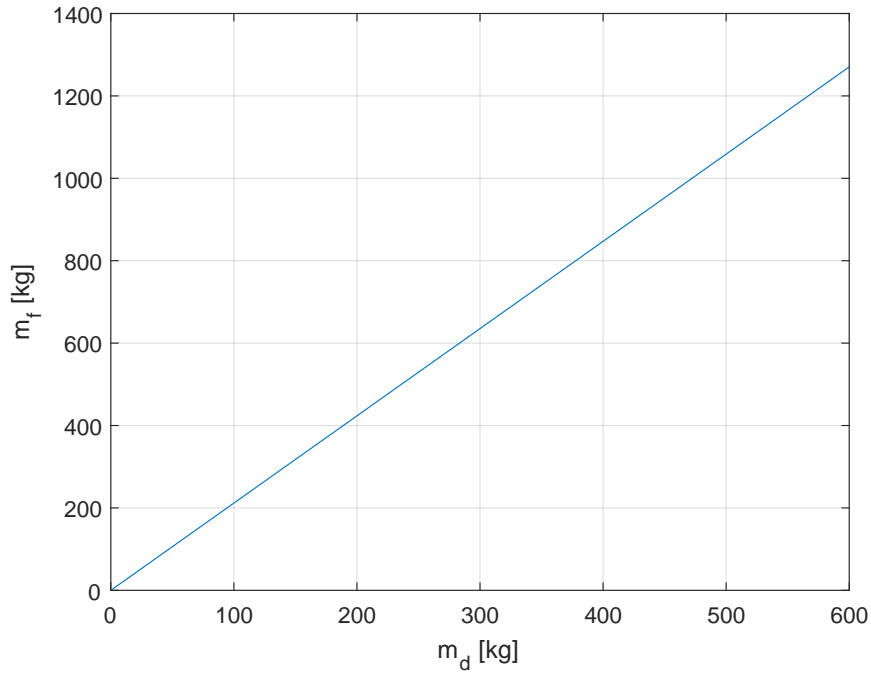
Figure 4.5: Fuel Mass for the STAR 48 Upper Stage

4.3. Instruments

The only instrument at this point of the design to be taken into account is a camera, which can be used both for navigation purposes and for science (thus taking the optical measurements during the flyby). Additional science instruments are considered to be out of the scope of this thesis, but could be added at a later design stage. The option of having a LIDAR, in addition to the camera, for very accurate position measurements when in proximity of the asteroid, has been analysed. This option has however been discarded, since a LIDAR works at distances of approximately 30 m to 25 km. The closest distance between asteroid and spacecraft for this mission will be 600 km, which is thus outside of the LIDAR range.

The primary goals of the camera are to navigate the spacecraft towards the asteroid in the pre-flyby phases, and to be able to target the asteroid during the close approach phase to take optical measurements. Secondary goals of the camera are to retrieve information on the target asteroid, such as diameter, shape and spin rate. The secondary goals require higher imaging capabilities than the primary goal. Any improvement in performance towards the primary goal would thus be beneficial towards the secondary goals.

Some preliminary calculations will be done for three types of cameras, in order to assess what type of camera will be best for this mission. The analysis has been done for a wide angle camera, a narrow angle camera and a camera with angle in between the two. Cameras with a FoV of 0.5, 2 and 5 degrees have been selected for this purpose, which are three recurring cases in ESA studies for preliminary instrument assessments. First the field of view per pixel is calculated in μrad. Then the resolution, in terms of the size of one pixel on the target, is calculated, using:

$$hFoV = 2 \cdot WD \cdot \tan\left(\frac{aFoV}{2}\right) \tag{4.4}$$

$$s_{px} = \frac{hFoV}{n_{px}} \tag{4.5}$$

where $hFoV$ and $aFoV$ are the horizontal FoV in km and angular FoV in degrees, respectively, while WD is the working distance, thus the distance between the spacecraft and asteroid. For this analysis the closest approach distance of 600 km has been used. Furthermore, s_{px} and n_{px} are the size of one

pixel on the target and number of pixels on the detector, respectively. The focal distance of the camera is then calculated using:

$$F_{cam} = \frac{h \cdot WD}{hFoV} \tag{4.6}$$

where h is the horizontal dimension of the detector. For this equation, the number of pixels and the pixel size need to be known. Based on recurring reference data, a detector with 1024×1024 pixels and a pixel size of 10 μm has been selected for these calculations. A camera with a f-number, denoted by $F\#$, of 7.45 has furthermore been selected, also based on reference data, which is then used to calculate the entrance pupil aperture, using:

$$D_{cam} = \frac{F_{cam}}{F\#} \tag{4.7}$$

The results for the three analysed cases can be seen in Table 4.4.

Table 4.4: Calculated Camera Parameters

FoV [deg]	5	2	0.5
$hFoV$ [m]	52393.1	20946.1	5236.0
FoV/px [μrad]	85.2	34.1	8.5
s_{px} [m]	51.2	20.5	5.1
F_{cam} [mm]	117.3	293.3	1173.4
D_{cam} [mm]	15.7	39.4	157.5

For navigation purposes, a wide field of view is preferred since this would maximise the number of visible bright stars, while for science purposes a narrow field of view is preferred instead since this gives a high resolution. However, a camera with a narrow field of view in combination with a star tracker would be a perfect option for this particular mission. The star tracker is used for navigation throughout most of the cruise, and the camera is used for early detection of the asteroid due to its large aperture. The camera can then be used for fine guiding due to its high resolution during the stages before the science phase activates. During the science phase, the high resolution of about 5 meters per pixels would yield optical measurements of great quality for this mission. Based on this analysis, it can be concluded that a NAC (Narrow Angle Camera) is preferred for this mission. This camera would be sufficient to fulfil the primary goal of the camera and would also be adequate to fulfil the secondary goals due to the high resolution.

From this short assessment, the main payload requirements can be identified, which are:

Table 4.5: Instrument Requirements

Identifier	Requirement
MFM-PLD-01	The spacecraft shall have an optical camera as the main science instrument.
MFM-PLD-02	The science camera shall be used in combination with GNC equipment for navigation.

Based on these initial payload requirements, some possible existing cameras have been researched to understand what is achievable for such a mission in terms of camera performance. From the many cameras researched, the cameras used for Dawn and Hayabusa 2, listed in Appendix D, could both be good options for this type of mission, since they both have flown and both were used for science and navigation purposes and have adequate performance parameters to meet the primary and secondary camera goals mentioned earlier. The camera used on Dawn will be used as a baseline for the remainder of the section, since detailed information is publicly available on the camera, unlike the Hayabusa 2 camera. The Dawn camera has a mass of 5.5 kg.

4.4. Propulsion

The propulsion system of the spacecraft will be discussed in this section. The propulsion system is needed in order to perform tasks such as planned orbital manoeuvres, emergency collision manoeuvres and desaturasing the reaction wheels. Throughout this section, the following references have been frequently used:[3] [44] [45] [46] [47] [48] [49] [50].

A preliminary propulsion system assessment has been performed, in order to understand whether there is a propulsion system which is clearly better than other options. For this purpose, three propulsion types with very different performance parameters (primarily I_{sp} and thrust) have been chosen to carry out the analysis. For each engine type, a possible propellant has been assigned in order to perform the needed calculations. A butane cold gas system, a hydrazine mono-propellant system and a xenon ion engine have been chosen as the options, as these are frequently used options.

The GMAT trajectory generation tool described in Section 2.4 has been revisited for this analysis. The impulsive burns have been replaced by finite burns in order to implement the various engine types. The multiple shooting method as depicted in Figure 2.4 is no longer valid for this approach, since an additional epoch has to be accounted for. The revised multiple shooting method can be seen in Figure 4.6, where the green and red arrows depict forward and backward propagation, respectively.
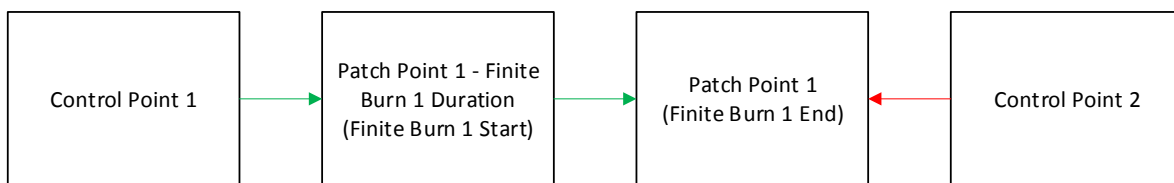
Figure 4.6: Revised Multiple Shooting Method

Since a finite burn involves a burn duration, the additional epoch that has to be accounted for is the epoch corresponding to the patch point epoch minus the burn duration, which is when the finite burn is started. The way the velocity increment is varied is different as well compared to the method described in Section 2.4. In the previous analysis, the three dV components were directly varied, since it involved an instantaneous increment in that direction, meaning thrust and I_{sp} were not needed. With the revisited finite burn model however, the three unit vectors depicting the burn direction are varied, along with the burn duration. The total velocity increment can then be calculated by rewriting the rocket equation, previously introduced in Equation (4.3):

$$dV = g_0 \cdot I_{sp} \cdot \frac{M_p}{M} = g_0 \cdot I_{sp} \cdot \dot{m} \cdot \frac{t_b}{M} = F \cdot \frac{t_b}{M} \tag{4.8}$$

where $\dot{m}$ is the mass flow and t_b is the burn time. This equation involves the assumption that the propellant mass, M_p, is small compared to the satellite total mass, M, which is a valid assumption for this mission. The increment in each direction can then be calculated by multiplying the dV with the varied unit vectors. The same equation can also be used to determine the needed propellant mass. Since the burn time directly relates to the propellant mass, the latter is the optimisation parameter in the revised simulation. Besides the finite burn implementation, the rest of the simulation, as described in Section 2.4, has been kept the same. In an initial analysis, fixed values for the thrust and specific impulsive for the three engine types have been used. An important assumption that has been made here, to keep the simulation simple, is that no throttling takes place. This means that in these simulations the engine will give the full thrust over the duration of the burn. It is made sure that all the resulting resonant trajectories for this analysis are based on the same trajectory used for the covariance analysis by making sure the launch and flyby epochs are the same as the ones in Table 2.6, the trajectory is the same as the one in Figure 2.9 and the flyby geometry is the same as the one in Figure 3.11. The results can be seen in Table 4.6. The chosen thrust and I_{sp} combinations have been selected based on the references mentioned at the beginning of this section in combination with the researched reference missions in Appendix D.

---

[3]https://sst-soa.arc.nasa.gov/04-propulsion, accessed 01-11-2018

Table 4.6: Results of Propulsion Simulations - Fixed Engine Parameters

Engine	Thrust [N]	I_{sp} [s]	Burn Time [s]	dV [m/s]	M_p [kg]
Mono-Prop	1	230	1460	9.73	0.6471
	10	230	47	3.13	0.2083
Ion	0.001	3000	695604	4.63	0.0236
	0.01	3000	118507	7.90	0.0403
Cold Gas	0.05	75	14168	4.72	0.9628

It should be noted that due to the complexity of this optimisation problem, it is not possible to determine whether the found solution is a local optimum or a global optimum. A wide variety of inputs have been tried for each case, but only the result with the lowest burn time has been tabulated. From this analysis, one can see that all three systems could potentially be feasible, since they all lead to small velocity increments, and thus a small needed propellant mass less than 1 kg. Based on these results, one could potentially exclude the butane cold gas system as it requires significantly more propellant than the hydrazine or xenon options. However, before excluding the cold gas system, a second analysis is performed where the thrust and I_{sp} values have been made variable as well, rather than fixed as in the previous analysis. The applied ranges for these parameters can be seen in Table 4.7.

Table 4.7: Typical Performance Parameters of Selected Engine Types

Engine	Thrust Range [N]	I_{sp} Range [s]
Hydrazine Mono-Propellant	1 - 10	200 - 250
Xenon Ion	0.001 - 0.01	1000 - 3000
Butane Cold Gas	0.001 - 0.1	35 - 75

The results from this second analysis can be seen in Table 4.8. For the "generic" case in this table, the entire variables range has been used, thus thrust ranging from 0.001 to 10 N and I_{sp} from 35 to 3000 s. While obviously not every thrust and specific impulse pair corresponds to an existing engine and propellant, the generic case has been run to see whether the solution could be representable for an engine type. In theory, the generic case should find the best combination of parameters leading to the smallest propulsion mass since it has access to the full range of input parameters. However, in reality the optimisation process often results in a local optimum.

Table 4.8: Optimum Results for Variable Engine Parameters of Table 4.7

Engine	Thrust [N]	Isp [s]	Burn Time [t]	dV [m/s]	M_p [kg]
Mono-Prop	9.967	250	47	3.12	0.1911
Ion	0.01	3000	24170	1.45	0.0073
Cold Gas	0.1	75	1472	0.97	0.1981
Generic	0.074	1628	2341	1.15	0.0108

As can be seen from this analysis, the statement based on the previous analysis that the cold gas system can be excluded was not valid. As a matter of fact, based on these new results, the cold gas system could potentially be the best solution of the three due to its extremely low complexity and low needed propellant mass. In general, cold gas systems are limited in terms of achievable dV due to their low specific impulse. However, since the needed velocity increment for this case is low, the cold gas system is very feasible, especially considering the ability to achieve small impulse bits and a large number of possible impulse cycles that are relevant for precise positioning and attitude control manoeuvres. Another factor to be kept in mind, is the possible thrust range of a cold gas system. For the analysis in this section, the thrust was assumed to be constant over the duration of the burn. In reality, throttling can take place during a manoeuvre, which makes cold gas a great option due to its wide thrust range, recall Table 4.7. The analysed mono-propellant system can however be considered a viable solution as well: it is a simple system and requires a low propellant mass for this trajectory. Its high thrust (compared to the other two systems) makes it an interesting option for quick manoeuvres due its low burn duration. The electric propulsion option has the lowest needed propellant mass of the three, which is expected due to the very high I_{sp}. However, the system is much more complex than the other options, and furthermore would require a high amount of power for a long period, since the

burn duration is approximately 7 hours. Considering the available solar panel power analysis in Section 4.9, an electric system could potentially be hard to achieve for this mission, without involving bigger solar panels or more powerful batteries. The option should however not be discarded, as other systems could potentially be put in standby mode in order to allocate more power to the propulsion system, even though not the most optimal solution. Finally, the result of the generic case could be matched to a xenon ion thruster system with 7 thrusters of 0.01 N, due to the resulting combination of thrust and I_{sp}. However, due to the nature of the optimisation strategy the solution could be a local optima, of which this solution is the perfect example: the solution for the ion engine results in a comparable solution that needs a lower propellant mass. The solution of the generic case can thus be discarded.

Before moving on to possible design solutions, the basic propulsion system requirements will be stated in Table 4.9, where the identifier PRP stands for propulsion.

Table 4.9: Propulsion System Requirements

Identifier	Requirement
MFM-PRP-01	The propulsion system shall be able to perform at least two TCMs.
MFM-PRP-02	The propulsion system shall be able to desaturase the reaction wheels.

There are several options for the propulsion system, which are visualised in the Design Option Tree (DOT) of Figure 4.7.
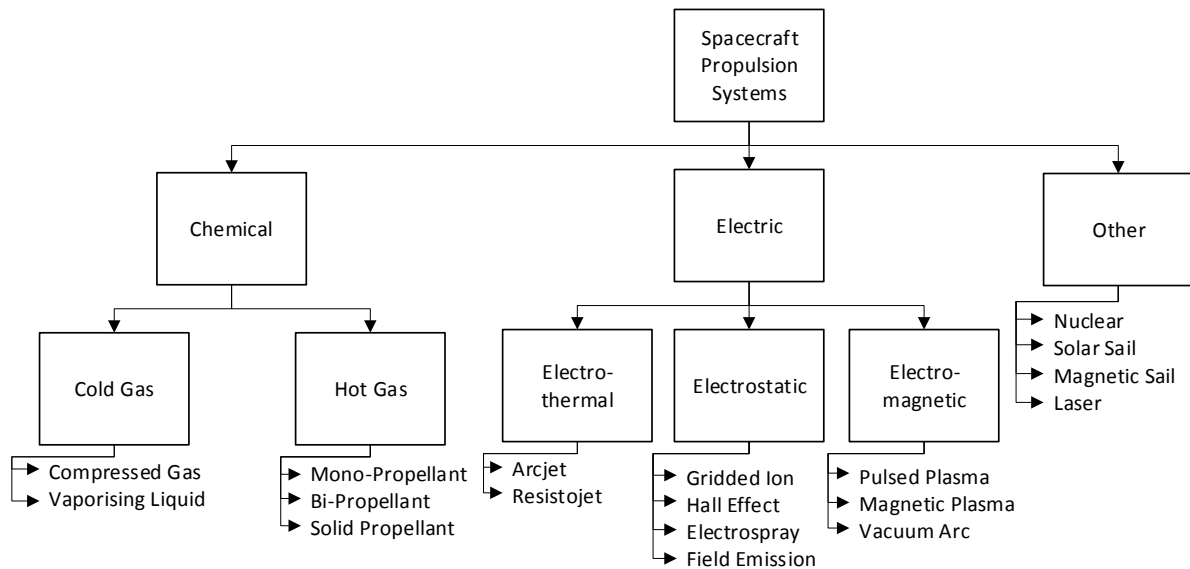
Figure 4.7: Propulsion System Design Option Tree

All the options will now be very briefly assessed, without going in too much detail since describing each option comprehensively falls out of the scope of this section. As can be seen, the two main categories are chemical and electric propulsion. All the other options are gathered in a remaining category. Nuclear propulsion can be discarded, since it is a rather unconventional method that is still in early study phases. Solar sailing, magnetic sailing and laser propulsion are three rather new types of propulsion that do not require any propellant to be expelled in order to generate thrust. Even though all three options seem very promising, they have not been studied well enough to be widely use for space applications yet and have therefore been discarded.

Chemical propulsion can be further divided in cold gas and hot gas systems. Cold gas systems have been proven to be an excellent option for propulsion applications in space. They have been frequently used for all kinds of manoeuvres, ranging from LEO orbit station-keeping to deep space manoeuvres. The cold gas system has a good efficiency while having an extremely low complexity, since it involves mainly a tank, valves, thrusters, tubing and fittings. Its low budget, mass and volume makes it an excellent option for this mission. Propellants can be either compressed gasses, such as nitrogen, or vaporising liquids, such as butane. Hot gas systems are another very common propulsion type for space applications. The system can either involve a solid propellant, a single liquid propellant or a

combination of two liquid propellants. A solid propellant system is not a valid option for this mission, as they cannot be turned off once ignited. A very small manoeuvre will thus be impractical with this system. Mono-propellant systems are widely used for both planetary and interplanetary orbital manoeuvres. It is a reliable option for this mission, since mass and volume of this system is compact and suitable to fit small spacecraft busses. Hydrazine or hydrogen peroxide are usually chosen as the propellant. Bi-propellant systems on the other hand consist of an oxidiser and a fuel that when mixed create thrust. The system is typically complex since two independent fluid feed systems, two tanks and two valve sets are needed, which do not make it an interesting option for this mission. Typical propellants are monomethylhydrazine (MMH) or unsymmetrical dimethylhydrazine (UDMH) as the fuel and dinitrogen tetroxide or mixed oxygens of nitrogen (MON) as the oxidiser.

Differently than chemical systems, in electric propulsion an electric power system is used to accelerate the exhaust. In small satellites, electrical power is usually supplied by the solar panels, hence the frequently used name Solar Electric Propulsion (SEP) for these systems. Electrothermal, electrostatic and electromagnetic systems can be distinguished. In electrothermal systems the propellant temperature is increased using heat generated by electrical power. While these systems have proven to have higher performance than several chemical systems, the added complexity makes it unfeasible for small satellites. Electromagnetic thrusters accelerate the ions using the Lorentz force generated by a magnetic field. Magnetic plasma dynamics thrusters, pulsed plasma thrusters and vacuum arc thrusters can be distinguished. However, these three options are not feasible for this mission, either because of their low efficiency (pulsed plasma and vacuum arc) or because of high thrust levels (magnetic plasma). The remaining SEP type to be discussed are the electrostatic engines. The electrostatic propulsion systems are the most evolved type of SEP engine. In these engines charged particles, usually ions, are accelerated by electrical forces when falling through a drop in potential across two electrodes. Gridded ion engines and hall effect thrusters are highly developed SEP systems and have been used in several space missions and typically use xenon as propellant. Field Emission Electrostatic Propulsion (FEEP) and electrospray (also called colloid) thrusters work similarly, but differ from ion and Hall thrusters in the way charged particles are produced. Liquefied metal propellants such as indium, gallium or cesium are usually used.

From this short analysis it can be concluded that the three engine types used for the simulations earlier in this section could all three be good choices for the proposed mission. Some possible options for these three will now be researched to match each case with an existing feasible option. As a hydrazine option, MOOG's MONARC-1 or MONARC-5 are excellent options[4]. These thrusters provide a thrust force of 1 N and 4.5 N, respectively, and have a specific impulse of roughly 227 seconds. Both thrusters have a mass less than 0.5 kg and only require 18 W of power. A cold gas option could be Surrey's butane propulsion system[5], which provides 50 mN of thrust and a specific impulse of about 80 seconds. An ion thruster possibility is the Busek BIT-3 engine with xenon propellant, which has a thrust of 1.15 mN and a specific impulsive of 2100 seconds and only requires 75 W of power. The Modular Propulsion System (MPS) for small satellites, designed by Aerojet Rocketdyne, is a good example that has options for all three engine types[6]: the MPS-220 is a hydrazine mono-propellant system that carries two 22 N engines and eight auxiliary 1 N engines, the MPS-270 is a gridded ion thruster for small satellites and the MPS-120 is a cold gas system.

As becomes clear from this discussion and the simulations at the beginning of this section, all three proposed engine types could be viable for this spacecraft. A butane cold gas system could be argued to be the best option due to its simplicity and low propellant mass, however the other two options should not be discarded as they are in fact feasible as well, and additional requirements and considerations in further design stages could potentially make it the best option. In the remainder of this chapter, the spacecraft is assumed to have a hydrazine system, relevant primarily for the power budget calculation in Section 4.9 and the mass budget calculation in Section 4.10.

4.5. GNC

Ground controlled navigation has a limit to the achieved accuracy. The error is typically in the order of 10 km for position and 1 m/s in velocity. Since the diameter of the Apophis is roughly 300 m and the relative flyby velocity will be roughly 8.73 km/s, there is a need for highly accurate navigation in

---

[4]https://www.moog.com/content/dam/moog/literature/Space_Defense/Spacecraft/Monopropellant_Thrusters_Rev_0613.pdf, accessed 02-11-2018

[5]http://www.sst-us.com/downloads/datasheets/us_prop_butanepropulsionsystem_2013-12.pdf, accessed 02-11-2018

[6]http://www.rocket.com/smallsat, accessed 02-11-2018

order to fly the nominal trajectory. Furthermore, considering the flyby velocity, it is not possible for the ground commands to be received, processed and executed in time to account for navigation errors. Therefore, there is a need for an autonomous GNC system on board of the spacecraft. The goal of this autonomous GNC system is to navigate the spacecraft towards the asteroid and provide the needed rotation during the flyby phase.

Before setting up some general GNC requirements, a short analysis has to be done for the most critical phase where precise attitude control is required: the science phase. During this phase the spacecraft has to rotate very quickly to keep the camera pointing towards the asteroid in order to take optical measurements. It is therefore crucial to identify a requirement for the needed slew rate. The slew rate can be easily computed by rewriting the angular velocity equation:

$$v = \omega r \tag{4.9}$$

By applying this equation to a space application, v is in fact V_∞ while r is the flyby distance. The angular velocity, in this case the slew rate, can then be computed. A figure containing all the values up to a flyby distance of 1000 km and a V_∞ of 30 km/s can be seen in Figure 4.8.
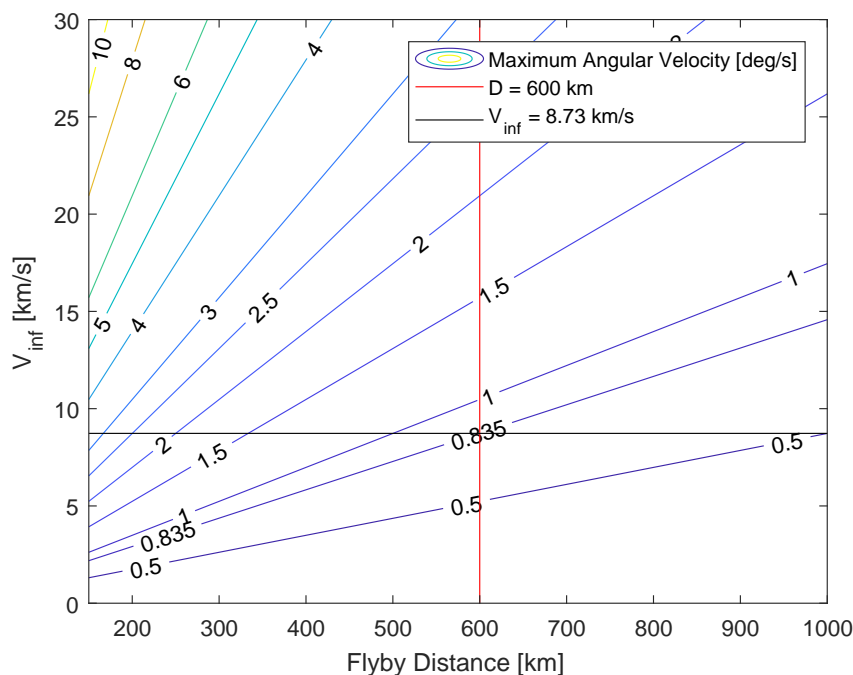
Figure 4.8: Maximum Slew Rate for Combination of V_∞ and Flyby Distance

Since for this case the minimum distance to the asteroid will be 600 km and the relative velocity will be roughly 8.73 km/s the maximum angular velocity will be roughly 0.835 deg/s, as can be seen from the figure. Since for most small agile spacecraft the maximum reachable slew rate using reaction wheels is roughly 1 deg/s, the slew rate for this mission is achievable. The general GNC requirements can now be identified and are tabulated in Table 4.10.

Table 4.10: GNC Requirements

Identifier	Requirement
MFM-GNC-01	The GNC system shall be able to navigate the spacecraft autonomously.
MFM-GNC-02	The GNC system shall be able to provide a slew rate of 0.83 deg/s.
MFM-GNC-03	The GNC system shall be used to three-axis stabilise the spacecraft.

Now that the main GNC requirements are established, some design choices can be discussed. As became clear from the spacecraft mode analysis in Section 4.1, a Sun tracker will be needed for the safe mode, a star tracker to determine orientation to facilitate the autonomous navigation (aided by the science

camera) and reaction wheels are needed to correct small fluctuations and rotate the spacecraft during science mode. To facilitate the LEOP and safe mode phases, a total of four Sun sensors will be needed, evenly distributed in order to have full coverage around the spacecraft. Four reaction wheels are needed to have full and redundant attitude control of the spacecraft. One star tracker is sufficient, since a single star tracker can contain multiple optical heads. For example the Sodern Hydra star tracker with three optical heads and one electrical unit is a good configuration for this mission[7]. The electrical unit is internally redundant which means a second one is not needed. In addition to these components, Inertial Measurement Units (IMUs) are needed as well to complete the GNC system. The Northrop Grumman LN200 IMU would be a perfect choice, since it has three solid-state fibre-optic gyros and three solid-state silicon Micro Electro-Mechanical System (MEMS) accelerometers in a compact package that measures velocity and angle changes in a coordinate system fixed relative to its case[8]. A total of two of these IMUs would be a good selection for this mission in order to meet the GNC goals.

4.6. Data Handling

The Data Handling System (DHS) will perform various tasks. A non-exhaustive list of the most important tasks can be seen below.

- Demodulate and decode ground commands
- Interface the GNC components
- Control the RCS components
- Monitor battery status
- Control heaters in order to keep temperature inside acceptable limits
- Provide data storage capabilities for unprocessed data during ground link outages
- Run applications, such as the autonomous GNC software
- Acquire data for transmission to the ground station

Based on this list, the main requirements for the DHS can be identified, which can be seen in Table 4.11, where the DHS identifier stands for Data Handling System.

Table 4.11: Data Handling System Requirements

Identifier	Requirement
MFM-DHS-01	The DHS shall be able to monitor all spacecraft sensors.
MFM-DHS-02	The DHS shall be able to control all spacecraft actuators.
MFM-DHS-03	The DHS shall be able to interpret ground commands.

Now that the main requirements have been established, some design considerations can be discussed. Based on reference data, it has been identified that the DHS for this mission needs at least a CDMU (Command and Data Management Unit), a RTU (Remote Terminal Unit) and a camera controller. The combination of these components is sufficient to meet all DHS requirements and perform the tasks from the list at the beginning of this section. The camera controller is needed to process the images taken of the asteroid during the flyby, in order to not burden the main on-board computer during the flyby phase. The CDMU is the on-board computer, and is responsible for a wide variety of tasks, including the processing of the data received from the GNC components and storing data during outages. The RTU on the other hand implements the physical interfaces to the propulsion system and the GNC actuators, in this case the reaction wheels. A simple visualisation of the DHS architecture and the interaction with some GNC and RCS components can be seen in Figure 4.9.

Valid examples for the three discussed data handling components are the following: the OSCAR on-board computer designed by Airbus as the CDMU, RUAG's AFIO as the RTU and Airbus's NPAL as the camera computer. Another option is to have an existing system where all three components are present, such as the Airbus AS250 platform, Verheart Space's ADPMS spacecraft controller or Surrey's OBDH, which is part of the SSTL-150 platform.

---

[7]http://www.sodern.com/website/en/ref/Hydra_316.html, accessed 23-10-2018
[8]https://www.northropgrumman.com/Capabilities/LN200FOG, accessed 23-10-2018
[8]https://spaceequipment.airbusdefenceandspace.com/avionics/platform-on-board-computers/oscar/,   accessed 24-10-2018
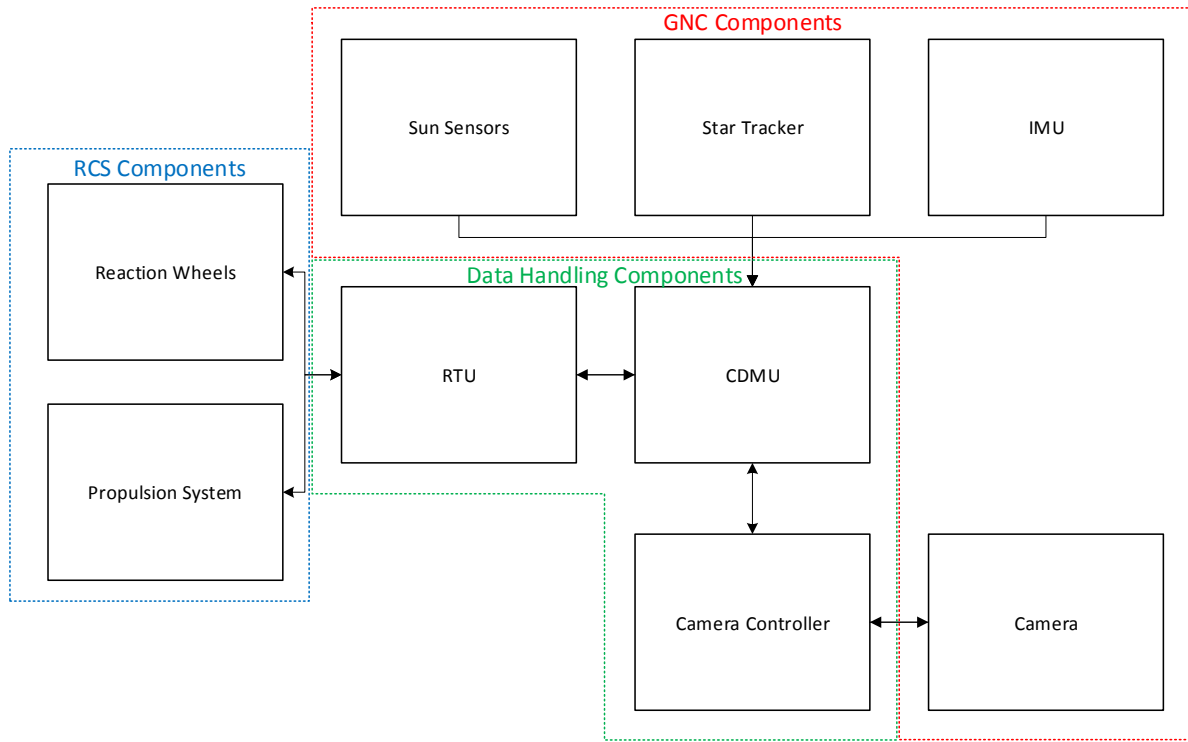
Figure 4.9: Data Handling Architecture

4.7. Telecommunications

The communications system will be responsible for all TT&C (Telemetry, Tracking and Command) activities throughout the entire mission. It will thus be responsible for the data link with the ground station, when visible, during all phases and any mode, including safe mode. Through the TT&C system it will also be possible to obtain two-way range and Doppler measurements. Important to note is that all considerations in this paragraph are formulated in order to be in line with the relevant ECSS (European Cooperation for Space Standardisation) standards [51] [52].

This mission will be more than 2 million km from the Earth surface, and would thus be recognised by ESA as a deep space mission. For deep space mission, the use of S-band is not supported by ESA's ESTRACK (European Space Tracking) network [53]. X-band shall therefore be considered instead, with downlink frequencies between 8400 and 8450 MHz and uplink frequencies between 7145 and 7190 MHz. An X-band Deep Space Transponder (DST) is thus needed for this spacecraft. Furthermore, there are three Deep Space Antennas (DSAs) in the ESTRACK network that can be used to communicate with ESA deep space missions, which had been introduced previously in Subsection 3.4.1. An important requirement is that the minimum ground visibility will be reached at maximum distance between Earth and spacecraft, which is achieved at a data rate of 1.5 kbps or higher. This data rate should at least be present during the TCMs as well. Note that the elevation should be at least 10 degrees, which is consistent with the GS coverage plots presented in the results of Chapter 3.

After this initial analysis, the main requirements for the TT&C system can be identified. These are listed in Table 4.12, where the identifier COM stands for communications.

Table 4.12: Communication Requirements

Identifier	Requirement
MFM-COM-01	The TT&C system shall be able to communicate with ESTRACK DSAs.
MFM-COM-02	The DSTs shall use X-band for uplink and downlink.
MFM-COM-03	The TT&C system shall provide a data rate of at least 1.5 kbps at maximum Earth distance.

Some design considerations will follow now that the main requirements have been identified. Based on similar ESA studies, it is found that having the combination of one fixed High Gain Antenna (HGA)

with a gain of 37.5 dBi and at least one Low Gain Antenna (LGA) with 5 dBi gain is a valid option
for this type of mission. The addition of a Medium Gain Antenna (MGA) does not add any value for
this type of mission and the option has thus been discarded. On the other hand, having two LGAs
on opposite sides of the spacecraft would be ideal in order to maximise coverage. The HGA will have
a maximum diameter of 1 m in order to make sure to adhere to launcher volume restrictions. As an
assumption, the maximum radio frequency power of the Travelling Wave Tube Amplifier (TWTA) is
assumed to be 35 W, which results in an EIRP (Equivalent Isotropic Radiated Power) of 47.5 dBW,
which will guarantee the 1.5 kbps visibility at maximum distance. The frequency power is estimated
using Figure 4.10, where the pointing accuracy error is estimated to be 0.5 degrees.
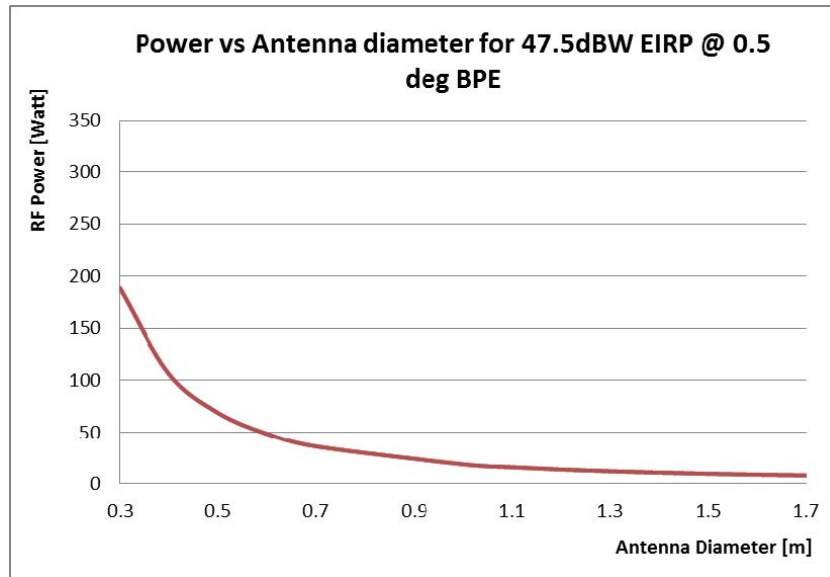
Figure 4.10: Antenna Diameter and Radio Frequency Power [53]

Besides the antennas, the X-band DST to transmit the signals and the TWTA (which includes the
Electric Power Conditioner (EPC)) to provide the frequency power, the TT&C subsystem will also
require a Radio Frequency Distribution Network (RFDN) to connect the DST and TWTA with the
antennas. This component is furthermore in charge of selecting the operating antenna, and to split the
uplink and downlink signals. The complete TT&C subsystem proposed for this mission will thus consist
of two X-band DSTs, two TWTAs, one RFDN, two LGAs and one HGA. Now that the components
have been analysed, the basic architecture of the telecommunications subsystem can be set up. This is
shown in Figure 4.11. Note that the connections within the RFDN itself have been omitted from this
analysis.
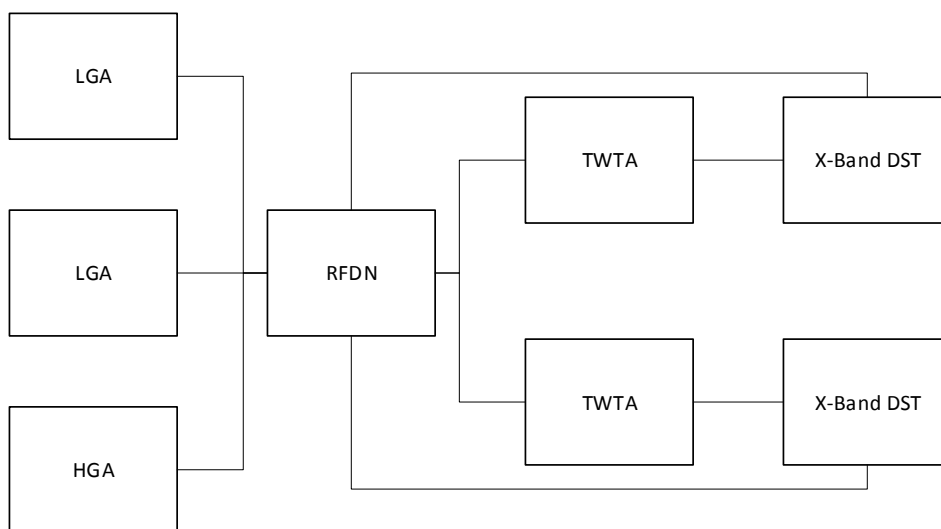
Figure 4.11: Communications Architecture

4.8. Thermal

The Thermal Control System (TCS) will provide the necessary thermal environment for the spacecraft in order to ensure adequate subsystem performance for the entire duration of the mission. The necessary thermal environment consists of adequate temperature ranges, temperature gradients and thermal stability.

First of all, a brief analysis on the spacecraft temperature is performed, in order to understand the cooling and heating needs of the spacecraft. In order to do this, the distance to the Sun for this mission is needed. Figure 4.12 shows the spacecraft distance to the Sun for the duration of the entire mission.
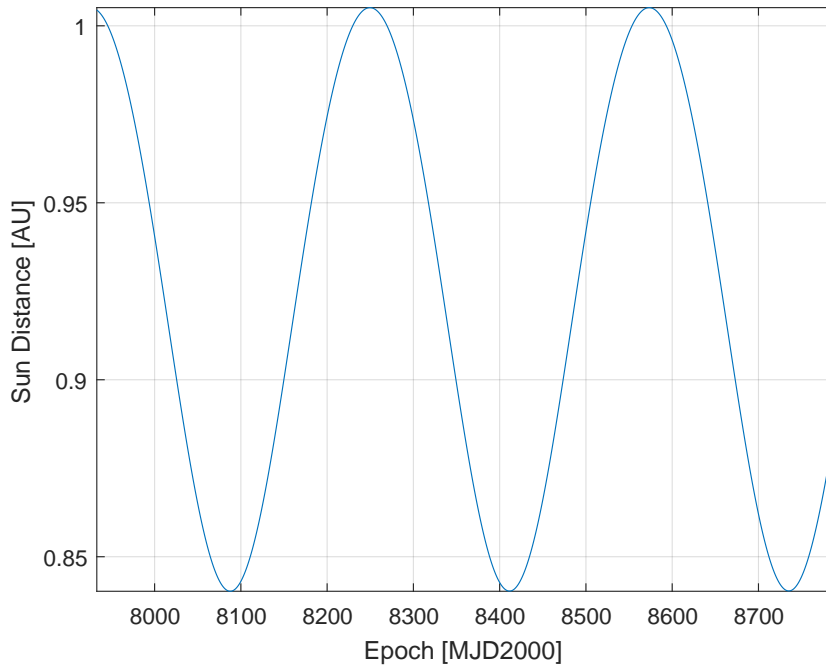
Figure 4.12: Spacecraft Distance to Sun

As can be seen, the minimum distance is roughly 0.8402 AU while the maximum distance is roughly 1.005 AU. The distance is needed to calculate the solar flux. This is calculated using:

$$F = \frac{L}{4\pi d^2} \tag{4.10}$$

where L is the Sun luminosity, $3.845 \cdot 10^{26}$ W. The solar flux for this particular mission can be visualised in two different ways: in Figure 4.13 the solar flux as a function of the Sun distance can be seen while in Figure 4.14 the solar flux as a function of the mission epoch can be seen.

The maximum, minimum and average value of the solar flux for this mission have been tabulated in Table 4.13.

Table 4.13: Solar Flux Analysis Values

Parameter	Min	Mean	Max
Distance to Sun [AU]	0.8402	0.9213	1.0051
Solar Flux [W/m^2]	1353.2943	1630.1753	1936.5508
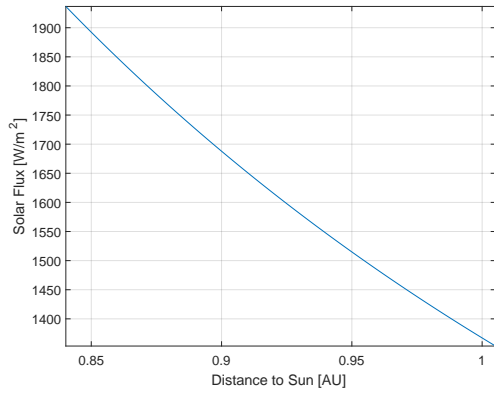
Figure 4.13: Spacecraft Solar Flux - Function of Sun Distance
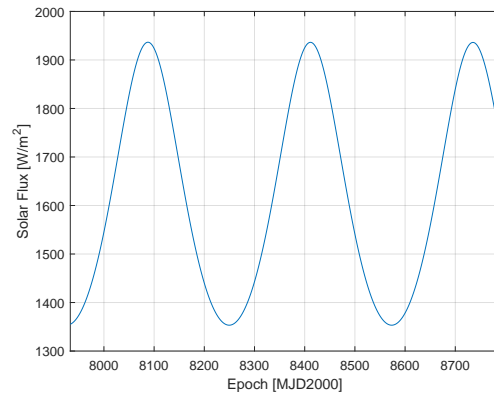
Figure 4.14: Spacecraft Solar Flux - Function of Mission Epoch

Once the solar flux is known, the temperature can be estimated, using:

$$T = \sqrt[4]{\frac{\alpha}{\varepsilon} \frac{F}{4\sigma} + 2.7^4} \tag{4.11}$$

where the 2.7 constant comes from the cosmic microwave background radiation, σ is the Stefan-Boltzmann constant, $5.67 \cdot 10^{-8}$ W·m^{-2}·K^{-4}, while α and ε are the solar absorptivity and IR emissivity, respectively, which are dependent on the coating used on the spacecraft. Some typical values can be seen in Table 4.14.

Table 4.14: Properties of Common Coatings [43]

Type of Coating	α [-]	ε [-]
2 mil silvered teflon	0.05 - 0.09	0.66
2 mil aluminised teflon	0.10 - 0.16	0.66
Z93 white paint	0.17 - 0.20	0.92
Chemglaze Z306 black paint	0.92 - 0.98	0.89
1 mil aluminised kapton	0.38	0.67
Bare aluminium	0.09 - 0.17	0.03 - 0.10

A temperature analysis has been done the same way as the solar flux analysis: the temperature as a function of the Sun distance has been shown in Figure 4.15 and the temperature as function of the mission epoch can be seen in Figure 4.16. The analysis has been run for all the coatings of Table 4.14, in addition to considering the spacecraft as a black body (thus $\alpha = \varepsilon = 1$). The used values for the absorptivity and emissivity can be seen in the legend of Figures 4.15 and 4.16.

Just as the solar flux analysis, the minimum, maximum and average values for this mission's spacecraft temperatures have been tabulated in Table 4.15.

Table 4.15: Spacecraft Temperature Analysis Values [^{o}C]

Coating	Min	Mean	Max
Black body	4.9097	17.3000	30.8383
Silvered teflon	-114.4684	-107.3976	-99.6716
Aluminised teflon	-87.9087	-79.6543	-70.6352
White paint	-88.2192	-79.9787	-70.9748
Black paint	9.4821	22.0761	35.8370
Aluminised kapton	-31.8456	-21.0931	-9.3444
Bare aluminium	64.2042	79.2366	95.6618
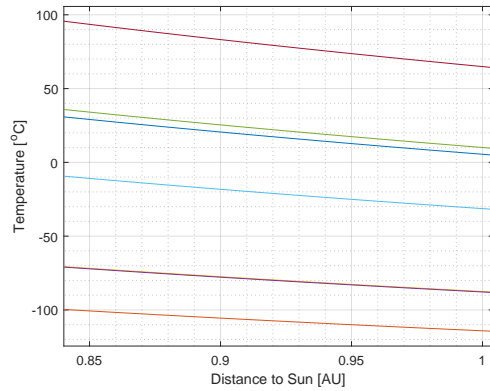
Figure 4.15: Spacecraft Temperature - Function of Sun Distance
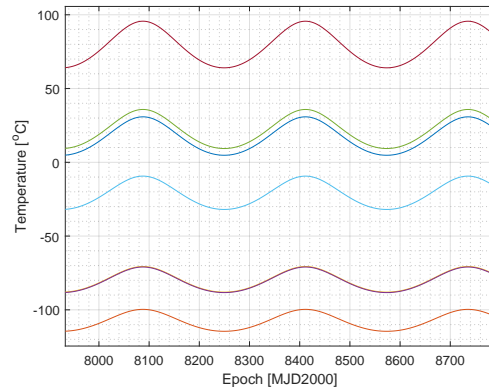
Figure 4.16: Spacecraft Temperature - Function of Mission Epoch

——	Black body: $\alpha = 1$, $\epsilon = 1$
——	Silvered teflon: $\alpha = 0.07$, $\epsilon = 0.66$
——	Aluminised teflon: $\alpha = 0.13$, $\epsilon = 0.66$
——	White paint: $\alpha = 0.18$, $\epsilon = 0.92$
——	Black paint: $\alpha = 0.95$, $\epsilon = 0.89$
——	Aluminised kapton: $\alpha = 0.38$, $\epsilon = 0.67$
——	Bare aluminum: $\alpha = 0.13$, $\epsilon = 0.06$

Note that for this analysis only the spacecraft side facing the Sun has been taken into account, thus the temperature ranges in Table 4.15 are only for the light side. The shadow side typically has very low temperatures, far below freezing point. Conduction between the light and shadow side of the spacecraft plays an important role for the TCS. However, for this first iteration analysis, it is assumed that the whole spacecraft has an equal temperature and no conduction takes place to facilitate the analysis. Examples of typical thermal requirements for some spacecraft components can be seen in Table 4.16, in order to assess what type of coating is necessary.

Table 4.16: Typical Thermal Temperature Ranges [^{o}C] [43]

	Operational	Survival
Batteries	0 to 15	-10 to 25
Reaction wheels	-10 to 40	-20 to 50
IMUs	0 to 40	-10 to 50
Star trackers	0 to 30	-10 to 40
Antennas	-100 to 100	-120 to 120
Solar panels	-150 to 110	-200 to 130

Based on these results, it can be seen that using passive cooling exclusively would not be enough for this mission to ensure full thermal control of the spacecraft. Consider the batteries for example, which is the component in Table 4.16 with the smallest range of survival temperatures. Black paint would be the best option for this component, from the analysed coatings, but the coating would still not ensure survival as the maximum temperature during this mission using this coating is estimated to be 35.8370 ^{o}C while the maximum survival temperature is 25 ^{o}C.

Now that this analysis has been done, some requirements concerning the TCS can be identified before discussing some design considerations. The requirements can be seen in Table 4.17, where the identifier TCS stands for Thermal Control System.

Table 4.17: Thermal Control System Requirements

Identifier	Requirement
MFM-TCS-01	The thermal control system shall guarantee that the spacecraft can withstand the space environment between 0.8402 and 1.005 AU.
MFM-TCS-02	The thermal control system shall consist of both passive and active cooling.

In general, internal coatings with a low emissivity are used to insulate sensitive subsystems while high emissivity coatings are used to make temperatures more uniform. On the exterior white paint is generally used for parts facing the Sun, and black paint otherwise. To avoid temperature drops of certain external components, coatings with a high solar absorptivity are used if the components are facing the Sun, or coatings with a low emissivity otherwise.

Cooling of the bus can be achieved using conventional techniques, such as radiators, interface fillers, black paint and Multi Layer Insulation (MLI). Electrical heaters can also be installed in order to prevent excessive cooling of certain components during the cold phases of the mission. Conduction can furthermore be used primarily to cool components, which can be improved by the use of interface fillers. Black paint can be used on internal units and sidewalls in order to homogenise the temperature of cavities. The internal propulsion system can be insulated from the bus cavities by applying MLI, while the external propulsion components, such as thrusters, can require an individual heating system to keep them in their respective temperature ranges. This mission's need for very accurate pointing means a high thermal stability for the navigation components has to be guaranteed, especially the camera and the star tracker, in order to minimise errors caused by thermo-elastic distortions. In order to optimise the thermal control of the star tracker, it can be decoupled from the bus using a CFRP (Carbon Fibre Reinforced Polymer), which has a small conductivity. The camera can be covered with MLI, but parts may be left uncovered in order to aid cooling of the structure and CCD, if needed. The critical optical components can however be fitted with heaters in order to maintain the temperature above the rest of the structure during the very early stages of the mission.

4.9. Power

Now that most components have been identified, spread over the various subsystems, a first estimate of the power budget can be seen in Table 4.18. All numbers are based on components that have been found for similar missions. The power needed for the instrument comes primarily from cooling needs. The DST and EPC consume between 5% and 100% of their max power throughout the entire mission, depending on the mission phase and spacecraft mode, a consumption of 50% is assumed for the average power. The antenna is also assumed to have a 50% power consumption on average throughout the mission. The thrusters are only used in short pulses, and therefore have a very low average consumption. Note that in this budget the propulsion system is assumed to be a chemical one for simplicity. In case an electric propulsion system is chosen, both the peak and average power needed will be significantly higher. The consumption of both the CDMU and camera controller is assumed to be 50% on average. The RTU has a 50% duty cycle, which is why this component has an average power that consists of 50% of the max power. The GNC components have a 100% duty cycle, and their average power thus matches the max power. The thermal heaters are estimated to be 5% of the average total power, while the losses are assumed to be roughly 10%. The PCDU is the Power Conditioning and Distribution Unit (PCDU), which is responsible for regulating the power from the batteries and solar arrays to the rest of the spacecraft. The PCDU proposed for this mission will contain at least an array regular, a charge regulator and a discharge regulator.

Table 4.18: Spacecraft Power Budget

Subsystem	Element	Peak Power [W]	Average Power [W]
Instruments	Data Processing Unit	35	7
Communication	DST	35	17.5
	EPC	70	35
	Antenna	15	7.5
Propulsion	Thruster	100	5
Data Handling	CDMU	35	17.5
	RTU	25	12.5
	Camera Controller	25	12.5
GNC	Sun Sensor	0.8	0.8
	IMU	24	24
	Star Tracker	11	11
Thermal	Heaters	9	9
PCDU	Losses	20	20
Totals		404.8	179.3
System Margin	20%	80.96	35.86
Total Power		485.76	215.16

The main requirements for the power system can now be identified. These can be seen in Table 4.19, where the identifier PWR stands for power.

Table 4.19: Power System Requirements

Identifier	Requirement
MFM-PWR-01	The power system shall be able to power the spacecraft during all phases after orbit insertion, and in all modes, except hibernation.
MFM-PWR-02	The power system shall be able to provide a peak power of 485.76 W.
MFM-PWR-03	The power system shall be able to provide an average power of 215.16 W.

Now that the requirements have been established, some design considerations can follow. Based on the requirements, simple calculations will be performed to estimate the solar array size. It can be assumed that the spacecraft consumes the estimated average power in general. However, during some phases, especially the TCMs when the propulsion system is active and the flyby phase when the camera is fully active, the estimated peak power could be consumed. It usually never occurs that all systems are 100% active at the same time, meaning the actual peak power will in reality be lower than the one estimated here. As a very conservative starting point, the peak power of Table 4.18 will be used for the remainder of this thesis. However, an analysis to be completed in a next design step would be to analyse the peak power for each spacecraft mode discussed in Section 4.1 in order to find a more realistic peak power value.

As a first iteration design, the solar arrays are sized for the average power. During peak power, it is assumed that the batteries can provide the necessary additional power. The epoch when the spacecraft is the furthest away from the Sun is considered for this analysis, as this is the worst case scenario. The solar flux available at that epoch is then used to do basic solar array sizing calculations. Recall from Table 4.13 that the minimum distance to the Sun during this mission is 0.8042 AU and the solar flux at that time is 1353.2943 W/m^2. Gallium arsenide (GaAs) solar panels with an efficiency of 30% at mission start are assumed, with a degradation of 1% per year. Since the mission duration will be about 2.5 years, the efficiency at EoL will be roughly 29.3%. The coverage ratio is assumed to be 90%, and the internal losses are estimated to be 10%. By dividing the maximum needed power by the solar flux multiplied by all the efficiencies, the solar array minimum area can be estimated. This is done both for the peak power and the average power, to show the difference, see Figure 4.17. No additional system margin has been applied, since the 20% system margin on the power budget also directly affects the solar array sizing.
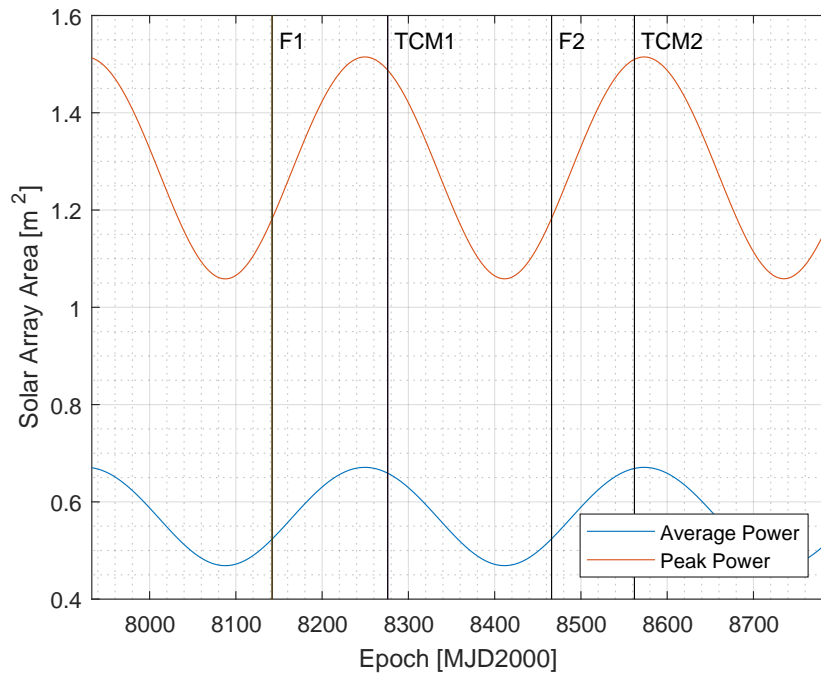
Figure 4.17: Minimum Required Solar Array Area

As can be seen, the minimum required solar array area at the most critical epoch is 0.6709 m^2. Assuming a panel density of 4 kg/m^2, a recurring value in internal ESA studies that use GaAs solar panels, the mass of the solar array will be 3.2204 kg.

Li-ion batteries can provide a good power to mass ratio for spacecraft and could be a viable option for this power subsystem. Due to the short mission duration, the depth of discharge can be high and the EoL degradation low. Batteries will be used both during eclipse periods, which are expected to be low due to the relatively short flyby duration, and for scenarios where the power exceeds the average power consumption. In order to do a simple first iteration design for the battery, the science phase is considered, since it is expected this phase has the highest battery storage capability need of the mission. It is assumed that during this phase all subsystems are active, with the exception of the propulsion system, since the spacecraft pointing will be achieved with the reaction wheels. If however reaction wheels desaturation using the thrusters will be take place during the science phase, this could be done relatively quickly which means there is no need to consider the power needed for the propulsion system for this simple analysis. Considering the power of the propulsion system at peak power was assumed to be 100 W, recall Table 4.18, the peak power requirement is 485.76, recall MFM-PWR-02 in Table 4.19, and the average power is 215.16 W, recall MFM-PWR-03 in Table 4.19, the power the batteries will have to provide during science phaes will be 170.6 W. At the beginning of Subsection 3.4.2 it was mentioned the science phase for the Apophis trajectory will be 928.8 minutes, or 15.48 hours. The minimum storage capability is then 2640.89 Wh, however, when considering a depth of discharge of 80%, which is a typical value for Li-ion batteries [54], the total storage capability of the batteries will be 3301.11 Wh. It is assumed the specific energy density of Li-ion batteries is 200 Wh/kg [54], meaning the battery mass will be 16.51 kg. It should be noted that the battery mass could be lower, since in reality not all subsystems would be working at max power during the entire science phase. The proposed battery with a capacity of 3301.11 Wh can provide the needed average power of 215.16 W for a duration of 12.27 hours, considering a depth of discharge of 80%. Since eclipse times will be much shorter than 12.27 hours, the batteries will be sufficient to power the spacecraft during eclipse.

The components for the power subsystem have been identified, and a simple architecture can be visualised, see Figure 4.18. During science and peak power scenarios, power will come both from the solar panels and from the battery while no charging will occur, see the blue links in the figure. During eclipse, the batteries will be in charge of powering the spacecraft, which is shown with the green links in the figure. Lastly, when batteries are charged the solar array alone will provide power to the spacecraft, shown with the red links in the figure.
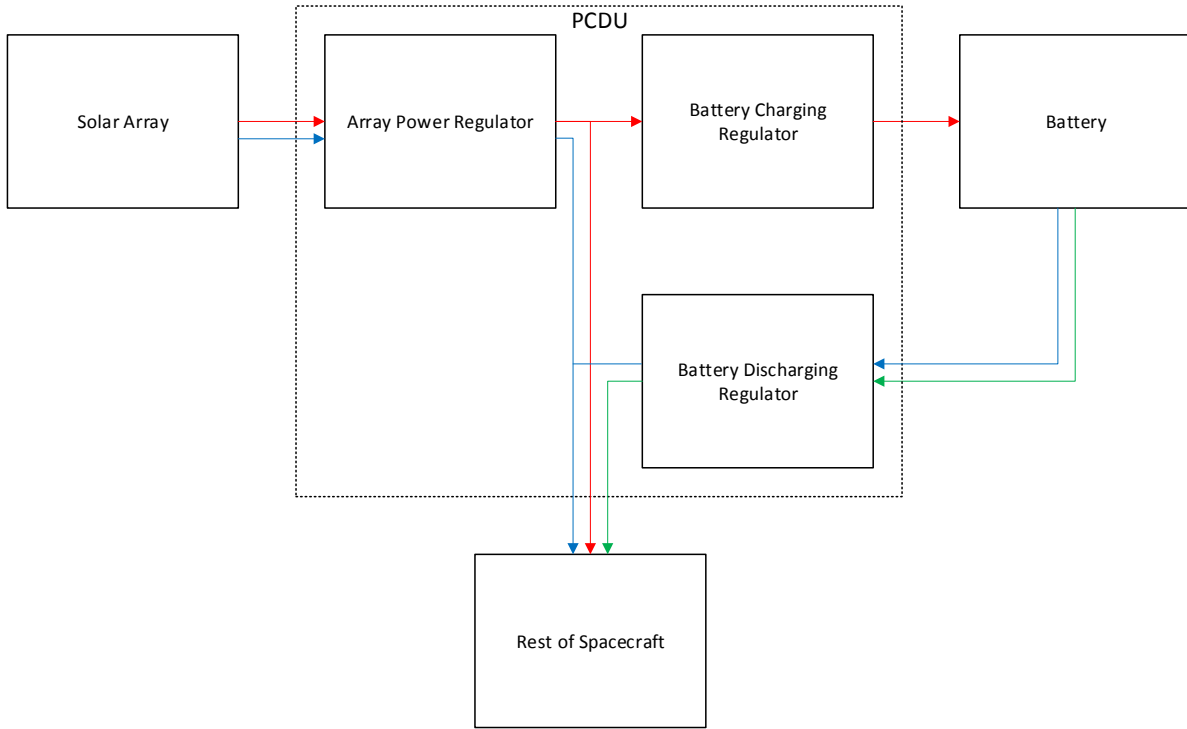
Figure 4.18: Power Subsystem Architecture

4.10. Mass Budget

All subsystems have been discussed, and the most important components have been identified. The next step is to estimate the total mass of the spacecraft. The mass budget can be seen in Table 4.20, where "wm" stands for "with margin".

Table 4.20: Spacecraft Mass Budget

Subsystem	Component	Amount	Unit mass [kg]	Total mass [kg]	Margin [%]	Margin [kg]	Mass wm [kg]	Subsystem wm [kg]	Mass fraction [%]
Structure		1	10.50	10.50	20%	2.10	12.60	12.60	0.10
TCS		1	3.50	3.50	20%	0.70	4.20	4.20	0.03
TT&C	DST	2	1.50	3.00	20%	0.60	3.60		
	TWTA	2	1.50	3.00	10%	0.30	3.30		
	RFDN	1	4.00	4.00	5%	0.20	4.20	14.58	0.12
	LGA	2	0.80	1.60	5%	0.08	1.68		
	HGA	1	1.50	1.50	20%	0.30	1.80		
DHS	CDMU	1	5.00	5.00	5%	0.25	5.25		
	RTU	1	8.10	8.10	10%	0.81	8.91	16.25	0.13
	Camera controller	1	1.90	1.90	10%	0.19	2.09		
GNC	Sun Sensor	4	0.30	1.20	5%	0.06	1.26		
	IMU	2	0.50	1.00	5%	0.05	1.05	23.10	0.19
	Star tracker	1	5.00	5.00	5%	0.25	5.25		
	Reaction Wheel	4	3.70	14.80	5%	0.74	15.54		
Propulsion	Thruster	8	0.30	2.40	20%	0.48	2.88		
	Tank	1	5.00	5.00	20%	1.00	6.00	14.28	0.11
	Pipes	1	2.00	2.00	20%	0.40	2.40		
	Misc	1	2.50	2.50	20%	0.50	3.00		
Power	Solar Array	1	6.03	6.03	20%	1.21	7.24		
	Battery	1	16.51	16.51	5%	0.83	17.33	27.72	0.22
	PCDU	1	3.00	3.00	5%	0.15	3.15		
Harness		1	6.00	6.00	5%	0.30	6.30	6.30	0.05
Instruments	Camera	1	5.50	5.50	5%	0.28	5.78	5.78	0.05
Totals				113.04		11.77	124.81		
System margin					20%		24.96		
Total dry mass							149.77		

All components present in the mass budget have been discussed earlier in this chapter, except the structure and harness masses, which have been estimated to be roughly 10% and 5% of the total dry mass without margin, respectively. All margins used in the budget are in accordance with ESA's margin philosophy for science studies [55], which consists of: 20% system margin on the nominal dry

mass at launch, a 5% margin on off-the-shelf items without the need of modifications, a 10% margin on off-the-shelf items that require minor modifications and a 20% margin on newly designed or developed items. As can be seen, the estimated spacecraft mass is estimated to be 149.77 kg, which meets requirement MFM-CFG-01 in Table 4.2. Note that the battery margin is only 5% since a system margin of 20% was already incorporated in the power budget, which has been used for the battery mass calculations. Furthermore, the propellant mass is not taken into consideration for this mass budget, which means it is not trivial to incorporate the propellant tank mass in the budget, as this is often a function of the propellant mass. A value of 5 kg has been used for the tank mass, based on the tank mass of similar internal ESA studies.

4.11. Platform

Now that all subsystems have been analysed and the power and mass budgets have been completed, a survey is performed in order to see whether there is an available platform that is compatible with this mission. Using an existing platform would facilitate the design process, since most subsystems are usually already included in an available platform. Existing platforms for small satellites, which are in the range of 100 to 500 kg, have been researched. Possible existing platforms and their technical details can be seen in Table 4.21. Data that was not found for this table has been left empty. Recall from Section 4.3 that the only payload considered for this analysis is a camera with a mass of 5.5 kg.

Table 4.21: Possible Platforms

Platform	Size [mm]	Payload Mass [kg]	Average Payload Power [W]
AF Adlershof TET-1	$670 \times 580 \times 880$	50	
BST LEOS-50	$600 \times 600 \times 300$	50	20
DEFIANT	$300 \times 300 \times 400$	5-10	65
InnoSat	$600 \times 650 \times 850$	25	40
MAC-100		50	65
S-50	$340 \times 340 \times 660$	20	26
SLI SCOUT	$400 \times 460 \times 840$	55	95
SSTL-100	$664 \times 632 \times 691$	15	24
Proteus	$1000 \times 1000 \times 1000$		

From this list, the SSTL-100 is arguably the best option for this mission because of the specified payload mass and power. The other options have somewhat excessive performance for this mission. Furthermore, the SSTL platforms are flight proven: the SSTL-100 in particular has been used in 15 successful missions, which all had a mass between 90 and 200 kg. The SSTL-100, that costs 11 M$, can be seen in Figure 4.19.
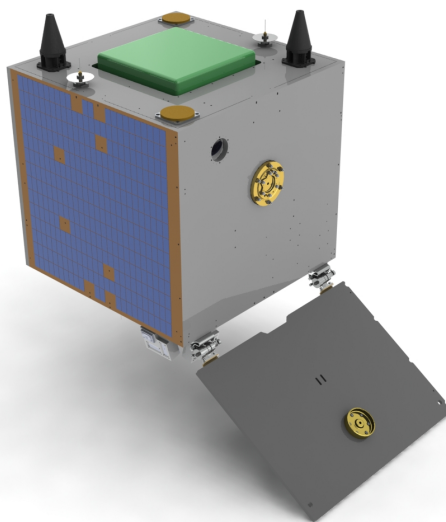
Figure 4.19: SSTL-100 Platform[9]

The placement of the solar panels could be a potential problem. The spacecraft is a box with body mounted solar panels on three sides and a deployable solar array on the fourth side. This obviously means that it is not possible to have all solar panels directly facing towards the Sun at all times, meaning power generation could be lower than when using a spacecraft with solar panels that extend from the body, such as the Proteus platform, see Figure 4.20.
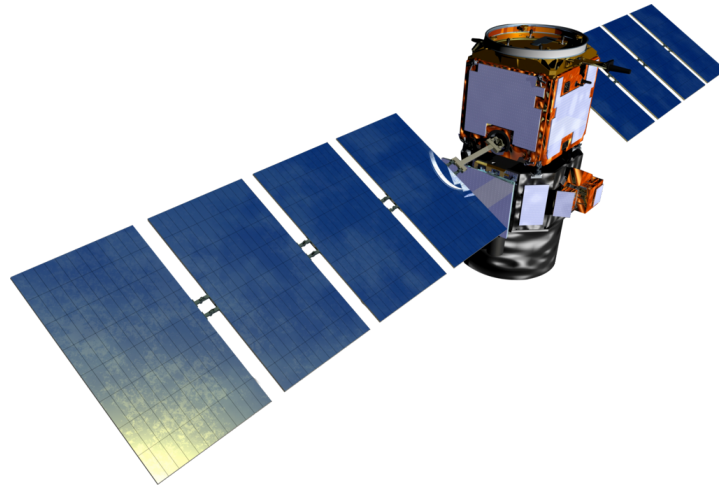
Figure 4.20: CALIPSO Spacecraft with Proteus Platform[10]

The SSTL-100 platform can accommodate a payload with an average power of 24 W, with peak power of 48 W. The baseline camera will be well within this power constraint. The SSTL-100 has three body mounted solar arrays and 1 deployable solar array. The body mounted arrays consist of single junction GaAs cells with a total area of 1.08 m^2, while the deployable solar array has triple junction GaAs cells with an area of 0.36 m^2. The estimated needed solar array area in Section 4.9 was 0.6709 m^2, which means this platform is expected to meet the power requirements of Table 4.19. The bus furthermore has a cold gas propulsion system with liquefied butane gas as the propellant. It can provide up to 20 m/s dV, which would be enough for the TCMs for this mission, according to the calculations in Section 4.4, which means it is expected to meet the propulsion requirements of Table 4.9. Lastly, the SSTL-100 bus is compatible with, among others, Vega, Dnepr and ROCKOT launchers, which are the ones researched for this thesis. The SSTL-100 could thus be a viable solution for this mission's purpose.

4.12. Recapitulation of Requirements

The requirements and design considerations for all subsystems have been discussed in Sections 4.2 through 4.11. A recapitulation of all the requirements, including a few additional requirements that arose after identifying necessary design considerations, is given in Table 4.22. The section where the requirement was introduced is also mentioned in this table. Recall the following abbreviations have been used for the identifiers: MFM for multi-flyby mission, LNC for launch, CFG for configuration, PLD for payload, GNC for Guidance, Navigation and Control, DHS for Data Handling System, COM for telecommunications, TCS for Thermal Control System, PWR for power and PRP for propulsion.

Table 4.22: Recapitulation of Requirements

Identifier	Requirement	Section
MFM-MIS-01	The mission shall provide optical measurement data during at least two flybys to asteroid Apophis.	4.1
MFM-MIS-02	The mission cost shall be less than 100 M€, including launch and operations.	4.1
MFM-MIS-03	The spacecraft shall have a mission lifetime of at least 2.5 years.	4.1
MFM-MIS-04	The spacecraft configuration shall be compatible with a Vega, or similar, launch vehicle.	New

---

[9]http://www.sst-us.com/shop/satellite-platforms/nasa-rapid-iii-sstl-100-15kg-24w, accessed 23-10-2018
[10]https://calipso.cnes.fr/en/CALIPSO/, accessed 24-10-2018

MFM-LNC-01	The launcher shall be able to bring the full spacecraft configuration in LEO.	New
MFM-CFG-01	The spacecraft shall have a dry mass less than 150 kg.	4.2
MFM-CFG-02	The complete spacecraft configuration wet mass shall be less than 2.4 tonnes.	New
MFM-CFG-03	The spacecraft shall have an upper stage to escape Earth from LEO.	New
MFM-PLD-01	The spacecraft shall have an optical camera as the main science instrument.	4.3
MFM-PLD-02	The science camera shall be used in combination with GNC equipment for navigation.	4.3
MFM-PRP-01	The propulsion system shall be able to perform at least two TCMs.	4.4
MFM-PRP-02	The propulsion system shall be able to desaturase the reaction wheels.	4.4
MFM-GNC-01	The GNC system shall be able to navigate the spacecraft autonomously.	4.5
MFM-GNC-02	The GNC system shall be able to provide a slew rate of 0.83 deg/s.	4.5
MFM-GNC-03	The GNC system shall be used to three-axis stabilise the spacecraft.	4.5
MFM-DHS-01	The DHS shall be able to monitor all spacecraft sensors.	4.6
MFM-DHS-02	The DHS shall be able to control all spacecraft actuators.	4.6
MFM-DHS-03	The DHS shall be able to interpret ground commands.	4.6
MFM-COM-01	The TT&C system shall be able to communicate with ESTRACK DSAs.	4.7
MFM-COM-02	The DSTs shall use X-band for uplink and downlink.	4.7
MFM-COM-03	The TT&C system shall provide a data rate of at least 1.5 kbps at maximum Earth distance.	4.7
MFM-TCS-01	The thermal control system shall guarantee that the spacecraft can withstand the space environment between 0.8402 and 1.005 AU.	4.8
MFM-TCS-02	The thermal control system shall consist of both passive and active cooling.	4.8
MFM-PWR-01	The power system shall be able to power the spacecraft during all phases, after orbit insertion, and in all modes, except hibernation.	4.9
MFM-PWR-02	The power system shall be able to provide a peak power of 485.76 W.	4.9
MFM-PWR-03	The power system shall be able to provide an average power of 215.16 W.	4.9
MFM-PWR-04	The solar arrays shall be able to generate the needed average power when the spacecraft is not in eclipse.	New
MFM-PWR-04	The battery shall be able to power the spacecraft during eclipse.	New
MFM-PWR-05	The battery shall be able to provide the necessary additional power during peak power scenarios.	New

To conclude this chapter, a brief summary will be given of the spacecraft analysis for this asteroid multi-flyby mission. The main instrument is an optical camera with a FoV of 0.5 degrees to ensure a resolution of 5 meters during the flyby phase. A light launcher such as Vega could get the spacecraft to low Earth orbit, while an upper stage such as STAR 48 can then be used to escape Earth and be injected into the desired interplanetary trajectory. In terms of spacecraft propulsion, three feasible options have been found: an ion thruster using xenon, a hydrazine mono-propellant system and a cold gas system using butane. The cold gas system is favoured due to its simplicity and low propellant needs for this particular mission, in the order of 0.2 kg. The combination of four reaction wheels, four Sun sensors, two IMUs and a star tracker would ensure that the necessary GNC tasks of this mission can be completed successfully, in particular the needed slew rate of 0.835 degrees per second during the close encounter with the asteroid. In order to communicate with Earth, X-band will be used. Two X-band DSTs will ensure a 1.5 kbps visibility at maximum distance. The HGA for communication with Earth will have a maximum diameter of 1 meter. A thermal control system with both passive and active cooling is required in order to make sure the spacecraft components work properly at distances ranging from roughly 0.84 to 1 AU. The power system needs to be able to generate an average power of 215.16 W. In order to do this, GaAs solar panels with an area of 0.6709 m^2 will be installed, in combination with a Li-ion batteries with a total storage capability of 3301.11 Wh. This configuration will ensure a spacecraft dry mass of 149.77 kg, excluding the STAR 48 upper stage. The SSTL-100 platform could be a potential option for this spacecraft. The design considerations mentioned here meet all the requirements listed in Table 4.22.

Conclusions and Future Work

This thesis has analysed the feasibility of an asteroid multi-flyby mission. This has been done from an astrodynamics point of view and a systems engineering one. Asteroid Apophis has been selected as the main research target due to its extremely close expected Earth encounter on April 13th, 2029: the expected miss distance is 38440 km, as was seen in Table 2.1. Backup targets, in order to compare results to Apophis, have been chosen to be 2001 WN5 and 2012 UE34. The high-fidelity 1:1 resonant trajectories that have been generated for Apophis and UE34 are near-circular and mostly around 1 AU, as can be seen in Figures 2.9 and 2.13, respectively. The trajectory to WN5 on the other hand is highly elliptical and expands to as much as 2 AU, recall Figure 2.14. The relative flyby velocities at the close approach for the generated trajectories are 8.73 km/s, 5.54 km/s and 13.46 km/s, respectively, as was seen in Tables 2.8 and 2.10.

These trajectories have then been used as inputs for the covariance analysis, where three cases have been analysed: the effects of the B-plane flyby geometry, the effect of several input parameters, and the effect of the asteroid target. The first case revealed that for this particular trajectory the results are independent of the flyby geometry, as became clear from Figure 3.15. From Figure 3.14 it was analysed that after a first flyby the knowledge improves significantly, but tends to converge back to its original knowledge after some time. After the second flyby, the orbital period can be estimated accurately due to having two independent measurements, which causes a big additional improvement in knowledge. A third flyby does not provide much additional knowledge. The reason for this is that no other new parameter that would cause a big knowledge improvement, such as the orbital period for the second flyby, can be accurately estimated after any flyby beyond the second. From this it can be concluded that for this target two flybys are needed to fulfil the task of improving the asteroid uncertainty. The position knowledge improves roughly 2 orders of magnitude, while the knowledge of the asteroid in the Earth B-plane at the expected impact date improves by roughly 3 orders of magnitude, as was seen in Figure 3.14 and 3.16, respectively. The 1-σ error ellipse diameter shrinks from roughly 65000 km to roughly 15 km in two flybys, as was seen in Figure 3.18 and Table 3.6. The second case showed that radiometric measurements at fixed intervals are not needed throughout the entire mission duration, recall Figure 3.28. Furthermore, it has been found that the very first optical measurement carries the most information, irrespective of the distance to the asteroid when it is taken. Every additional measurements provides less information, but improves the position knowledge nonetheless, up to a cap, as was seen in Figure 3.22. This means that there is no need for optical measurements at exactly the closest approach point, in this case 600 km. Finally, it has been shown that the results discussed so far are valid for both Apophis and asteroid UE34, which have similar orbits, while the results to asteroid WN5 are very different, recall Figures 3.32a and 3.36, respectively. In Figure 3.33 it was seen that the UE34 error ellipse diameter shrinks from 7839195 km at mission start to 1650 km at mission end. From this it can be concluded that for asteroids that do not have a near-circular orbit around 1 AU a different approach has to be used to improve the orbital knowledge. These conclusions made is possible to answer the main research question for the astrodynamics part, which was *how can the knowledge of the uncertainty on the trajectory of an asteroid be improved by means of a multi-flyby mission to that asteroid?*

A spacecraft analysis has been performed to identify critical requirements and design considerations. In Section 4.2 it has been concluded that a feasible launch option is to use a light launcher, such as Vega, to launch the spacecraft to LEO, after which an upper stage, such as STAR 48, would be used to escape Earth's gravity and put the spacecraft in the desired interplanetary trajectory. Three propulsion systems have been analysed and all three have been found to be viable options for this spacecraft as Table 4.8 suggested: an ion thruster with xenon as propellant, a hydrazine mono-propellant system and a cold gas system with butane. The cold gas system only requires a velocity increment of 0.97 m/s, which can be accomplished with 0.1981 kg of butane. Beside performing the necessary TCMs, the propulsion system can be used to desaturase the reaction wheels, which need to reach a slew rate

of at least 0.835 degrees per second during the flyby phase in order to keep pointing accurately at the asteroid to take optical measurements, recall Figure 4.8. From Table 4.15 it was concluded that the thermal control system will need both active and passive thermal cooling to provide heat and cooling capabilities for all subsystems, to ensure survival of all spacecraft components in the space environment at distances ranging from roughly 0.84 to 1 AU from the Sun. In Section 4.9 it was concluded that GaAs solar panels with an area of 0.6709 m^2 can generate the necessary 215.16 W average power for the spacecraft. During peak power scenarios, where the peak power can go as high as 485.76 W, the additional power will be provided by Li-ion batteries with a storage capacity of 3301.11 Wh. The proposed high-level spacecraft design can be accomplished with a dry mass of 149.77 kg, excluding the mass of the upper stage, according to the mass budget in Table 4.20. Additionally, an existing feasible platform, such as the SSTL-100, can be used for this mission. The conclusions in this paragraph answer the main research question for the systems engineering part, which was *what are critical requirements and design considerations for an asteroid multi-flyby mission?*

Recall the main research question to be answered from the introduction: *what is the feasibility of a multi-flyby mission to a potentially Earth impacting asteroid in order to improve the knowledge of the Earth collision uncertainty of that asteroid?* The combination of all three major parts of this thesis; the trajectory analysis, the covariance analysis and the systems engineering research, showed a spacecraft and mission design that can greatly improve the Earth collision uncertainty of a potentially Earth impacting asteroid with two flybys. It can thus be concluded that such a mission is feasible.

There are many interesting future work applications for this thesis, in order to expand the research. Arguably one of the most important tasks for future work would be to expand the NGA model of this analysis. For this analysis, the NGAs are only applied to the spacecraft. An addition could be to also apply the NGAs to the asteroid and include the Yarkovsky effect, since this effect that primarily affects small bodies such as asteroids is expected to deteriorate the results to some extent. It is crucial to know by how much the knowledge would be deteriorated before flying such a mission. The NGA model itself can be improved as well, primarily to improve the computation needs, which are extremely high with the current implementation. An interesting additional case to study would be to have the flyby of the spacecraft with the asteroid at an asteroid position that is as close as possible to the expected asteroid position at Earth impact. This is expected to give the best results in terms of asteroid position knowledge at the expected impact epoch. The reason for this is that since this proposed 1:1 resonant flyby mission only performs optical measurements of the asteroid in the same point in space at every flyby, the asteroid position knowledge is known best at that particular position. Another case that could be studied is having flybys at different positions along the asteroid trajectory, which is expected to improve the orbital knowledge to a better extend. Since the WN5 case has shown to give different results than the Apophis and UE34 case, it could be very interesting to expand the research and apply a parametrisation to the covariance analysis to allow for target-independent assessment based on orbital and physical asteroid parameters. This would mean that results would be available for all asteroids without the need to run each asteroid case independently.

Finally, there are several lessons learned from this thesis, from which the most important ones will be briefly discussed. The first is rather trivial: when selecting potential asteroid targets, the orbits should be visualised as well to quickly understand whether it could be a good target. For the selection in this thesis this had not been done, and instead only parameters such as expected impact date and asteroid diameter had been considered. Therefore it became clear after results from the spacecraft trajectory optimisation that asteroid WN5 was a poor target for this study, which could have been known all along in case the orbit would have been visualised at an earlier stage. Another lesson learned that arose from the trajectory optimisation process is to avoid complex simulation tools when possible. GMAT is an extremely powerful program with many available options and built in functions, most of which were not needed for the trajectory optimisation simulations. The many hours invested in debugging this complex program, while only using a fraction of its capabilities, could have been spent more wisely on creating a much simpler tool. Furthermore, a lesson learned from the covariance analysis results is to diversify the analysis to a bigger extend. Many of the results turned out to be very similar, such as the analysis of the radiometric measurement interval effect. If many additional asteroid targets had been selected as study cases, rather than studying the effect of input parameters, there would have been much more diverse results that could have been studied and discussed.

References

[1] P. Schulte *et al.*, "The Chicxulub asteroid impact and mass extinction at the Cretaceous-Paleogene boundary," *Science*, vol. 327, pp. 1214–1218, 2010.

[2] S. Brusatte *et al.*, "The extinction of the dinosaurs," *Biological Reviews*, vol. 90, pp. 628–642, 2015.

[3] T. von Foerster, "Dinosaur extinction due to asteroid?," *Physics Today*, vol. 35, pp. 19–21, 1982.

[4] A. Accomazzo *et al.*, "Rosetta following a living comet," *Acta Astronautica*, vol. 126, pp. 190–198, 2016.

[5] A. Herique, J. Lasue, Y. Rogez, S. Zine, and W. Kofman, "Rosetta rendezvous and CONSERT operations in 2014: a chimeric surface model of 67p/churymov gerasimenko," *Planetary and Space Science*, vol. 67, pp. 84–91, 2012.

[6] B. Godard, F. Budnik, P. Muñoz, T. Morley, and V. Janarthanan, "Orbit determination of Rosetta around comet 67P-Churymov-Gerasimenko," in *Proceedings of the ISSFD Munich*, 2015.

[7] A. Accomazzo *et al.*, "Rosetta operations at the comet," *Acta Astronautica*, vol. 115, pp. 434–441, 2015.

[8] R. Schulz, "Rosetta - one comet rendezvous and two asteroid fly-bys," *Solar System Research*, vol. 43, pp. 343–352, 2009.

[9] M. Barthelemy *et al.*, "Rosetta: How to archive more than 10 years of mission," *Planetary and Space Science*, vol. 150, pp. 91–103, 2018.

[10] E. Perozzi, A. Rossi, and G. Valsecchi, "Basic targeting strategies for rendezvous and flyby missinos to the near-Earth asteroids," *Planetary and Space Science*, vol. 49, pp. 3–22, 2001.

[11] B. Sarli and Y. Tsuda, "Hayabusa 2 extension plan: asteroid selection and trajectory design," *Acta Astronautica*, vol. 138, pp. 225–232, 2017.

[12] T. G. on Organic Environments in the Solar System and N. R. Council, *Exploring Organic Environments in the Solar System*. National Academies Press, 2007.

[13] S. Bus and R. Binzel, "Phase ii of the small main-belt asteroid spectroscopic survey the observations," *Icarus*, vol. 158, p. 106145, 2002.

[14] N. R. Council, *Defending planet Earth - near-Earth-object surveys and hazard mitigation strategies*. National Academies Press, 2010.

[15] J. Desmars, D. Bancelin, D. Hestroffer, and W. Thuillot, "Statistical and numerical study of asteroid orbital uncertainty," *Astronomy & Astrophysics*, vol. 554, 2013.

[16] A. Harris, M. Boslough, C. Chapman, L. Drube, and P. Michel, "Asteroid impacts and modern civilization: Can we prevent a catastrophe?," *Asteroids*, vol. 4, pp. 835–854, 2015.

[17] J. Cano, M. Snchez, S. Cornara, and I. Carnelli, "Mission analysis for the Don Quijote phase-a study," in *Proceedings of the 20th International Symposium on Space Flight Dynamics*, 2007.

[18] M. A'Hearn, M. Belton, A. Delamere, and W. Blume, "Deep impact: A large-scale active experiment on a cometary nucleus," *Deep Impact Mission: Looking Beneath the Surface of a Cometary Nucleus*, pp. 1–21, 2005.

[19] E. Bowell, B. Hapke, D. Domingue, K. Lumme, J. Peltoniemi, and A. Harris, "Application of photometric models to asteroids," in *Asteroids II; Proceedings of the Conference*, pp. 524–556, 1989.

[20] A. Harris and A. Harris, "On the Revision of Radiometric Albedos and Diameters of Asteroids," *icarus*, vol. 126, pp. 450–454, 1997.

[21] J. Desmars, D. Bancelin, D. Hestroffer, and W. Thuillot, "Statistical analysis on the uncertainty of asteroid ephemerides," *Proceedings of the Annual Meeting of the French Society of Astronomy and Astrophysics*, pp. 639 – 642, 2011.

[22] E. Lancaster and R. Blanchard, "A unified form of Lambert's theorem," Tech. Rep. TN D-5368, NASA, 1969.

[23] R. Gooding, "A procedure for the solution of Lambert's orbital boundary-value problem," *Celestial Mechanics and Dynamical Astronomy*, vol. 48, pp. 145–165, 1990.

[24] H. Shen and P. Tsiotras, "Optimal two-impulse rendezvous between two circular orbits using multiple-revolution Lambert's solutions," in *Proceeding of the AIAA Guidance, Navigation, and Control Conference and Exhibit*, 2002.

[25] D. Cho, Y. Chung, and H. Bang, "Trajectory correction maneuver design using an improved B-plane targeting method," *Acta Astronautica*, vol. 72, pp. 47–61, 2012.

[26] T. (NASA GSFC), "General Mission Analysis Tool (GMAT) - User Guide - R2018a," 2018.

[27] T. (NASA GSFC), "General Mission Analysis Tool (GMAT) - Mathematical Speficiations - R2018a," 2018.

[28] P. Gill and E. Wong, "Sequential quadratic programming methods," in *Proceedings of the IMA workshop mixed-integer nonlinear optimization (algorithmic advances and applications), Minneapolis, November 2008*, vol. 154, pp. 147–224, 2012.

[29] W. Martens and M. Khan. Private conversation on 12-07-2018.

[30] N. Stastny and D. Geller, "Autonomous optica lnavigation at Jupiter: a linear covariance analysis," *Journal of Spacecraft and Rockets*, vol. 45, pp. 290 – 298, 2008.

[31] S. Bhaskaran, J. Riedel, S. Synnott, and T. Wang, "The Deep Space 1 autonomous navigation system - a post-flight analysis," in *Proceedings of the Astrodynamics Specialist Conference*, 2000.

[32] W. Martens. Private conversation on 27-04-2018.

[33] O. Montenbruck and E. Gill, *Satellite Orbits*. Springer, 2005.

[34] B. Tapley, B. Schutz, and G. Born, *Statistical Orbit Determination*. Elsevier Academic Press, 2004.

[35] W. Martens and A. Rocchi. Private conversation on 25-06-2018.

[36] W. Martens. Private conversation on 10-04-2018.

[37] M. Salzmann, "Some aspects of Kalman filtering," tech. rep., University of New Brunswick, 1988.

[38] G. Bierman, "A comparison of discrete linear filtering algorithms," in *Proceedings of the 1973 IEEE Aerospace and Electronic Systems Conference*, 1973.

[39] G. Bierman, *Factorization methods for discrete sequential estimation*. Academic Press, 1977.

[40] G. Bierman, "Sequential square root filtering and smoothing of discrete linear systems," *Automatica*, vol. 10, pp. 147–158, 1974.

[41] W. Martens. Private comments on draft of this literature study report on 24-05-2018.

[42] O. Montenbruck, T. van helleputte, R. Kroes, and E. Gill, "Reduced dynamic orbiter determination using GPS code and carrier measurements," *Aerospace Science and Technology*, vol. 9, pp. 261–271, 2005.

[43] W. Larson and J. Wertz, *Space mission analysis and design*. Microcosm Press, 3 ed., 2005.

[44] D. Krejci and P. Lozano, "Space propulsion technology for small spacecraft," *Proceedings of the IEEE*, vol. 106, pp. 362 – 378, 2018.

[45] A. Cervone, *Micro-propulsion course (AE4S07) reader*. Delft University of Technology, 2018.

[46] A. Hashem, "Design and testing of a cold gas system," in *Proceedings of the 4th International Spacecraft Propulsion Conference*, 2004.

[47] S. Benson, J. Riehl, and S. Oleson, "NEXT ion propulsion system configurations and performance for Saturn system exploration," in *Proceedings of the 43rd AIAA-ASME-SAE-ASEE Joint Propulsion Conference and Exhibit*, 2007.

[48] D. Gibbson and C. Underwood, "Low cost butane propulsion systems for small spacecraft," in *Proceedings of the 15th AIAA-USU Conference on Small Satellites*, 2001.

[49] G. Schmidt, M. Patterson, and S. Benson, "The NASA evolutionary xenon thruster NEXT: NASA's next step for u.s. deep space propulsion," in *Proceedings of the 59th International Astronautical Congress*, 2008.

[50] S. Nothnagel, Z. Bailey, P. Cunio, and J. Hoffman, "Development of a cold gas spacecraft emulator system for the TALARIS hopper," in *Proceedings of the AIAA Space 2010 Conference and Exposition*, 2010.

[51] ECSS Secretariat, "Space engineering - communications guidelines," Tech. Rep. ECSS-E-HB-50A, European Cooperation for Space Standardisation, 2008. Available online: http://ecss.nl/hbstms/ecss-e-hb-50a-communications-guidelines/, accessed 24-10-2018.

[52] ECSS Secretariat, "Space engineering - radio frequency and modulation," Tech. Rep. ECSS-E-ST-50-05C Rev. 2, European Cooperation for Space Standardisation, 2011. Available online: http://ecss.nl/standard/ecss-e-st-50-05c-rev2-radio-frequency-and-modulation-4-october-2011/, accessed 24-10-2018.

[53] ESOC, "Aim 3P: Asteroid impact mission - payload assessment - CDF study report," tech. rep., ESA, 2014. Available online: https://gsp.esa.int/documents/10180/0/Document%2Bupload%2Btest%2B1/9755a7e0-73d5-41d2-95c9-dd2b32dbda87, accessed 23-10-2018.

[54] R. Surampudi *et al.*, "Energy storage technologies for future planetary science missions," Tech. Rep. JPL D-101146, Jet Propulsion Laboratory, 2017.

[55] SRE-PA and D-TEC Staff, "Margin philosophy for science assessment studies," tech. rep., ESA, 2012. Available online: http://sci.esa.int/science-e/www/object/doc.cfm?fobjectid=55027, accessed 25-10-2018.

[56] M. Murison, *Partial derivatives of observables with respect to two-body orbital elements*. Available online: https://www.researchgate.net/publication/271214791_Partial_Derivatives_of_Observables_with_Respect_to_Two-Body_Orbital_Elements, accessed 25-10-2018, 2006.

[57] L. Prockter *et al.*, "The NEAR Shoemaker mission to asteroid 433 Eros," *Acta Astronautica*, vol. 51, pp. 491–500, 2002.

[58] A. Accomazzo *et al.*, "The first Rosetta asteroid flyby," *Acta Astronautica*, vol. 66, pp. 382–390, 2010.

[59] T. Morley and F. Budnik, "Rosetta navigation for the fly-by of asteroid 2867 Šteins," in *Proceedings of the ISSFD Toulouse*, 2009.

[60] M. Lauer, U. Herfort, D. Hocken, and S. Kielbassa, "Optical measurements for the flyby navigation of Rosetta at asteroid Steins," in *Proceedings of the ISSFD Toulouse*, 2009.

[61] A. Accomazzo, K. Wirth, S. Lodiot, M. Küppers, and G. Schwehm, "The flyby of rosetta at asteroid Šteins - mission and science operations," *Planetary and Space Science*, vol. 58, pp. 1058–1065, 2010.

[62] F. Preusker *et al.*, "The northern hemisphere of asteroid (21) Lutetia - topography and orthoimages frmo Rosetta OSIRIS NAC image data," *Planetary and Space Science*, vol. 66, pp. 54–63, 2012.

[63] M. A'Hearn *et al.*, "EPOXI at comet Hartley 2," *Science*, vol. 332, pp. 1396–1400, 2011.

[64] R. Nelson, M. Rayman, and H. Weaver, "The Deep Space 1 encounter with comet 19P/Borrelly," *Icarus*, vol. 167, pp. 1–3, 2004.

[65] D. Boice and R. Wegmann, "The Deep Space 1 encounter with comet 19P/Borrelly," *Advances in Space Research*, vol. 39, pp. 407–412, 2007.

[66] J. Oberst *et al.*, "A model for rotation and shape of asteroid 9969 Braille from ground-based observations and images obtained during the Deep Space 1 (ds1) flyby," *Icarus*, vol. 153, pp. 16–23, 2001.

[67] M. Rayman and P. Varghese, "The Deep Space 1 extended mission," *Acta Astronautica*, vol. 48, pp. 693–705, 2001.

[68] M. Rayman, "The Deep Space 1 extended mission: challenges in preparing for an encounter with comet Borrelly," *Acta Astronautica*, vol. 51, pp. 507–516, 2002.

[69] NASA, *Deep Space 1 asteroid flyby.* Press Kit, 1999.

[70] R. N. Jr. *et al.*, "Stardust imaging camera," *Journal of Geophysical Research*, vol. 108, 2003.

[71] R. N. Jr. *et al.*, "Phase curve and albedo of asteroid 5535 Annefrank," *Journal of Geophysical Research*, vol. 108, 2003.

[72] T. Duxbury *et al.*, "Asteroid 5535 Annefrank size, shape and orientation: Stardust first results," *Journal of Geophysical Research*, vol. 109, 2004.

[73] J. Hillier, J. Bauer, and B. Buratti, "Photometric modeling of asteroid 5535 Annefrank from Stardust observations," *Icarus*, vol. 211, pp. 546–552, 2011.

[74] P. Tsou *et al.*, "Stardust encounters comet 81P/Wild 2," *Journal of Geophysical Research*, vol. 109, 2004.

[75] K. Klaasen *et al.*, "Stardust-NExT NAVCAM calibration and performance," *Icarus*, vol. 222, pp. 436–452, 2013.

[76] NASA, *Stardust-NExT.* Press Kit, 2011.

[77] F. Morring, "New Horizons changes course for 2019 encounter," *Aerospace Daily & Defense Report*, vol. 254, p. 6, 2015.

[78] Y. Guo and R. Farquhar, "New Horizons Plut-Kuiper Belt mission: design and simulation of the Pluto-Charon encounter," *Acta Astronautica*, vol. 56, pp. 421–429, 2005.

[79] S. Stern, "The New Horizons Pluto Kuiper Belt mission: an overview with historical context," *Space Science Reviews*, vol. 140, pp. 3–21, 2008.

[80] G. Fountain *et al.*, "The New Horizons spacecraft," *Space Science Reviews*, vol. 140, pp. 23–47, 2008.

[81] C. Russell, *New Horizons - Reconnaissance of the Pluto-Charon system and the Kuiper Belt.* Springer, 2009.

[82] J. Veverka *et al.*, "Comet Nucleus Tour," *Acta Astronautica*, vol. 35, pp. 181–191, 1995.

[83] A. Cochran, "The Comet Nucleus Tour (CONTOUR)," *Earth, Moon and Planets*, vol. 89, pp. 289–300, 2002.

[84] L. McNutt *et al.*, "Near-Earth Asteroid Scout," in *Proceedings of the AIAA Space 2014 Conference and Exposition*, 2014.

[85] N. Bowles *et al.*, "CASTAway: an asteroid main belt tour and survey," *Advances in Space Research*, vol. Article in press, 2017.

[86] A. Gibbings *et al.*, "A deep space inventory tour of the main asteroid belt," in *Proceedings of the 67th International Astronautical Congress*, 2016.

[87] N. Wells, R. Walker, S. Green, and A. Ball, "SIMONE: interplanetary microsatellites for NEO rendezvous missions," *Acta Astronautica*, vol. 59, pp. 700–709, 2006.

[88] M. Ishiguro *et al.*, "The Hayabusa spacecraft asteroid multi-band imaging camera (AMICA)," *Icarus*, vol. 207, pp. 714–731, 2010.

[89] J. Kawaguchi, H. Kuninaka, A. Fujiwara, and T. Uesugis, "MUSES-C, its launch and early orbit operations," *Acta Astronautica*, vol. 59, pp. 669–678, 2006.

[90] J. Kawaguchi, A. Fujiwara, and T. Uesugi, "Hayabusa - its technology and science accomplishment summary and Hayabusa-2," *Acta Astronautica*, vol. 62, pp. 639–647, 2008.

[91] B. Sarli and Y. Tsuda, "Hayabusa 2 extension plan: asteroid selection and trajectory design," *Acta Astronautica*, vol. 138, pp. 225–232, 2017.

[92] Y. Tsuda, M. Yoshikawa, M. Abe, H. Minamino, and S. Nakazawa, "System design of the Hayabusa 2 - asteroid sample return missino to 1999 ju3," *Acta Astronautica*, vol. 91, pp. 356–362, 2013.

[93] T. Ajluni *et al.*, "OSIRIS-REx, returning the asteroid sample," in *Proceedings of the 2015 IEEE Aerospace Conference*, 2015.

[94] J. Gal-Edd and A. Cheuvront, "The OSIRIS-REx asteroid sample return mission operations design," in *Proceedings of the 2015 IEEE Aerospace Conference*, 2015.

[95] B. Rizk *et al.*, "OCAMS: the OSIRIS-REx Camera Suite," *Space Science Reviews*, vol. 214, 2018.

[96] C. Russell and C. Raymond, "The Dawn mission to Vesta and Ceres," *Space Science Reviews*, vol. 163, pp. 3–23, 2011.

[97] M. Rayman and R. Mase, "Dawn's exploration of Vesta," *Acta Astronautica*, vol. 94, pp. 159–167, 2014.

[98] H. Sierks *et al.*, "The Dawn framing camera," *Space Science Reviews*, vol. 163, pp. 263–327, 2011.

[99] NASA, *Dawn at Ceres.* Press Kit, 2015.

[100] P. Lord *et al.*, "Psyche: journey to a metal world," in *Proceedings of the 2017 IEEE Aerospace Conference*, 2017.

[101] L. Elkins-Tanton *et al.*, "Journey to a metal world: concept for a discovery mission to Psyche," in *Proceedings of 45th Lunar and Planetary Science Conference*, 2014.

[102] A. Cheng *et al.*, "Asteroid impact and deflection assessment mission," *Acta Astronautica*, vol. 115, pp. 262–269, 2015.

[103] P. Michel *et al.*, "Science case for the asteroid impact mission (AIM): a component of the asteroid impact & deflection assessment (AIDA) mission," *Advances in Space Research*, vol. 57, pp. 2529–2547, 2016.

[104] ESOC, "Asteroid impact mission: mission analysis guidelines," tech. rep., ESA, 2016.

[105] P. Michel *et al.*, "European component of the AIDA mission to a binary asteroid: characterization and interpretation of the impact of the DART mission," *Advances in Space Research*, vol. Article in press, 2017.

[106] R. Manghi, "Preliminary orbital analysis for a cubesat mission to the Didymos binary asteroid system," *Advances in Space Research*, vol. Article in press, 2017.

[107] R. Walker, D. Koschny, C. Bramanti, and E. C. S. Team, "M-argo: a stand-alone deep space cubesat system for low-cost science and exploration missions," in *Presentation at 6th Interplanetary CubeSat Workshop, Cambridge, UK*, 2017.

[108] ESOC, "M-argo internal cdf study report," tech. rep., ESA, 2017.

[109] C. Snodgrass *et al.*, "The Castalia mission to main belt comet 133P/Elst-Pizarro," *Advances in Space Research*, vol. Article in press, 2017.

[110] P. D'Arrigo, "The ISHTAR mission - executive summary for publication on esa web pages," tech. rep., Astrium Ltd, 2014.

[111] M. Barucci *et al.*, "The ISHTAR mission: probing the internal structure of NEOs," *Highlights of Astronomy*, vol. 13, pp. 738–742, 2005.

[112] P. D'Arrigo, M. Barucci, and C. Lagerkvist, "The ISHTAR mission," in *Proceedings of the ACM International Conference*, 2002.

[113] S. Wolters, A. Ball, N. Wells, C. Saunders, and N. McBride, "Measurement requirements for a near-Earth asteroid impact mitigation demonstration mission," *Planetary and Space Science*, vol. 59, pp. 1506–1515, 2011.

[114] I. Carnelli, A. Gàlvez, and D. Izzo, "Don Quijote: a NEO deflection precursor mission," in *Proceedings of the NASA Workshop on Near-Earth Object Detection, Characterization and Threat Mitigation*, 2006.

Appendices

<div align="right"><h1>A</h1></div>

<h1 align="center">Derivation of Transformations</h1>

The following transformation discussed in Section 3.1 is derived here:

$$\mathbf{R}_{CAM \to RADEC} = \mathbf{R}_{RADEC \to EME2000}^{T} \mathbf{R}_{CAM \to EME2000} \tag{A.1}$$

Taking following relation can furthermore be stated:

$$\vec{r}_{EME} = r \begin{bmatrix} \cos(\delta)\cos(\alpha) \\ \cos(\delta)\sin(\alpha) \\ \sin(\delta) \end{bmatrix} \tag{A.2}$$

Together with $\vec{r}$, $\hat{e}_{\alpha}$ and $\hat{e}_{\delta}$ form an orthogonal coordinate system. Now the derivation of $\mathbf{R}_{CAM \to EME2000}$ will be discussed. It can be stated as follows

$$\mathbf{R}_{CAM \to EME2000} = [\hat{X}_{CAM}, \hat{Y}_{CAM}, \hat{Z}_{CAM}] \tag{A.3}$$

The elements of this rotation matrix are essentially the CAM frame unit vectors expressed in EME2000. To evaluate this, first the distance from the spacecraft to the target is calculated, then this distance is normalised to find the unit vectors $\vec{e}_k$, which is simply $\hat{Z}_{CAM}$. Then define a vector $\vec{s}$ as the direction of the Sun as seen from the target, which thus is the vector pointing from the object towards the Sun. This can be computed by subtracting the object coordinates from the Sun coordinates, defined in the EME2000 frame. By evaluating the cross product $\vec{e} \times \vec{s}$ and normalising, this vector $\hat{Y}_{CAM}$ is obtained. Finally, $\hat{X}_{CAM}$ is obtained by evaluating the cross product $\hat{Y}_{CAM} \times \hat{Z}_{CAM}$ and the vector is again normalised. The rotation matrix can thus be written as

$$\mathbf{R}_{CAM \to EME2000} = \left[\frac{(\vec{e} \times \vec{s}) \times \vec{e}}{||(\vec{e} \times \vec{s}) \times \vec{e}||}, \frac{\vec{e} \times \vec{s}}{||\vec{e} \times \vec{s}||}, \vec{e} \right] \tag{A.4}$$

Discussed next is the rotation matrix from RADEC to the EME2000 frame, which can be stated as follows

$$\mathbf{R}_{RADEC \to EME2000} = [\hat{e}_{\alpha}, \hat{e}_{\delta}, \hat{r}] \tag{A.5}$$

The first element, before normalising, can be calculated as follows

$$\begin{aligned} \vec{e}_{\alpha} &= \frac{\partial \vec{X}_{EME}}{\partial \alpha} \hat{X}_{EME} + \frac{\partial \vec{Y}_{EME}}{\partial \alpha} \hat{Y}_{EME} + \frac{\partial \vec{Z}_{EME}}{\partial \alpha} \hat{Z}_{EME} \\ &= \begin{bmatrix} -\cos(\delta)\sin(\alpha) \\ \cos(\delta)\cos(\alpha) \\ 0 \end{bmatrix} \\ &= \hat{Z}_{EME} \times \hat{r} \end{aligned} \tag{A.6}$$

Which, after normalising, can be written as

$$\hat{e}_{\alpha} = \begin{bmatrix} -\sin(\alpha) \\ \cos(\alpha) \\ 0 \end{bmatrix} \tag{A.7}$$

The second element is calculated as follows

$$
\begin{aligned}
\vec{e}_\delta &= \frac{\partial \vec{X}_{EME}}{\partial \delta} \hat{X}_{EME} + \frac{\partial \vec{Y}_{EME}}{\partial \delta} \hat{Y}_{EME} + \frac{\partial \vec{Z}_{EME}}{\partial \delta} \hat{Z}_{EME} \\
&= r \begin{bmatrix} -\sin(\delta)\cos(\alpha) \\ -\sin(\delta)\sin(\alpha) \\ \cos(\delta) \end{bmatrix} \\
&= \hat{r} \times \hat{e}_\alpha
\end{aligned}
\tag{A.8}
$$

This expression is already normalised. The rotation matrix can thus be written as

$$
\mathbf{R}_{RADEC \to EME2000} = \begin{bmatrix} -\sin(\alpha) \\ \cos(\alpha) \\ 0 \end{bmatrix}, \hat{r} \times \begin{pmatrix} -\sin(\alpha) \\ \cos(\alpha) \\ 0 \end{pmatrix}, \hat{r} \end{bmatrix}
\tag{A.9}
$$

B

Derivation of Optical, Range and Doppler Partials

The **H** matrix, recall Equation (3.42), needs to be computed in order to use the SRIF. This matrix contains the partials of the measurements with respect to the estimation, consider and implicitly estimated parameters. The method to generate the partials for the consider covariance matrix ($\mathbf{H}_C$), the covariance matrix of the estimation parameters ($\mathbf{H}_E$), and the IEP covariance matrix ($\mathbf{H}_{IEP}$) is identical, so no distinction has to made there. On the other hand, a distinction is made between the generation of the partials needed for the optical measurements, and the partials needed for the range and Doppler measurements.

Starting with the partials of the optical measurements, the following expression for the partials can be set up:

$$\mathbf{H}_{ij} = \frac{\partial z_i(t_{meas})}{\partial \vec{x}_j(t_{sol})} \tag{B.1}$$

$$= \frac{\partial z_i(t_{meas})}{\partial \vec{x}_k(t_{meas})} \frac{\partial \vec{x}_k(t_{meas})}{\partial \vec{x}_j(t_{sol})} \tag{B.2}$$

In this equation, t_{meas} is the measurement epoch and t_{sol} is the solution epoch, while z_i are the optical measurements, thus right ascension (RA, α) and declination (DEC, δ) of the target, and $\vec{x}_j$ is the modelled state of the target and spacecraft. The first term in Equation (B.2) has to be calculated analytically and will be discussed in this section, while the second term equals $\mathbf{\Phi}(t_{meas}, t_{sol})$ and thus comes from the variational equations, discussed in Section 3.2.3. In the following derivation the following notations will be used, where the orientation of the SCI frame has been discussed in Section 3.1 and can be found in Table 3.1:

- $\vec{s}$: Spacecraft position vector at measurement epoch, in SCI frame
- $\vec{r}$: Target position vector at transmission epoch, in SCI frame
- $\hat{e}$: Unit vector of measurement direction, in SCI frame
- α, δ: Right ascension and declination of $\hat{e}$, respectively

So the partials that need to be calculated are:

$$\frac{\partial \alpha}{\partial \vec{s}} \quad \frac{\partial \delta}{\partial \vec{s}} \quad \frac{\partial \alpha}{\partial \vec{r}} \quad \frac{\partial \delta}{\partial \vec{r}}$$

Using the chain rule, these needed partials can be separated into the following partials (here subscripts i and k have been omitted for simplicity, but note that in fact every $\vec{r}$ and $\vec{s}$ should in fact be $\vec{r}_i$ and $\vec{s}_i$ while $\hat{e}$ is in fact $\hat{e}_k$):

$$\frac{\partial \alpha}{\partial \vec{s}} = \frac{\partial \alpha}{\partial \hat{e}} \frac{\partial \hat{e}}{\partial \vec{s}} \tag{B.3}$$

$$\frac{\partial \delta}{\partial \vec{s}} = \frac{\partial \delta}{\partial \hat{e}} \frac{\partial \hat{e}}{\partial \vec{s}} \tag{B.4}$$

$$\frac{\partial \alpha}{\partial \vec{r}} = \frac{\partial \alpha}{\partial \hat{e}} \frac{\partial \hat{e}}{\partial \vec{r}} \tag{B.5}$$

$$\frac{\partial \delta}{\partial \vec{r}} = \frac{\partial \delta}{\partial \hat{e}} \frac{\partial \hat{e}}{\partial \vec{r}} \tag{B.6}$$

From these equations it becomes clear that the partials that need to be derived are:

$$\frac{\partial \alpha}{\partial \hat{e}} \quad \frac{\partial \delta}{\partial \hat{e}} \quad \frac{\partial \hat{e}}{\partial \vec{s}} \quad \frac{\partial \hat{e}}{\partial \vec{r}}$$

Considering the Cartesian frame of Figure B.1, the following expressions for the right ascension and declination can be set up.
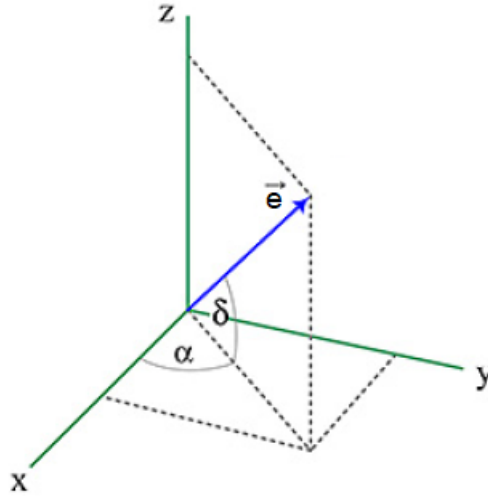
Figure B.1: Frame with $\hat{e}$, right ascension and declination [56]

$$\alpha = \tan_2^{-1}(e_y, e_x) \tag{B.7}$$

$$\delta = \tan_2^{-1}(e_z, \sqrt{e_x^2 + e_y^2}) \tag{B.8}$$

Note that in these equations, $\tan_2^{-1}$ is used instead of just the $\tan^{-1}$, as the correct quadrant needs to be found. Using the following expressions:

$$\frac{\partial \tan_2^{-1}(y, x)}{\partial x} = -\frac{y}{x^2 + y^2} \tag{B.9}$$

$$\frac{\partial \tan_2^{-1}(y, x)}{\partial y} = \frac{x}{x^2 + y^2} \tag{B.10}$$

the following partials can be found:

$$\frac{\partial \alpha}{\partial e_x} = -\frac{e_y}{e_x^2 + e_y^2} \tag{B.11}$$

$$\frac{\partial \alpha}{\partial e_y} = \frac{e_x}{e_x^2 + e_y^2} \tag{B.12}$$

$$\frac{\partial \alpha}{\partial e_z} = 0 \tag{B.13}$$

$$\frac{\partial \delta}{\partial e_x} = -\frac{e_x e_z}{(e_x^2 + e_y^2 + e_z^2)\sqrt{e_x^2 + e_y^2}} \tag{B.14}$$

$$\frac{\partial \delta}{\partial e_y} = -\frac{e_y e_z}{(e_x^2 + e_y^2 + e_z^2)\sqrt{e_x^2 + e_y^2}} \tag{B.15}$$

$$\frac{\partial \delta}{\partial e_z} = \frac{\sqrt{e_x^2 + e_y^2}}{e_x^2 + e_y^2 + e_z^2} \tag{B.16}$$

which concludes the derivation of the measurements with respect to the unit vectors ($\frac{\partial \alpha}{\partial \hat{e}}$ and $\frac{\partial \delta}{\partial \hat{e}}$). Next, the partial derivatives of $\hat{e}$ with respect to the spacecraft and target have to be found. These can be found using the following expression:

$$\frac{\partial}{\partial \vec{x}_i} \frac{\vec{x}_j}{||\vec{x}||} = \frac{\delta_{ij}}{||\vec{x}||} - \frac{\vec{x}_i \vec{x}_j}{||\vec{x}||^3} \tag{B.17}$$

This is needed because the unit vector $\hat{e}$ can be written as follows:

$$\hat{e}_k = \frac{\vec{r}_k - \vec{s}_k}{||\vec{r} - \vec{s}||} \tag{B.18}$$

By combining Equations (B.17) and (B.18), the following partials are found:

$$\frac{\partial \hat{e}_k}{\partial \vec{s}_i} = -\frac{\delta_{ik}}{||\vec{r} - \vec{s}||} + \frac{(\vec{r} - \vec{s})_i(\vec{r} - \vec{s})_k}{||\vec{r} - \vec{s}||^3} \tag{B.19}$$

$$\frac{\partial \hat{e}_k}{\partial \vec{r}_i} = \frac{\delta_{ik}}{||\vec{r} - \vec{s}||} - \frac{(\vec{r} - \vec{s})_i(\vec{r} - \vec{s})_k}{||\vec{r} - \vec{s}||^3} \tag{B.20}$$

An important assumption that is made here is that the light time can be ignored for the position of the target. This is a valid assumption considering the measurement distance will be 600 km the closest and a few 10,000 km the furthest (as will be shown in Section 3.4). Considering the speed of light is 299792.458 km/s, even at the furthest measurement distance the light time effects would be a fraction of a second, hence it is acceptable neglecting the effect. Partials $\frac{\partial \hat{e}}{\partial \vec{s}}$ and $\frac{\partial \hat{e}}{\partial \vec{r}}$ are now derived as well, and all relevant optical measurement partials have been discussed. Optionally, GALICOV can also calculate partials of α and δ with respect to the Image Processing (IP) bias model coefficients. This was used for the JUICE case, but since for this thesis the IP bias is not included in the estimated, considered or implicitly estimated parameters of the covariance analysis, as will become clear in Subsection 3.2.7, these partials are not implemented and the derivation of the partials will thus not be discussed.

Now that all the optical navigation partials have been discussed, the range and Doppler partials will follow. Since light-time effects are accounted for, as discussed in Subsection 3.2.2, the following three vector are defined:

- $\vec{s}_1$: Spacecraft state at t_1
- $\vec{r}_2$: Target (asteroid) state at t_2
- $\vec{s}_3$: Spacecraft state at t_3

Important to note is that t_1 and t_3 are taken in GS time while t_2 is taken in spacecraft time. The range r and range rate $\dot{r}$ can be set up as follows. Not to be confused are the target state vector $\vec{r}$ and the range scalar r.

$$r = ||\vec{r}_2 - \vec{s}_1|| + ||\vec{r}_2 - \vec{s}_3|| \tag{B.21}$$

$$\dot{r} = \frac{(\vec{r}_2 - \vec{s}_1)(\vec{r}_2 - \dot{\vec{s}}_1)}{||\vec{r}_2 - \vec{s}_1||} + \frac{(\vec{r}_2 - \vec{s}_3)(\vec{r}_2 - \dot{\vec{s}}_3)}{||\vec{r}_2 - \vec{s}_3||} \tag{B.22}$$

The partial of the range with respect to the spacecraft state can then be defined as follows, where the STM is part of the expression due to accounting for light-time effects, where $\partial\left(\vec{r}, \dot{\vec{r}}\right)_i$ is at t_3:

$$\frac{\partial r}{\partial\left(\vec{r}, \dot{\vec{r}}\right)_i} = \left[\frac{(\vec{r}_2 - \vec{s}_1)_j}{||\vec{r}_2 - \vec{s}_1||} + \frac{(\vec{r}_2 - \vec{s}_3)_j}{||\vec{r}_2 - \vec{s}_3||}\right] \mathbf{\Phi}_{sc,ji}(t_2, t_3) \tag{B.23}$$

Where $\mathbf{\Phi}_{sc,ji}(t_2, t_3)$ is a 3×6 block of the STM of the spacecraft, with i ranging from 1 to 6 and j from 1 to 3. The range rate partial can similarly be defined as, where $\partial\left(\vec{r}, \dot{\vec{r}}\right)_i$ is again at t_3:

$$\frac{\partial \dot{\vec{r}}}{\partial\left(\vec{r}, \dot{\vec{r}}\right)_i} = (\vec{A}_1 + \vec{A}_2, \vec{B}_1 + \vec{B}_2)_j \mathbf{\Phi}_{sc,ji}(t_2, t_3) \tag{B.24}$$

where $\vec{A}_{1j}$, $\vec{A}_{2j}$, $\vec{B}_{1j}$ and $\vec{B}_{2j}$ are all position vectors, defined as follows:

$$\vec{A}_{1j} = \frac{(\vec{r}_2 - \vec{s}_1)_j}{||\vec{r}_2 - \vec{s}_1||} - \frac{(\vec{r}_2 - \vec{s}_1)_j(\vec{r}_2 - \vec{s}_1)(\vec{r}_2 - \vec{s}_1)}{||\vec{r}_2 - \vec{s}_1||^3} \tag{B.25}$$

$$\vec{A}_{2j} = \frac{(\vec{r}_2 - \vec{s}_3)_j}{||\vec{r}_2 - \vec{s}_3||} - \frac{(\vec{r}_2 - \vec{s}_3)_j(\vec{r}_2 - \vec{s}_3)(\vec{r}_2 - \vec{s}_3)}{||\vec{r}_2 - \vec{s}_3||^3} \tag{B.26}$$

$$\vec{B}_{1j} = \frac{(\vec{r}_2 - \vec{s}_1)_j}{||\vec{r}_2 - \vec{s}_1||} \tag{B.27}$$

$$\vec{B}_{2j} = \frac{(\vec{r}_2 - \vec{s}_3)_j}{||\vec{r}_2 - \vec{s}_3||} \tag{B.28}$$

The partials needed for range and Doppler measurements with respect to the state vectors are now defined. Lastly, the partials of the radiometric measurements with respect to the GS are also derived. These are defined in the ECEF frame, as the ground station is fixed to the Earth. Then using the following expression:

$$\vec{s}_t = k_t \vec{s}_f \tag{B.29}$$

where the subscript f stands for fixed and subscript t denotes the time, the following partials can be derived

$$\frac{\partial r}{\partial \vec{s}_{f,i}} = -\frac{(\vec{r}_2 - \vec{s}_1)_j}{||\vec{r}_2 - \vec{s}_1||} k_{1,ji} - \frac{(\vec{r}_2 - \vec{s}_3)_j}{||\vec{r}_2 - \vec{s}_3||} k_{3,ji} \tag{B.30}$$

$$\frac{\partial \dot{r}}{\partial \vec{s}_{f,i}} = -\vec{A}_{1j} k_{1,ji} - \vec{B}_{1j} \dot{k}_{1,ji} - \vec{A}_{2j} k_{3,ji} - \vec{B}_{2j} \dot{k}_{3,ji} \tag{B.31}$$

where the expressions for $\vec{A}_{1j}$, $\vec{A}_{2j}$, $\vec{B}_{1j}$ and $\vec{B}_{2j}$ are the same as the ones defined in Equations (B.25) through (B.28).

C

Additional Galicov Figures

This appendix contains additional figures generated using GALICOV. The figures used for the phase 2 verification can be seen in Section C.1, while the galicov and INTNAV figures for the phase 3 verification are found in Section C.2. Sections C.3 and C.4 contain the additional figures used for asteroids UE34 and WN5, respectively.

C.1. Verification Phase 2

(a) Spacecraft
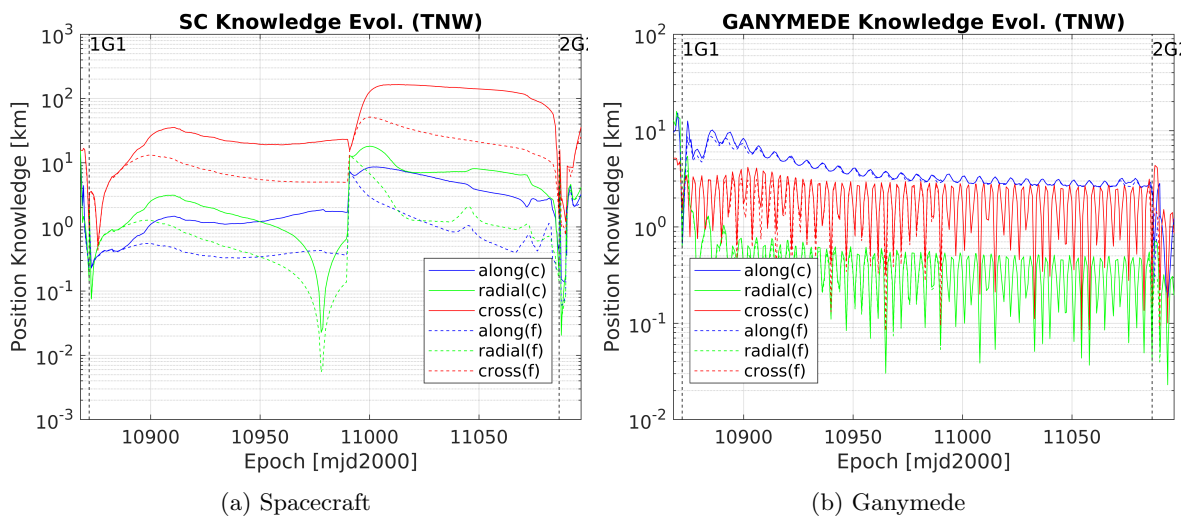
(b) Ganymede

Figure C.1: Position Knowledge - Original

(a) Spacecraft
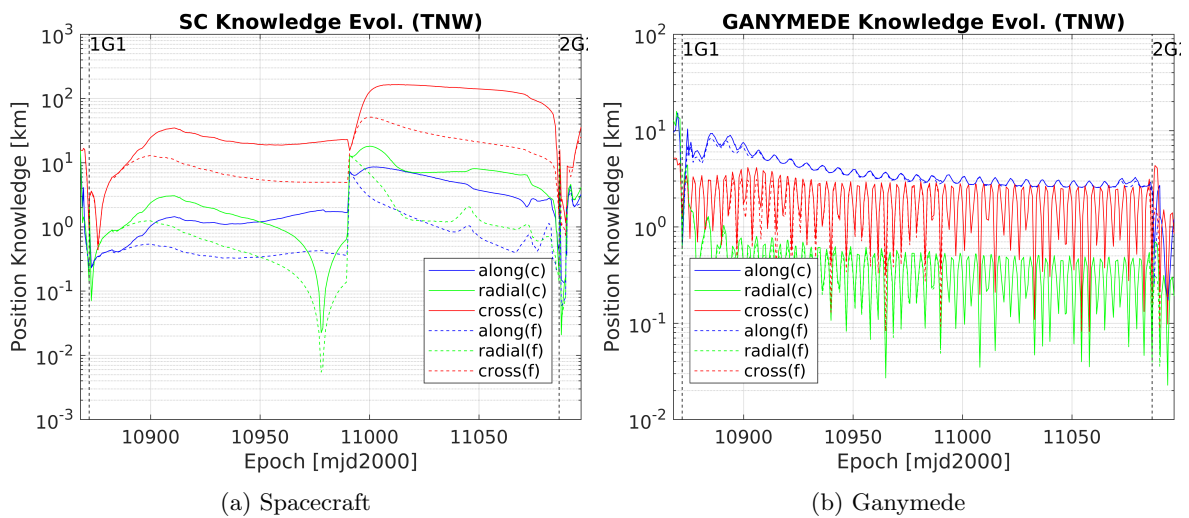
(b) Ganymede

Figure C.2: Position Knowledge - Without Io

(a) Spacecraft
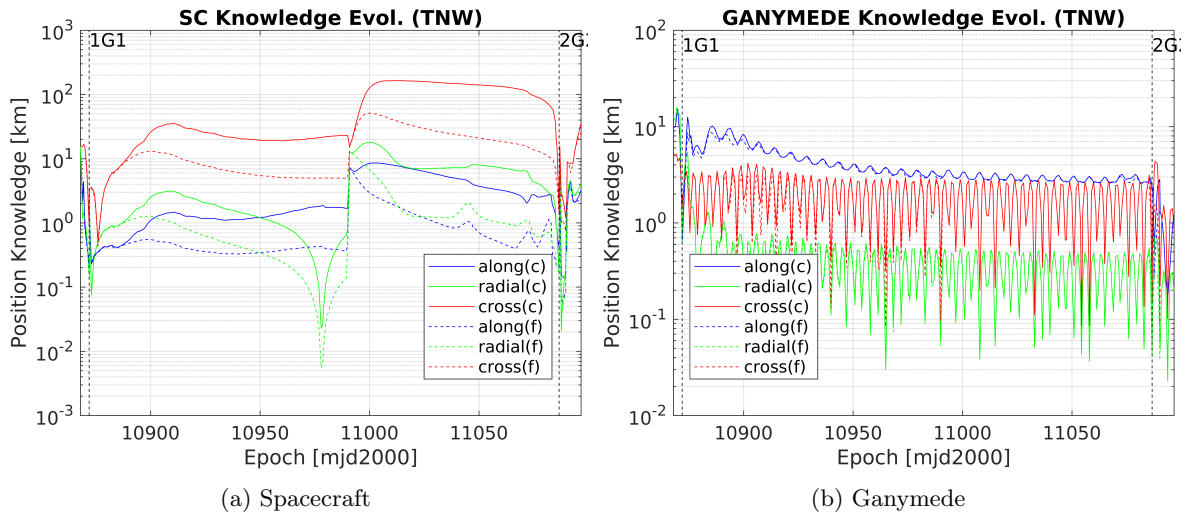
(b) Ganymede

Figure C.3: Position Knowledge - Only Ganymede

C.2. Verification Phase 3

(a) GALICOV

(b) INTNAV
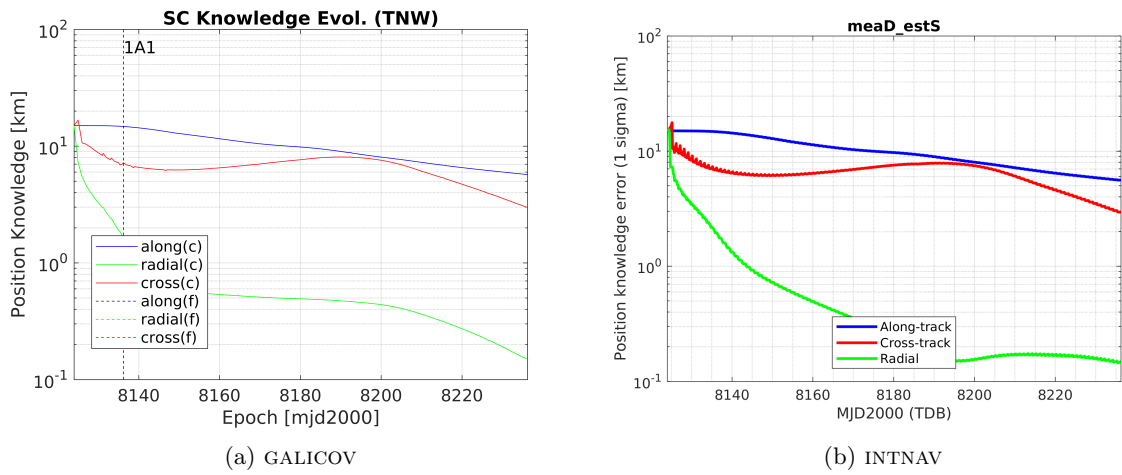
Figure C.4: Spacecraft Position Knowledge - Case 1

(a) GALICOV

(b) INTNAV
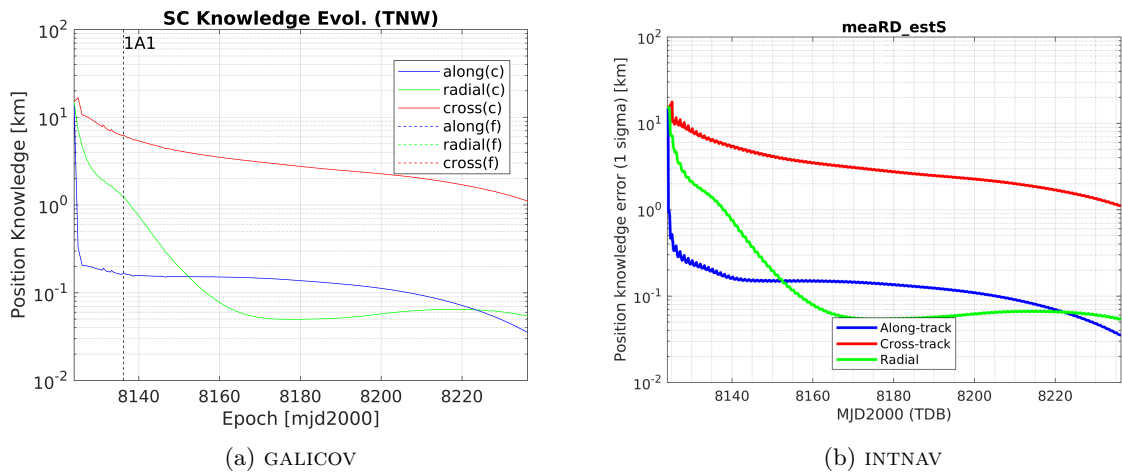
Figure C.5: Spacecraft Position Knowledge - Case 2

(a) GALICOV
(b) INTNAV
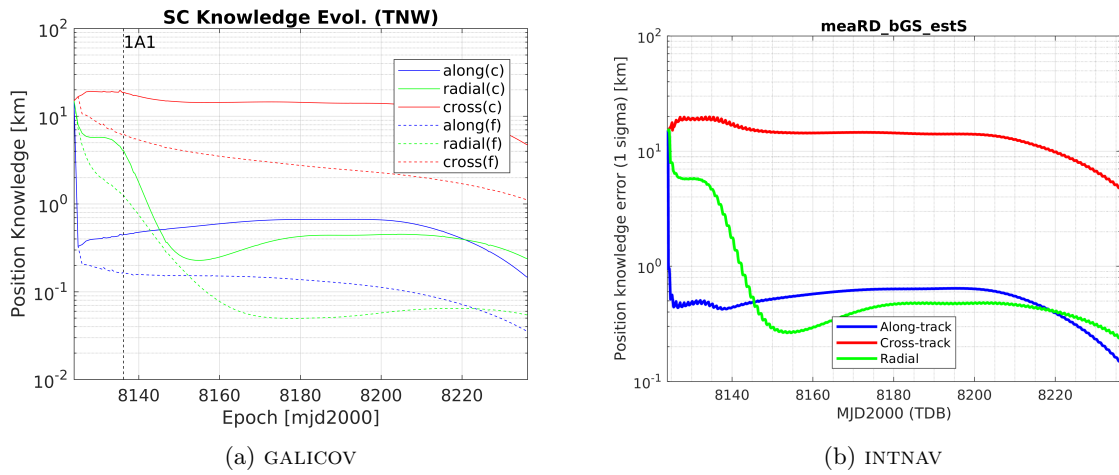
Figure C.6: Spacecraft Position Knowledge - Case 3

(a) GALICOV
(b) INTNAV
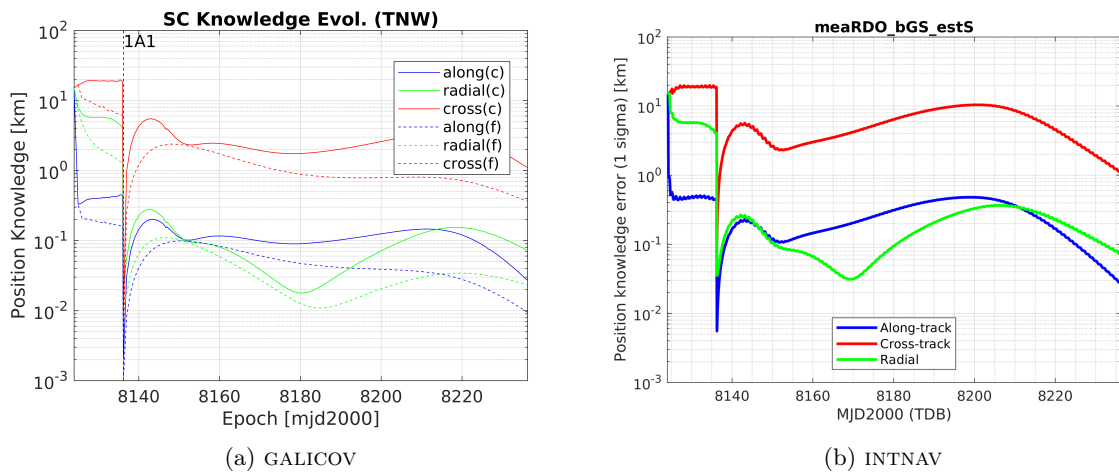
Figure C.7: Spacecraft Position Knowledge - Case 4

C.3. Asteroid UE34
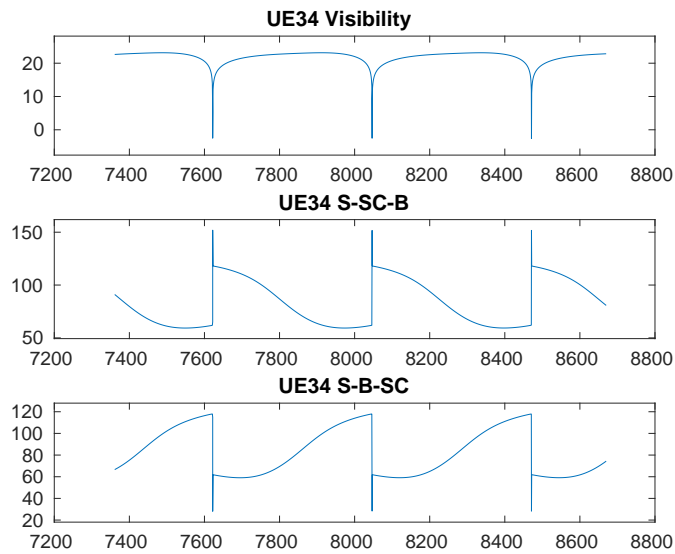
Figure C.8: Optical Measurement Constraints for Case 3 (UE34)
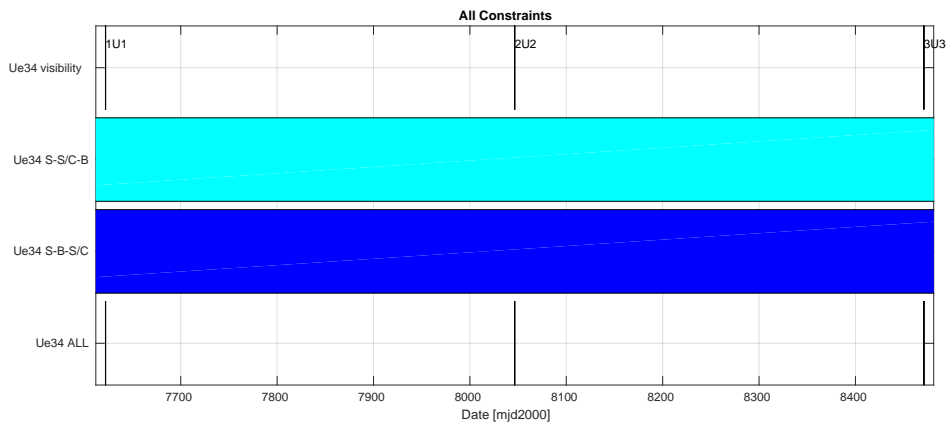
Figure C.9: Optical Measurement Intervals for Case 3 (UE34)
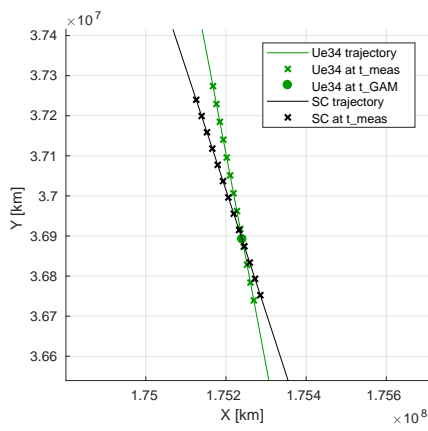
Figure C.10: Optical Measurement Geometry for Case 3 (UE34)
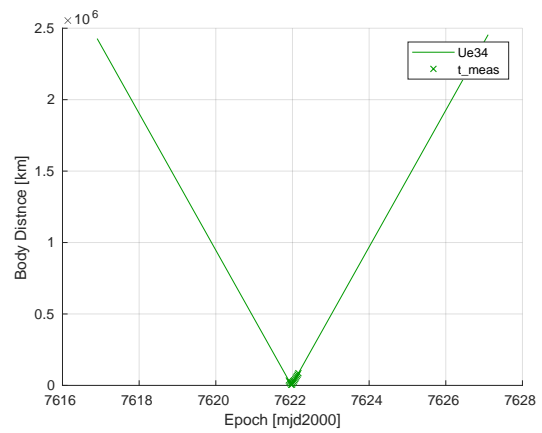
Figure C.11: Optical Measurement Distance for Case 3 (UE34)
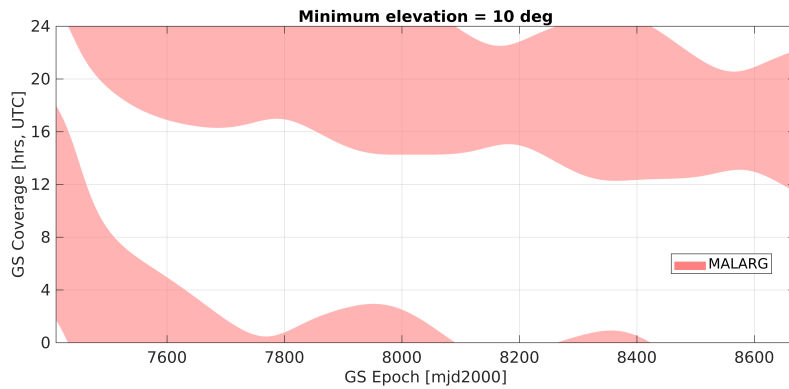
Figure C.12: Radiometric Measurement Schedule for Case 3 (UE34)

C.4. Asteroid WN5
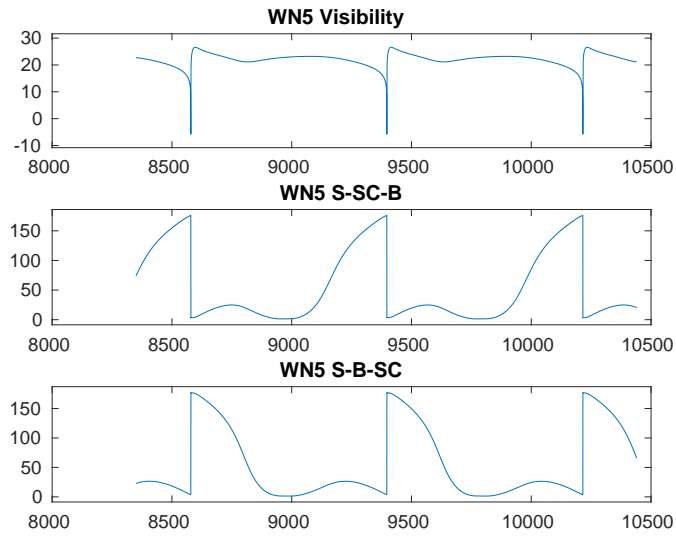
Figure C.13: Optical Measurement Constraints for Case 3 (WN5)
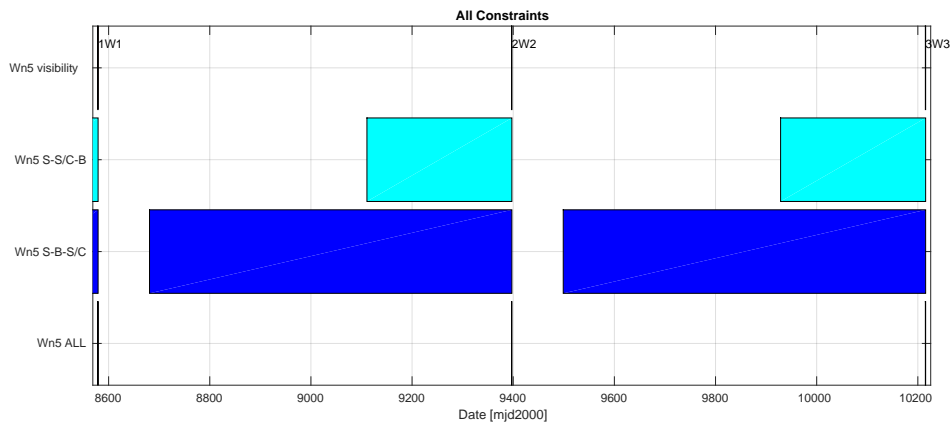
Figure C.14: Optical Measurement Intervals for Case 3 (WN5)
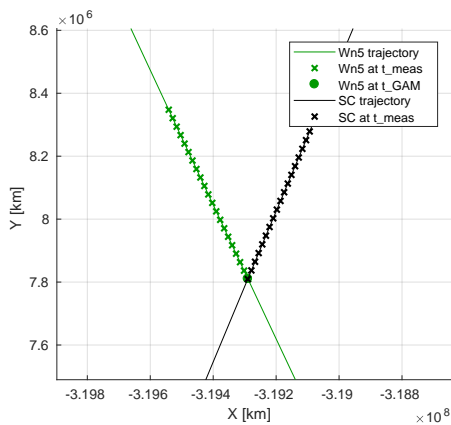
Figure C.15: Optical Measurement Geometry for Case 3 (WN5)
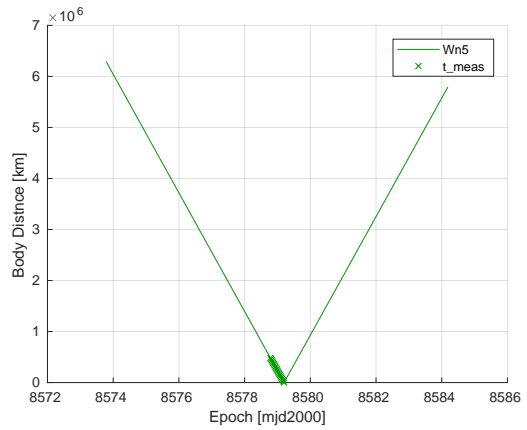
Figure C.16: Optical Measurement Distance for Case 3 (WN5)
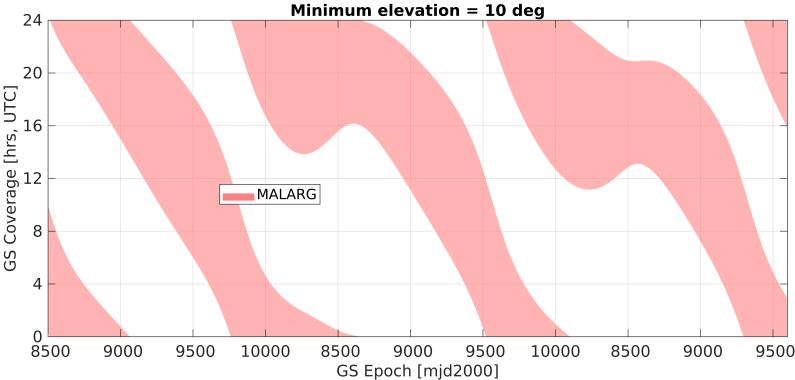
Figure C.17: Radiometric Measurement Schedule for Case 3 (WN5)

D
Reference Missions

All gathered reference data from existing mission and concepts can be found in this appendix. Note that for the concept missions the flyby parameters are not known, and often the expected values are not publicly available. All values that have not been found are left empty. Propulsion types can either be chemical (C), electric (E) or solar sailing (S). Only the parameters of the main propulsion system used for manoeuvres will be listed, as most of the discussed missions use a hydrazine monopropellant system for attitude control. To keep the table compact, "H" is used to denote hydrazine in the table and "X" for xenon. The thrust units are in Newtons when the propulsion type is chemical, and in mN when the propulsion type is electric or solar sailing. The thrust values are per thruster and the number of thrusters is denoted in brackets behind the thrust value (without counting the redundancy engines), if the spacecraft carries more than one. An "e" behind a value denotes that it is the expected value while a "var" means the parameter was variable and a fixed value is not available. Finally, "tbd" stands for to be determined, as the value is unsure at the time of writing. The missions and concepts that perform one or multiple flybys to small bodies and for which enough parameters are known, including their references where the data is extracted from, are the following: NEAR Shoemaker [57], Rosetta [58] [59] [60] [61] [62] [6], Deep Impact [63], DS1 [64] [65] [66] [67] [68] [69], Stardust [70] [71] [72] [73] [74] [75] [76], New Horizons [77] [78] [79] [80] [81], CONTOUR [82] [83], NEA Scout [84], CASTAway [85] [86] and SIMONE [87]. The missions and concepts that on the other hand achieve rendezvous with a small body, and for which enough parameters are known, are the following, again including the references where the data is taken from: Hayabusa and Hayabusa 2 [88] [89] [90] [91] [92], OSIRIS-REx [93] [94] [95], Dawn [96] [97] [98] [99], Psyche [100] [101], AIM [102] [103] [104] [105] [106], M-ARGO [107] [108], Castalia [109], ISHTAR [110] [111] [112] and Don Quijote [113] [114]. Important to note is that the way M-ARGO is designed, it can be used for flyby missions as well.

Table D.1: Flyby Missions and Concepts Summary

	Mission	NEAR	Rosetta			Deep Impact		DS1
			NAVCAM	WAC	NAC	HRI	MRI	MICAS
Mass	Dry [kg]	468	1230					373
	Prop [kg]	318						113
	Payload [kg]							
	Wet [kg]					650		486
Payload	Name/Type		NAVCAM	WAC	NAC	HRI	MRI	MICAS
	FOV [deg]		5x5	2.2x2.2	10x10			0.769x0.769
	Pixels							1024x1024
	Pixel Size [μm]					2	10	9
Flyby	Distance [km]	1200	800, 3160			694		26, 2171
	Velocity [km/s]	9.93	8.6, 15.0			12.3		15.5, 16.5
Propulsion	Type	C	C			C		E
	Propellant	H-NTO	MMH-NTO			H		X
	I_{sp} [s]		292					1814-3127
	Thrust [N or mN]	450	10 (24)					19-92.7

	Mission	Stardust	New Horizons			CONTOUR	
		Camera	Alice	Ralph	LORRI	CRISP	CFI
Mass	Dry [kg]	300	400			328	
	Prop [kg]	85	76.8			70	
	Payload [kg]		30				
	Wet [kg]	385	476.8			398	
Payload	Name/Type	Camera	Alice	Ralph	LORRI	CRISP	CFI
	FOV [deg]	3.5x3.5	4x0.1	5.7x0.15	0.29x0.29	1.2x1.2	2.5x2.5
	Pixels	1024x1024				1024x1024	
	Pixel Size [μm]						
Flyby	Distance [km]	3078.5, 236.4, 200	12500, 3000				
	Velocity [km/s]	7.4, 6.1, 10.9	var, tbd			28.3 (e), 14.0 (e)	
Propulsion	Type	C	C			C	
	Propellant	H	H			H	
	I_{sp} [s]						
	Thrust [N or mN]	4.4 (8)	4.4 (4)			(16)	

	Mission	NEA Scout	CASTAway
Mass	Dry [kg]	14	735
	Prop [kg]	0	340
	Payload [kg]	0.256	53
	Wet [kg]	14	1150
Payload	Name/Type	ECAM M-50	Telescope
	FOV [deg]	25x19	0.5x0.5
	Pixels	2650x1944	2048x2048
	Pixel Size [μm]	2.2	18
Flyby	Distance [km]	10	
	Velocity [km/s]		
Propulsion	Type	S	C
	Propellant		MON-MMH
	I_{sp} [s]		320
	Thrust [N or mN]		

Table D.2: Rendezvous Missions and Concepts Summary

Mission		Hayabusa	Hayabusa 2		OSIRIS-REx	Dawn
Mass	Dry [kg]	380	500		880	747.1
	Prop [kg]	130	100		1230	525.5
	Payload [kg]					
	Wet [kg]	510	600		2110	1217.7
Payload	Name/Type	AMICA	Wide Camera	NavCam		FC
	FOV [deg]	5.83x5.69	54x54	5.4x5.4		5.5x5.5
	Pixels	1024x1000				
	Pixel Size [μm]	12				
Propulsion	Type	E	E		C	E
	Propellant	X	X		H	X
	I_{sp} [s]	3000	2740-2890		25-236	3100
	Thrust [N or mN]	8	6.3-9		85-360 (4)	90 (2)

Mission		Castalia		SIMONE	ISHTAR	Don Quijote
Mass	Dry [kg]	1386		90.2	300	395
	Prop [kg]	225		39.8	108	96
	Payload [kg]	20		13.1	25	19.7
	Wet [kg]	1611		120	408	491
Payload	Name/Type	VIS	NIR	MIS		Camera
	FOV [deg]	5.5x5.5	11.4x12.1	5.3x5.3		5.3x5.3
	Pixels	1024x1024	1024x1024	1024x1024		
	Pixel Size [μm]	15	30			
Propulsion	Type	E		E	E	C or E
	Propellant	X		X	X	
	I_{sp} [s]	4200				
	Thrust [N or mN]	160				

Mission		Psyche	AIM	HERA	M-ARGO		
Mass	Dry [kg]	1300	510.3	389.4	20		
	Prop [kg]	1100	307	249	2		
	Payload [kg]						
	Wet [kg]	2400	817.3	638.4	22		
Payload	Name/Type		AFC		VIS	NIR	SWIR
	FOV [deg]		5.5x5.5		6x6	5.3x5.3	5
	Pixels				614x614	256x256	1
	Pixel Size [μm]				5.5	30	1000
Propulsion	Type	E	E	E	E		
	Propellant	X	X	X	X		
	I_{sp} [s]	1800	1420		3050 / 3180		
	Thrust [N or mN]	280	54		1.7 / 2.4		